UNIVERSIDADE FEDERAL DO CEARÁ
CENTRO DE CIENCIAS
DEPARTAMENTO DE GEOLOGIA
PROGRAMA DE PÓS-GRADUAÇÃO EM GEOLOGIA

ROBERTA ESPOSITO

APPLICATION OF MAGNETOTELLURIC METHOD IN SEDIMENTARY ENVIRONMENTS AND ANALYSIS OF THE RESISTIVITY DISPERSION IN PRESENCE OF 3D POLARIZABLE STRUCTURES

FORTALEZA
2016

ROBERTA ESPOSITO

APPLICATION OF MAGNETOTELLURIC METHOD IN SEDIMENTARY ENVIRONMENTS AND ANALYSIS OF THE RESISTIVITY DISPERSION IN PRESENCE OF 3D POLARIZABLE STRUCTURES

Tese apresentada ao Programa de Pós-Graduação em Geologia da Universidade Federal do Ceará, , como requisito parcial à obtenção do título de Doutor em Geologia. Área de concentração: Geodinâmica e recursos Minerais.

Orientador: Prof. Dr. Raimundo Mariano Gomes Castelo Branco.

FORTALEZA

2016

Dados Internacionais de Catalogação na Publicação
Universidade Federal do Ceará
Biblioteca Universitária
Gerada automaticamente pelo módulo Catalog, mediante os dados fornecidos pelo(a) autor(a)

E79a Esposito, Roberta.
Application of Magnetotelluric Method in sedimentary environments and analysis of the resistivity dispersion in presence of 3D polarizable structures / Roberta Esposito. – 2016.
102 f. : il. color.

Tese (doutorado) – Universidade Federal do Ceará, Centro de Ciências, Programa de Pós-Graduação em Geologia, Fortaleza, 2016.
Orientação: Prof. Dr. Raimundo Mariano Gomes Castelo Branco.

1. Resistivity frequency dispersion. 2. Magnetotelluric Method. 3. 3D strustures. I. Título.
CDD 551

ROBERTA ESPOSITO

APPLICATION OF MAGNETOTELLURIC METHOD IN SEDIMENTARY ENVIRONMENTS AND ANALYSIS OF THE RESISTIVITY DISPERSION IN PRESENCE OF 3D POLARIZABLE STRUCTURES

Tese apresentada ao Programa de Pós-Graduação em Geologia da Universidade Federal do Ceará, , como requisito parcial à obtenção do título de Doutor em Geologia. Área de concentração: Geodinâmica e recursos Minerais.

Aprovada em: 13/06/2016.

BANCA EXAMINADORA

_____

Prof. Dr. Raimundo Mariano Gomes Castelo Branco (Orientador)
Universidade Feral do Ceará (UFC)

_____

Profa. Dra. Sônia Maria Silva Vasconcelos
Universidade Federal do Ceará (UFC)

_____

Prof. Dr. Milenko Markovic
Universidade Federal do Ceará (UFC)

Prof. Dr. Christiano Magini
Universidade Federal do Ceará (UFC)

Prof. Dr. Francisco Nepomuceno Filho
Universidade Federal do Ceará (UFC)

ACKNOWLEDGEMENTS

There are many people without whom this thesis might have not been written, and to whom I am grateful.

First of all, I want to thank CAPES for the financial support that allowed me to realize this work and the GEOFMEL project of FCPC, UFC and CENPES/PETROBRAS.

I wish to express my sincere gratitude to Prof. Dr. Raimundo Mariano Gomés Castelo Branco for his orientation and useful help during my time spent in Fortaleza. For his support and encouragement in every step of this adventure.

I want to thank the Professors of Examination Committee for the time, valid suggestions and collaboration. I am thankful to Prof. Dr. Cícero Regis da UFPA, Prof. Dr. Nepomuceno and Prof. Dr. Sônia Vasconcelos for the valuable advices, modifications and for the time they invested to make me valorize my work at the best. Their collaboration has been essential to realize and express the potential of this work and its contribution to the scientific community.

I want to thank all the people of the Post-Graduation program of UFC that helped me for every inconvenience could have been occurred and the Secretary of the Geology Department.

I am thankful to all the Professors of UFC, to Prof. Dr. Jose de Araujo Nogueira Neito, Prof. Dr. Christiano Magini and every one that I met during my permanence at UFC that gave a contribution to my professional and emotional life.

I would like to thank all my colleagues of UFC, especially Fabiano Mota da Silva for the big help and the constant support.

I want to thank the Vesuvius Observatory and all the researchers that helped me during my PhD.

I sincerely thank Professor Domenico Patella for the time, suggestions, collaboration and inestimable help.

I want to thank my colleagues Dr. Alessandro Fedele and Dr. Lucia Nardone for their ideas, help and good humor.

My deepest appreciation belongs to my family and to Michele for the patience and understanding.

I want to thank my friends, colleagues and all the people that in some way gave their contribution to make me face the PhD at the best.

ABSTRACT

Magnetotelluric method allows the determination of electrical resistivity distribution in the subsurface in order to differentiate structures underneath. With appropriate data inversion procedures it is possible to obtain resistivity values from a few tens of meters to hundreds of kilometers. As with all geophysical prospecting methods, the MT method is subject to ambiguities because of the resistivity dispersion phenomenon. This phenomenon might deform the MT response curves and can lead to erroneous interpretation.

A general conclusion is that the dispersion effects can influence the MT response either in recognizable or in subtle forms. In both cases, disregarding the distortion effects may lead to misleading conclusions as to the physical properties of the surveyed structures.

This work deals with different aspects of the magnetotelluric method. First of all the resistivity dispersion is treated theoretically performing, for the first time, simulations over a 3-D Earth model (1-D case is reported from a previous work of Esposito and Patella, 2009 and 2-D case is reconstructed basing the simulation on a previous work of Mauriello *et al.,* 1996) with a case study in a geothermal area as example (Snake River Plain, Idaho, USA). It is shown an MT application in the Pecém costal area (Ceará, Brazil), disregarding the resistivity dispersion, in order to show the efficiency of the method in solving subsurface resistivity contrasts and finally theoretical simulations showing the application of the MT method for Oil and Gas in the emerged portion of Potiguar Basin (Rio Grande do Norte, Brazil) are performed, in order to consider the MT as a support in areas where the seismic, mainly used for these purposes, can be logistically hard to apply or needs a comparison with other geophysical prospecting methods.

Keywords: Resistivity dispersion. Magnetotelluric response. 3D structures.

RESUMO

O Método magnetotelúrico permite a determinação da distribuição de resistividade elétrica na subsuperfície, a fim de diferenciar as estruturas presentes. Com os procedimentos de inversão de dados é possível obter valores de resistividade de algumas dezenas de metros até centenas de quilómetros. Como acontece com todos os métodos de prospecção geofísica, o método MT está sujeito a ambiguidades por causa do fenômeno da dispersão da resistividade. Este fenómeno pode deformar as curvas de resposta MT e pode conduzir a uma interpretação errónea.

Uma conclusão geral é que os efeitos de dispersão pode influenciar a resposta MT em forma reconhecível ou sutil. Em ambos os casos, sem considerar os efeitos de distorção a interpretação pode levar a conclusões enganosas sobre as propriedades físicas das estruturas pesquisadas.

Este trabalho trata com diferentes aspectos do Método Magnetotelúrico. Em primeiro lugar a dispersão da resistividade é estudada teoricamente realizando, pela primeira vez, simulações de um modelo 3-D da Terra (caso 1-D é apresentado a partir de um trabalho anterior de Esposito e Patella, 2009 e o caso 2-D é reconstruído baseando a simulação sobre um trabalho de Mauriello et al., 1996), com um estudo de caso em uma área geotérmica (Snake River Plain, Idaho, USA).

Mostra-se uma aplicação do MT na área do Pecém (Ceará, Brasil), desconsiderando a dispersão da resistividade, a fim de mostrar a eficiência do método para resolver contrastes de resitividade na subsuperfície e, finalmente, são realizadas as simulações teóricas que mostram a aplicação do método MT para pesquisa de Oléo e Gás na porção emersa da Bacia Potiguar (Rio Grande do Norte, Brasil), a fim de considerar a MT como um apoio em áreas onde a sísmica, usada principalmente para esses fins, pode ser logisticamente difícil de aplicar ou precisa de uma comparação com outros métodos de prospecção geofísica.

Palavras chaves: Dispersão da resistividade. Resposta Magnetotelúrica. Estruturas 3D.

TABLE OF FIGURES

LIST OF TABLES

LIST OF SYMBOLS

MT	Magnetotelluric
CSAMT	Controlled Source Audio-Magnetotelluric
IP	Induced Polarization
TD	Time Domain
FD	Frequency Domain
CPRM	Companhia de Pesquisa e Recursos Minerais
B	Magnetic field
E	Electric field
Z	Impedance
j	Current density
ρ	Resistivity
ρ(ω)	Impedivity
σ	Conductivity
σ(ω)	Admittivity
Ωm	Ohm m
Hz	Hertz

TABLE OF CONTENTS

1 INTRODUCTION

Geophysical prospection is a big set of earth imaging techniques that uses physical parameters to study the underground matter. The main goal of prospection is to detect the geometry of the buried structures and objects and in particular to reveal areas of economic interest, like mineral deposits, oil and gas reservoirs, underground water or geothermal fluids. There are different geophysical prospection methods and, because of the different field sources, each one is sensible to a particular physical property like the density in the gravimetric and seismic methods (in the latter case through the seismic waves velocity), electrical resistivity (or its inverse, the conductivity) in the electric and electromagnetic methods and the magnetic susceptibility in the magnetic method.

The field sources allow the classification of the methods in two categories: those that use the natural field of the Earth (gravimetric, magnetic, electric and electromagnetic methods) and the ones that need an artificial source (seismic, inductive electric and electromagnetic methods). The natural or artificial fields that propagate in the subsurface are measured at the surface and the local field perturbations are supposed to be caused by the presence of structures buried at different depths.

All prospecting methods are subjected to interpretation ambiguities due to the fact that different geological configurations can reproduce the same effects at the surface. The situation can be quite complex if the buried structures are bi-dimensional or anisotropic like several rocks, which store oil, gas and underground water (Jones, A., J., 2006)

In the Magnetotelluric Method (MT) a source of ambiguity called resistivity dispersion exists. The resistivity dispersion phenomenon due to the induced polarization is a well-known phenomenology (Martinez, J. and Armenta, J., 2007; Prosvirnin, S. L. and S. Zouhdi, S., 2006; Sjöberg, D., 2006) and it can influence MT responses creating distortions in the curves that may easily lead to an erroneous interpretation (Esposito, R. and Patella, D., 2009, Patella, D., 1979).

Hydrocarbon and geothermal research are application fields, where MT is an ideal approach to detect dispersion-affected zones. These zones are fractured portions of rock, which have undergone diffuse alterations due to chemical interaction with uprising light hydrocarbons and hot fluids. They are considered reliable markers of the presence of exploitable reservoirs underneath (Sternberg and Oehler, 1990; Wright at al., 1985).

The thesis is divided in three chapters. The first one provides the theoretical bases of the resistivity dispersion in the magnetotelluric method. In particular there are reported the MT responses over a 1-D and a 2-D polarizable structures. In the second chapter we performed, thought the use of a modeling software, a set of 3-D theoretical simulations showing the effects of the dispersion on the MT response curves resulting form a 3-D structure underneath.
Finally in the third chapter we show the results of two MT applications, one field experiment and one theoretical study, in two different areas of the Northeast Brazilian coast.

1.1 Objectives

1.1.1 General

The main objective of this work is to show the application of the Magnetotelluric method in different areas and the analysis of resistivity dispersion over 3-D polarizable structures.

1.1.2 Specific

Specific objectives are:

a) To perform numerical simulations of the MT response in presence of 3-D polarizable structures.
b) To perform a case study of the geothermal area of Snake River Plain, Idaho.
c) To process, invert and interpret data in the Ceará costal area of Pecém.
d) To perform numerical simulations of the MT response in the emerged portion of the Potiguar Basin for Oil and Gas exploration.

1.2 Justification

The magnetotelluric method is increasingly used both in applied geophysics and in basic research. It is less well known than seismology as Earth investigation technique, nevertheless the MT has a great potential that is yet to be fully realized. During the past

decades the MT method passed through a phase of fast development especially from a computational point of view (with two and three-dimensional modeling and inversion), allowing a considerable improvement in the study of the Earth through this methodology. MT can be an important interpretation tool, integrated with other geophysical prospection methods, to the study of sedimentary basins for example, both terrestrial and oceanic. In the case of active volcanic areas, the MT method is very efficient because it is able to reach great depths in comparison to other electromagnetic methods and to distinguish deep geothermal reservoirs. MT method allows the location of the low resistivity anomalies under volcanic sediments.

As we have mentioned before, a limit to the MT method can be the resistivity dispersion phenomenon, i. e. the resistivity is dependent from the incident wave frequency. Electrical resistivity is the behavior of a material to oppose to the passage of electric current. It is a parameter that can differentiate rocks (Palacky, G.V., 1987) and that depends on their physical state, the presence of fluids in rock pores, soil permeability and its temperature (Keller and Frischknecht, 1966; Olhoeft, G. R., 1980).

Resistivity values vary in a very large interval, 10^{-7} - 10^{7} Ωm, differentiating rocks and their physical states. For example, the resistivities of saturated rocks are directly proportional to that of the fluid in the pores and inversely proportional to the porosity. Of course the electrical resistivity alone is not enough for a precise identification of the materials or rocks but to minimize the ambiguity on the resistivity values is undoubtedly an important and valid goal.

The motivation behind this work is primarily the study (in addition to the one-dimensional and two-dimensional cases already studied) of the dispersion of the resistivity due to 3-D polarizable structures in the subsurface and secondly the application, disregarding the dispersion effect, of the method (both theoretically and experimentally) in areas not yet observed by the MT. The importance of the 3-D Earth model affected by the resistivity dispersion is supported by a case study in which we observe clearly how the dispersive 3-D model fits very well the experimental data. This can be a starting point for the use of 3-D models including the resistivity dispersion where it is supposed to verify.

We have chosen three types of geological structures in this work: the Snake River Plain, (Idaho, USA), the Pecém region (Fortaleza, Ceará State) and the Potiguar Basin (Rio Grande do Norte).

There are different reasons behind the choice of these areas. The first is a geothermal area in which we have performed a 3-D theoretical simulation including the dispersion of the

resistivity to better fit the experimental data of Stanley (1982), the second is aimed at the knowledge and study of geological structure of a very poor known zone and the third is motivated by the application of the MT method in areas, such as a sedimentary basin with hydrocarbon reservoirs, usually investigated by the seismic method, in order to show that the MT method can be a valuable support, less expensive than seismic and logistically easier to apply .

2 DISPERSIVE MAGNETOTELLURICS

2.1 Theoretical background of the Magnetotelluric Method (MT)

The MT method is an exploration technique that uses the natural electromagnetic field to estimate electrical resistivity values of the subsurface.

MT theory was introduced for the first time in 1950 by Tikhonov and in a more detailed way by Cagniard few years later, in 1953. It is based on the concept that electromagnetic waves generated in the far distance from the Earth's surface reach the crust of our planet where they vertically penetrate underground and provide information on the electrical properties of found materials.

When the waves travelling underground encounter materials with different resistivities, they are partially reflected at the interfaces and they return to the surface containing information about the crossed layers. Natural electromagnetic fields used by the MT method are generated mainly by two phenomena and cover a frequency range between 10^{-4} - 10^{4} Hz. The first phenomenon is the interaction between the solar plasma and Earth's magnetosphere (MT low frequency field, Fig. 5), and the second is the presence of storms between the two tropics (MT high frequency field, Fig. 6). (Parker, 1958; Campbell, 1987).

Interactions between the solar wind and the Earth's magnetosphere generate fluctuations in the electromagnetic field lower than 1Hz. The solar wind emits streams of ions, protons and electrons from the Sun, and on the encounter with terrestrial magnetic field (at the magnetopause) these protons and electrons, deflected in opposite directions, create an electric field. This is a throbbing phenomenon, not static, which means that the deformation of the magnetic field is variable in time, with frequency between 1 Hz and 10^{-4} Hz. The increase is solar wind pressure pushes the magnetopause closer to the Earth giving rise to magnetic storms (Fig. 1) (Chapman and Ferraro, 1931).

Electromagnetic fields with frequency higher than 1Hz have their origins in meteorological activity like lightening discharges. These, known as "sferics" (impulsive signals emitted by lightening), propagate around the world within the waveguide bounded by the ionosphere and Earth's surface (Dobbs, 1985, *Electromagnetic Waves*).

It is a source of uniform electromagnetic energy due to the constant presence of lightening on the Earth's surface. Zones where we have most of this type of activity are

located in the equatorial regions, where storms have an average rate of 100 days per year (Fig. 2).

It is a perturbation that propagates over a long distance, and as in the previous case, is not static, but produces a variable magnetic field this time with frequency between 1 Hz and 10^4 Hz.

Figure 1: Interaction between solar plasma and magnetosphere (a) Distortion of the front of solar plasma by Earth's magnetic field. (b) Magnetic field lines showing the form of the Earth's magnetosphere under the effect of the solar wind.

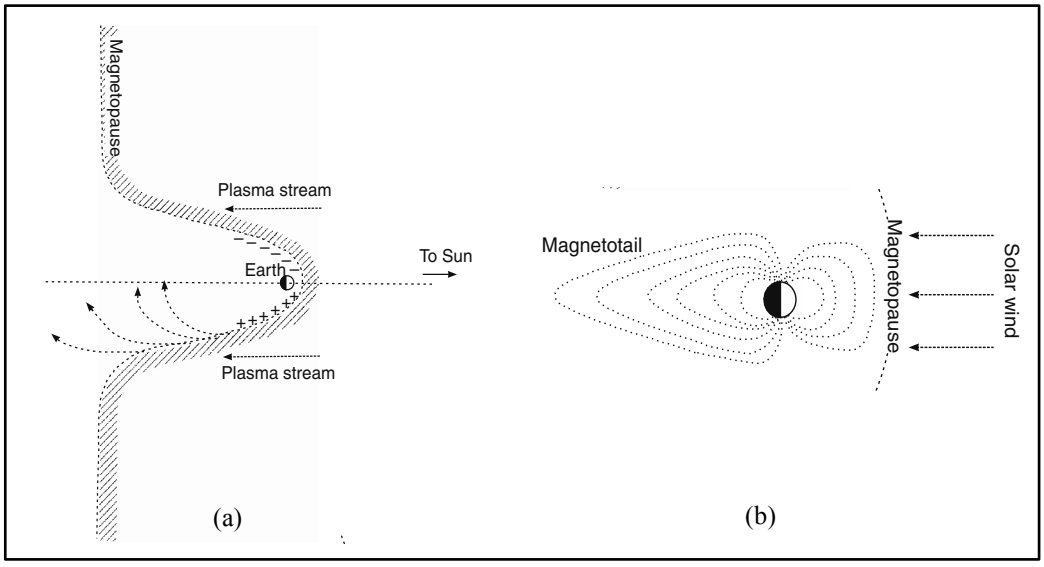

Modified from Simpson and Bahr, *Practical Magnetotellurics*, 2005. a) from Chapman and Ferrero, 1931

Figure 2: Contour lines (isolines) represent the storms average rate in a year around the globe.

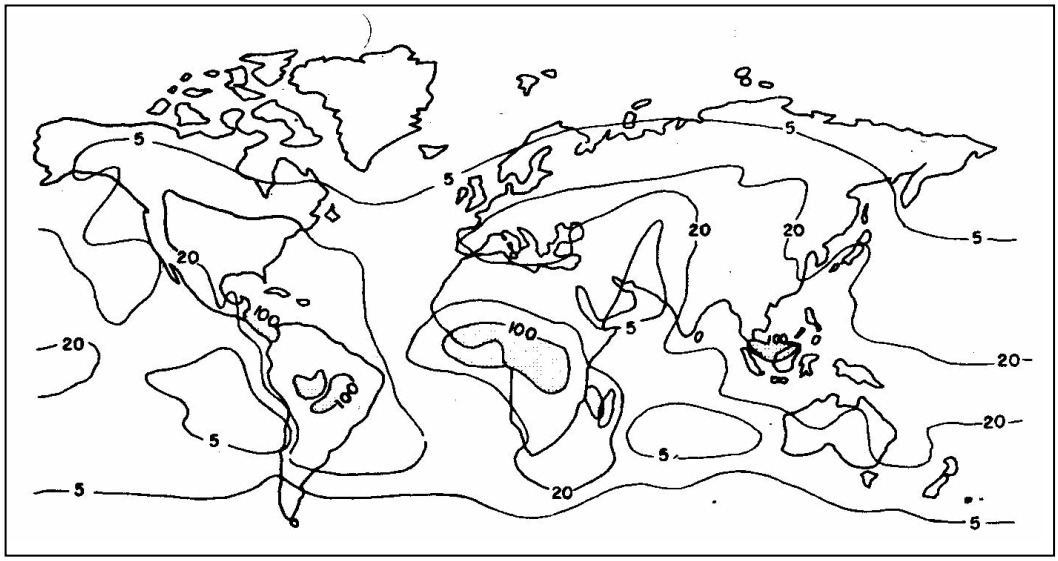

Modified from Grandt, 1991.

The ionosphere acts as an intermediary between the two phenomena, distributing evenly the dynamic effects so that natural electromagnetic source field utilized, relatively far away from the Earth's surface, may be treated as uniform, plane-polarized electromagnetic waves (Tikhonov 1950, Cagniard, 1953) normally incident on the Earth surface. Wait (1954) and Price (1962) showed that limitations of the normally incident wave assumption arise when the lateral extension of the source is not significantly larger than the penetration depth of electromagnetic fields into the Earth, requiring a correction in Cagniard's (1953) formulation.

Another peculiarity of the Tikhonov-Cagniard model is that it ignores the sphericity of the earth. This question has been addressed by many researchers (Srivastava, 1966; Sochel'nikov, 1979; Kaufman and Keller, 1981; Berdichevsky and Zdanov, 1984) and the most elegant solution has been advanced by P. Weidelt (1972) establishing the relationship between spherical and plane models. The conditions are satisfied for depths that not exceed a few hundreds of kilometers. Therefore, for the purpose of MT, it is sufficient to consider a flat Earth model with electromagnetic fields described in Cartesian coordinates.

The plane wave field is a mixture of monochromatic waves that travel vertically in the ground and generate telluric currents (from which the name magnetotelluric).

The external energy reaches the Earth's surface where is partially reflected and the remaining part penetrates into the Earth inducing electric currents, known as telluric currents, which generate a secondary magnetic field.

Magnetotelluric is based on the simultaneous measurements of total electromagnetic field, time variation of both magnetic field B(t) and induced electric field E(t), through which it is possible to obtain information on the electrical properties (electrical resistivity) since they correlated to the impedance **Z**, which is the ratio of the electrical (E) and magnetic (B) components.

According to the property of electromagnetic waves in the conductors, the penetration of electromagnetic wave depends on the oscillation frequency through the following mathematical relationship:

$$p \approx 500 \sqrt{(\rho/f)} \qquad (1.1)$$

where p, called *skin depth* is expressed in meters, ρ is the resistivity expressed in Ωm and f is the frequency in Hz.

Frequency values between 10^{-4} Hz and 1 Hz (Magnetotellurics) investigate deeper structures, and values between 1 Hz and 10^{4} Hz (Audio-Magnetotellurics) "shallower" structures instead. Skin depth depends also on resistivity values of the layers lying over the target.

The frequency interval between 0.5 and 5 Hz is known as *dead band* because in this range of frequency the natural electromagnetic signal is not good enough to allow a good quality data acquisition and a good resolution of objects buried up to a few kilometers of depth.

Goldstein and Strangway in 1975 introduced a new methodology of artificial source (CSAMT - *controlled source audio-magnetotellurics*) to better study underground shallow layers (up to 2-3 km). This is a high-resolution technique and it was found very efficient in imaging Earth's crust between 20m and 2000m.

The source of CSAMT method, typically in a frequency interval of 0.1 – 8 kHz, consists of en electric dipole positioned into the ground that generates an electromagnetic field simulating the natural field. The electric dipole simulating the source, usually 2-3 km long is positioned at a great distance (minimum 3 times the skin depth) from the measurements area. The distance between the source and the measurements area is necessary

to guarantee that the field is not influenced by *near-field* effects. In the proximity of the source the electromagnetic waves are curved and the Cagniard resistivity doesn't provide realistic resistivity values. When *far-field* conditions are satisfied electric and magnetic fields behave like plane waves, similar to natural MT and AMT, and for this reason we can use the same equations used in the MT method.

Data acquired allow us to calculate values of impedance **Z**, which is related to magnetic field and electric field for every frequency value.

$$\begin{pmatrix} E_x \\ E_y \end{pmatrix} = \begin{pmatrix} Z_{xx} & Z_{xy} \\ Z_{yx} & Z_{yy} \end{pmatrix} \begin{pmatrix} H_x \\ H_y \end{pmatrix}, \tag{1.2}$$

$$E_x = Z_{xx}H_x + Z_{xy}H_y, \tag{1.3}$$

$$E_y = Z_{yx}H_x + Z_{yy}H_y. \tag{1.4}$$

The impedance **Z** is complex with a real and imaginary part; every component Z_{ij} has a magnitude and a phase. It is correlated to the apparent resistivity through the equation

$$\rho_{a,ij}(\omega) = \frac{1}{\mu_0 \omega} \left| Z_{ij}(\omega) \right|^2 \tag{1.5}$$

where ω is the angular frequency and μ_0 is the magnetic permeability of the vacuum, which is not very different from magnetic permeability of Earth's materials.

The phase is represented by the equation

$$\phi_{ij} = tan^{-1}\left(\frac{Im\{Z_{ij}\}}{Re\{Z_{ij}\}}\right). \tag{1.6}$$

In the case of 1-D Earth (a stack of isotropic layers), where conductivity varies only with depth, the diagonal tensor elements Z_{xx} and Z_{yy} are zero, whilst the off-diagonal elements are equal in magnitude but have opposite signs:

$$\mathbf{Z_{1-D}} = \begin{bmatrix} 0 & Z_{xy} \\ -Z_{xy} & 0 \end{bmatrix} \tag{1.7}$$

there are two parameters per frequency, which are the real and imaginary parts of the complex impedance.

For a 2-D Earth, in which conductivity varies along one horizontal direction as well as with depth, Z_{xx} e Z_{yy} are equal in magnitude, but have opposite sign, whilst Z_{xy} e Z_{yx} differ. If we in consider x or y direction aligned along the direction of geoelectric strike of the 2-D structures, the tensor becomes

$$\mathbf{Z_{2-D}} = \begin{bmatrix} 0 & Z_{xy} \\ Z_{yx} & 0 \end{bmatrix} \tag{1.8}$$

with four parameters per frequency.

The observed coordinate system is often not aligned to structural strike, so a fifth, frequency-independent parameter, namely the obliquity between the observation reference system and geoelectric strike, θ, needs to be defined, where

$$\mathbf{Z}_{2-D}(\theta) = \mathbf{R} \cdot \mathbf{Z}_{2-D}(0) \cdot \mathbf{R}^T$$

$$= \begin{bmatrix} \cos(\theta) & \sin(\theta) \\ -\sin(\theta) & \cos(\theta) \end{bmatrix} \begin{bmatrix} 0 & Z_{xy}(0) \\ Z_{yx}(0) & 0 \end{bmatrix} \begin{bmatrix} \cos(\theta) & -\sin(\theta) \\ \sin(\theta) & \cos(\theta) \end{bmatrix}$$

$$= \begin{bmatrix} \cos(\theta)\sin(\theta)\left[Z_{xy}(0) + Z_{yx}(0)\right] & \cos^2(\theta)Z_{xy}(\theta) - \sin^2(\theta)Z_{yx}(0) \\ \cos^2(\theta)Z_{yy}(\theta) - \sin^2(\theta)Z_{xx}(0) & -\cos(\theta)\sin(\theta)\left[Z_{xy}(0) + Z_{yx}(0)\right] \end{bmatrix}. \tag{1.9}$$

Knowing that $Z_{yy}(\theta) = -Z_{xx}(\theta)$, the impedance tensor will be

$$\mathbf{Z}_{2-D}(\theta) = \begin{bmatrix} Z_{xx}(\theta) & Z_{xy}(\theta) \\ Z_{yx}(\theta) & -Z_{xx}(\theta) \end{bmatrix}. \tag{1.10}$$

With measured data, it is often not possible to find a direction in which the condition that $Z_{xx} = Z_{yy} = 0$ is satisfied.

Figure 3: Model showing electromagnetic field decomposition. Blue and orange structures represents two materials with different resistivities ρ_1 and ρ_2.

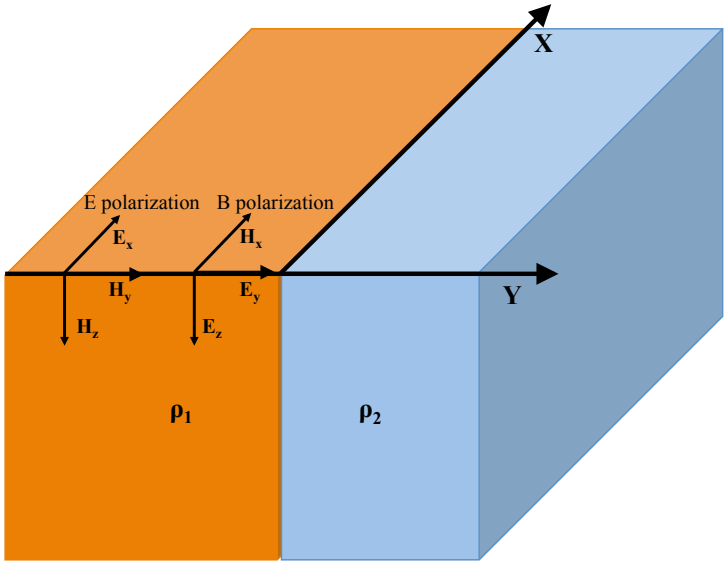

For an ideal 2-D case (Fig. 3) we can divide the electromagnetic field in two independent modes, TE and TM

- H perpendicular to the *strike* --- TE mode
- H parallel to the *strike*--- TM mode

and consider two apparent resistivities ρ_{xy} and ρ_{xy}

$$\rho_{a,xy}(\omega) = \frac{1}{\mu_0 \omega} \left| Z_{xy}(\omega) \right|^2 \tag{1.11}$$

$$\rho_{a,yx}(\omega) = \frac{1}{\mu_0 \omega} \left| Z_{yx}(\omega) \right|^2. \tag{1.12}$$

For a 3-D earth the impedance tensor is

$$\mathbf{Z_{3-D}} = \begin{bmatrix} Z_{xx} & Z_{xy} \\ Z_{yx} & Z_{yy} \end{bmatrix} \tag{1.13}$$

and there are eight parameters per frequency.

2.2 Magnetotelluric dispersion

Resistivity dispersion phenomenon can manifest itself when the soil is electrically polarizable. In the frequency range of the MT method (10^{-4}-10^{4} Hz) a very important phenomenon can occur which gives additional information in underground investigation: the Induced Polarization phenomenon (10^{-2}-10^{2} Hz).

Induced Polarization (IP) is the basis for a geophysical prospecting method as well and it occurs, under particular conditions, when electrical current flows into the subsoil.
It is a transient and very complex phenomenon, correlated to electrochemical processes in rocks and consists of the creation of electrical dipoles oriented with the electrical source field.
Main factors that determine IP are:

- Mineral composition
- Rocks pattern
- Water percentage
- Chemical composition of water

Experimentally, Induced Polarization can be recognized by positioning on Earth's surface a quadrupole ABMN, where A and B are the current electrodes while M and N are the voltage electrodes. A direct current is sent into the subsoil and in presence of polarization the potential difference measured after the interruption of the current returns to zero slower than a normal trend (Fig. 4).

The charges take some time to redistribute when an external DC electric field is applied (charging). Equivalently they take the same time to revert to a balanced distribuition once the electric field is removed (discharging).

The subsoil behaves as a distribution of capacitors that are charged and uncharged. The system will return to the state of equilibrium in an amount of time, which is function of the soil polarizability.

Figure 4: Induced Polarization phenomenon (from Patella 2003): (a) measurements equipment over the surface, A and B are the current electrodes, M and N potential electrodes, (b) curves in time domain, (c) curves in frequency domain.

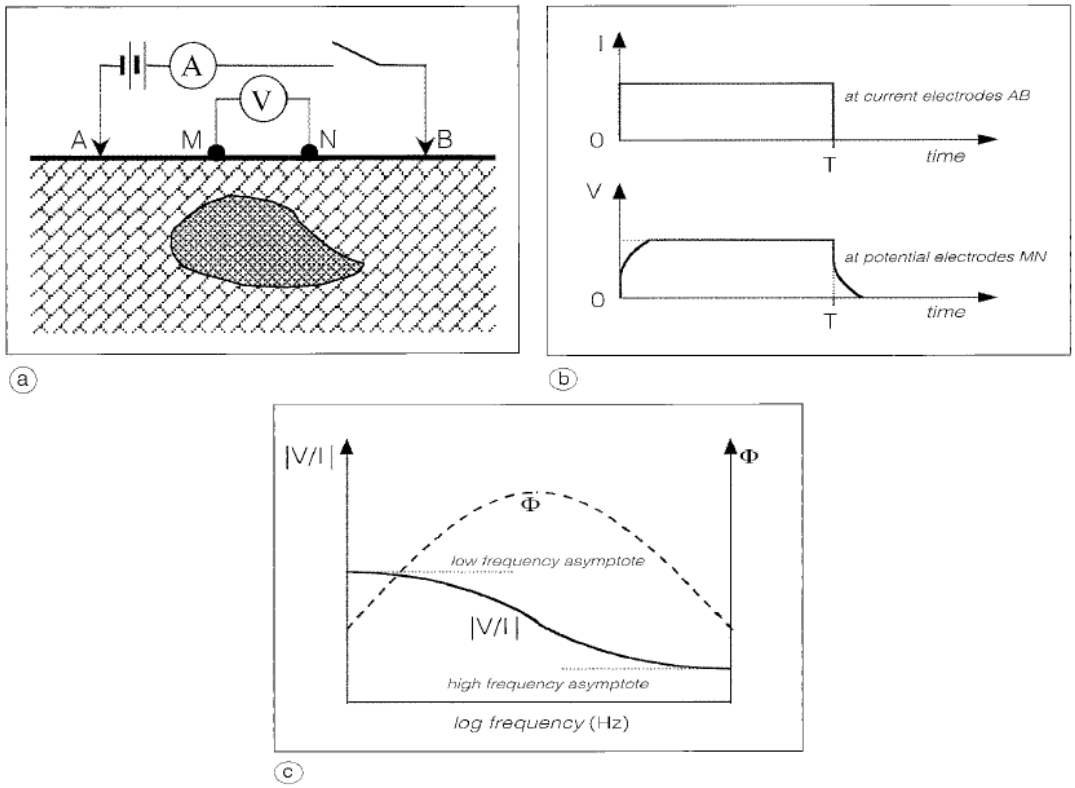

From Patella, 2003.

The types of polarization are called:

- Membrane polarization
- Electrode polarization

There are two types of membrane polarization, the first one occurs when pore space narrows to within several boundary layer thicknesses (which is the thickness of ions adsorbed

to a surface). Charges cannot flow easily, so they accumulate when an electric field is applied resulting in a net charge dipole, which adds to any other voltages measured at the surface.

A second form of membrane polarization is similar to the first: this occurs when in the rock is present a discreet and widespread distribution of clay particles. Upon application of an electric potential, positive charge carriers pass easily, while negative carriers accumulate. There is an "ion-selective membrane." A surplus of both cations and anions occurs at one end of the membrane, while a deficiency occurs at the other end.

Figure 5: (a) two types of membrane polarization, top and bottom figure respectively, (b) electrode polarization.

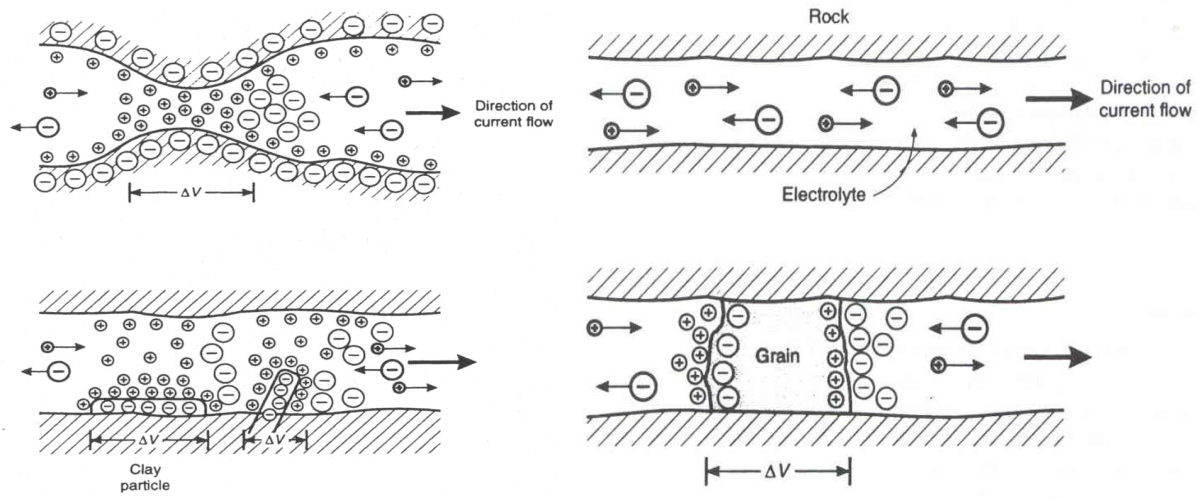

(a) **(b)**

Modified from a) Ward, 1990 b) Seigel, 1974

Electrode polarization occurs when pore space is blocked by metallic particles, as oxides or sulphides. When an electric current is applied, which is in part electrolytic and electronic, ions accumulate at the interface obstructing current flow (Snyder *et al.*, 1977), the result is two electrical double layers which add to voltages measured at the surface.

We can observe a transient potential both at the connection and at the shutdown of the circuit, the two transient phases are equivalent, but usually the discharging transient is studied because is free from the "light" of the current. The phenomenon is studied in the frequency domain applying Fourier transform of the transient in the time domain or sending alternating current at different frequencies.

To study Induced Polarization is necessary to introduce physical models that can fully represent the phenomenon. One of the models used to study IP is called Debye model and it is expressed in the following equation

$$V^D(t) = V_0 \sum_{n=1}^{N} \alpha_n \exp\left(-\frac{t}{\tau_n}\right) \tag{2.1}$$

in time domain (t), and

$$\rho_D(\omega) = \rho_0 \left(1 - \sum_{n=1}^{N} \frac{j\omega\beta_n}{1 + j\omega\tau_n}\right) \tag{2.2}$$

in the frequency domain (ω), where $\alpha_n>0$ is the amplitude of the *n*-th decay component, V_0 is the stationary value before the discharge, τ_n is the decay constant of the *n*-th exponential, $\beta_n= \alpha_n\tau_n$, ρ_0 is the resistivity in correspondence of V_0.

The Debye model is based on the assumption that underground N different ionic species are present, in equation (2.1), we observe the superposition of exponential decays and (2.2), the overlap of the individual dispersion curves.

The definition of the Debye model thus involves the determination of 2n parameters totally. Another physical model for the representation of the induced polarization phenomenon is the Cole-Cole model

$$V^{CC}(t) = mV_0 \sum_{n=0}^{\infty} \frac{(-1)^n (\frac{t}{\tau})^{nc}}{\Gamma(1 + \mathrm{nc})} \tag{2.3}$$

$$\rho^{CC}(\omega) = \rho_0 \left[1 - m \frac{(j\omega\tau)^c}{1 + (j\omega\tau)^c}\right] \tag{2.4}$$

where *m* is a measure of material polarization, $0 \leq c \leq 1$ is the frequency dependence factor, τ the time constant in seconds, which determines the length of time required for the decay, and Γ(1+*nc*) is the gamma function.

The Cole-Cole model is an empirical model with just three parameters to be determined, *m,* τ and *c*, and it can be proven that it is a continuous distribution of individual Debye models. In the recent literature we find several studies concerning the reformulation of the Debye and the Cole-Cole models (Weigand and Kemna, 2016; Gurin *at al.*, 2015). Nordsiek and Weller, for example, in 2008 proposed an alternative fitting approach for the induced-polarization spectra using the decomposition of observed IP spectra into a variety of Debye spectra. It proves to be more flexible and stable, even for complicated phase spectra that cannot be fitted by single Cole-Cole type models.

Ustra *et al*. 2016 developed an alternative formulation for Debye decomposition through laboratory tests with sand and oil mixtures undergoing microbial degradation of hydrocarbons. They determined a relaxation time distribution (RTD) and two frequency-independent parameters that modulate the complex conductivity spectra. The distribution of relaxation times quantifies the contribution of each distinct relaxation process. Each contribution can then be associated with specific polarization processes and the RTD reveals evidence of a length scale at which a new polarization process takes place as a result of the biodegradation process.

The spatial and temporal behavior of an electric field generated into polarizable rocks due to external sources is significantly different from the one expected if we consider valid Ohm's law in its basic formulation. IP phenomenon is a clear sign that the electricity conduction in the rocks is very complex and cannot be synthesized by the classical relationship:

$$\boldsymbol{J} = \sigma \boldsymbol{E} \tag{2.5}$$

where the conductivity σ is assumed to be independent from time t in TD and from frequency ω no FD. Polarization effects are observed when into the rocks there are alterations in the crystal structure due to the circulation of hydrothermal fluids, hydrocarbon migration and tectonic metamorphism.

Among the various electromagnetic prospecting methods, which in principle can report the occurrence of polarization phenomena, it is included the MT method. One of the ways in which polarization manifests itself in the rocks consists in the resistivity variation by varying the frequency of an alternating current flow passing there through (resistivity dispersion). For this reason one polarizable material opposes different resistivities at different monochromatic components of MT field.

The MT method requires an accurate analysis of the experimental data in the frequency range between 10^{-4} and 10^{4} Hz and this is precisely the range in which the dispersion phenomenon manifests if exists. It reveals itself with an anomalous behavior in the experimental data that is not justified by the classical MT theory.

An example is shown in Figure 6, from Manzella *et al*. (2004), where we can observe an anomaly in MT curves. This anomaly cannot be justified as a response to any particular geometry of the buried structure, but as a response to an abnormal physical behavior of the resistivity of the rocks.

Figure 6: Apparent resistivity and phase MT curves. Red circles indicate the presence of anomalies in the curves.

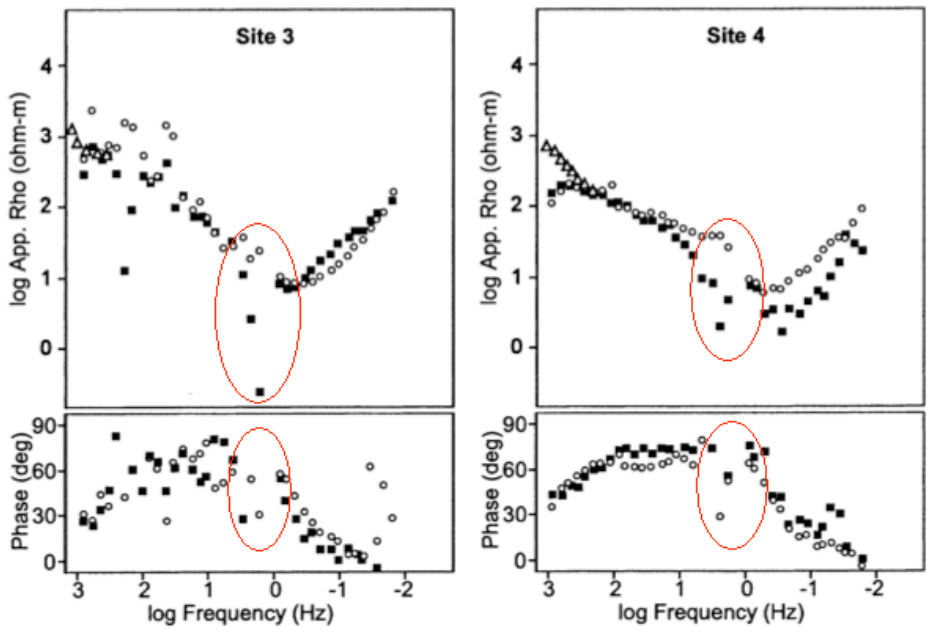

from Manzella et al., 2004.

2.3 Electrodynamic model of Induced Polarization

The polarizability of the soil is connected to the presence of saline solutions inside the rocks, of metal particles or hydrocarbons.

Among the models proposed to explain the phenomenon of IP we consider a model introduced by Patella in 2003, called electrodynamic model, which allows us to get an expression of the conductivity, then of the resistivity as a solution of a second order differential equation that describes the movement of charged particles immersed in an external electric field.

We start from the motion equation of a charged particle q immersed in an electric field E (t):

$$\sum_{\lambda=0}^{2} m_\lambda \frac{d^\lambda \boldsymbol{r}(t)}{dt^\lambda} = q\boldsymbol{E}(t) \tag{2.6}$$

where m_2 is the mass of the particle, m_1 the friction-like coefficient accounting for dissipative effects due to the collision and interaction with other charged particles, and m_0 is the elastic-like coefficient accounting for recall effects on bound charges.

In the frequency domain eq. (2.6) transforms

$$\sum_{\lambda=0}^{2} m_\lambda (i\omega)^\lambda \boldsymbol{R}(\omega) = q\boldsymbol{E}(\omega) \tag{2.7}$$

From eq. (2.7) we obtain the solution for R(ω) as

$$\boldsymbol{R}(\omega) = \frac{q}{\sum_{\lambda=0}^{2} m_\lambda (i\omega)^\lambda} \boldsymbol{E}(\omega). \tag{2.8}$$

Suppose that the system has K> 0 equal charged particles per unit of volume and that all particles of the medium behaves like a microcircuit with a current density equal to:

$$\boldsymbol{J}(\omega) = Kqj\omega\boldsymbol{R}(\omega) \tag{2.9}$$

which, using the eq.(2.8), becomes

$$\boldsymbol{J}(\omega) = \frac{j\omega Kq^2}{\sum_{\lambda=0}^{2} m_\lambda (i\omega)^\lambda}\boldsymbol{E}(\omega) \tag{2.10}$$

knowing that

$$\boldsymbol{J}(\omega) = \sigma(\omega)\boldsymbol{E}(\omega) \tag{2.11}$$

we obtain

$$\sigma(\omega) = \frac{j\omega Kq^2}{\sum_{\lambda=0}^{2} m_\lambda (i\omega)^\lambda}. \tag{2.12}$$

Equation (2.12) describes a circuit-like cell with a resistance-capacitance-inductance series combination. Physically this circuit represents the presence of moving charges (R) bound charges (C) and heavy charges (L) i.e. with considerable inertia.

It is possible to classify circuit behavior in the three following modes:

1) if there are only charges "light" and not "bound", i.e. only subject to viscous friction forces, dominant over inertia and Coulomb force, the behavior is purely Ohmic, that speaking in terms of circuit corresponds to a resistance R;

2) if there are charges "light" and "bound", i.e. only subject to Coulomb force, dominant over inertia and viscous friction force, the behavior is capacitive and corresponds to a capacitance C;

3) if, finally, charges are "heavy" and not "bound", i.e. subject only to inertial forces, dominant on purely viscous friction and Coulomb force, the behavior is inductive, that corresponds to the circuit element of inductance L.

From a geological point of view, it can be assumed that “heavy” charges in solution are due to hydrocarbon pollution or heavy metal ions (industrial residues as lead, zinc and mercury poured into the soil or into groundwater).

If we imagine a purely resistive circuit, i.e., $\omega m_2 << m_1$ and $m_0 << \omega m_1$, equation (2.12) reduces to

$$\sigma(\omega) = \frac{Kq^2}{m_1} \tag{2.13}$$

which represents the Ohmic conductivity.

When $\omega m_1 << m_0$ and $m_0 << \omega_2 m_2$ equation (2.12) becomes

$$\sigma(\omega) = \frac{j\omega Kq^2}{m_0}. \tag{2.14}$$

In this case, the elastic term is dominant and the circuit is purely capacitive. If $m_1 << \omega m_2$ and $m_0 << \omega_2 m_2$ eq. (2.12) is reduced to

$$\sigma(\omega) = \frac{Kq^2}{j\omega m_2}, \tag{2.15}$$

that represents the conductivity of a pure inductive circuit.

Because of the complexity of the porous structure of rocks and the various combinations of ionic species in the fluid, it is easy to realize that various types of forces may

prevail in different ways, giving rise to a more complex circuit behavior with series or parallel combinations of the elements just described.

2.4 Dispersion models

From a work of Patella of 2008 we consider five different dispersion laws. From equation (2.6) that describes the particles motion immersed in an external electric field, we arrive to the following expression for the conductivity

$$\sigma(\omega) = \frac{j\omega K q^2}{m_0 + j\omega m_1 - \omega^2 m_2} \tag{2.16}$$

and hence the resistivity

$$\rho(\omega) = \frac{m_0 + j\omega m_1 - \omega^2 m_2}{j\omega K q^2}. \tag{2.17}$$

The resistivity and the conductivity are called respectively impedivity and admittivity in the frequency domain (Patella 1987).

From this expression that describes the overall behavior of a RLC series circuit we obtain the following dispersion models:

1. the positive non-resonant model, in which real and imaginary part of the admittivity are positive;
2. the negative non-resonant model, in which real part of admittivity is positive and imaginary part is negative;
3. the resonant model, in which both real and imaginary part of the admittivity present a resonant peak;
4. the resonant positive model, in which the resonance is superimposed on the positive dispersion effect;
5. the resonant positive model, in which the resonance is superimposed on the positive dispersion effect;

6. the resonant positive model, in which the resonance is superimposed on the positive dispersion effect;
7. and the resonant negative model, in which the resonance is superimposed on the negative dispersion effect.

In the case of non-resonant model one of the ion species consists of charges subject to frictional force (R) and the other species is characterized by "light" charges subject to both frictional forces and Coulomb force (RC). In other words one branch (R) represents the path which the unbound light ions run through, with instantaneous constant speed, under the action of the external exciting field. The other branch (RC) represents the path the bound light ions can move through, under the action of the same external field and against the decelerating recall forces.

In the non-resonant negative model one of the two species is formed by charges subject to frictional force (R) as in the previous case, and the other has "heavy" charges subject to the forces of inertia and friction (RL). In this case the second branch (RL) simulates the accelerated path the unbound heavy ions can travel through, subject to the external field.

In the resonant model one of the two species, as in the two previous cases, consists of "light" and "bound" charges (R) and the second one composed by "heavy" charges subject to all three kinds of forces: inertia, friction and Coulomb force (RCL).

In membrane polarization bound charges are represented by clay particles that with their negative charge distribution in the rock pores delay the flow of the positive ions (cations) in the solution because of Coulomb force. In electrode polarization instead the metal particles obstructing the pores block the ions in the fluid solution.

2.4.1 Non-resonant positive model

In the case of non-resonant positive model the conductivity is

$$\sigma^{(+)}(\omega) = \frac{K_1 q_1^2}{m_{11}} + \frac{j\omega K_2 q_2^2}{m_{02} + j\omega m_{12}}. \qquad (2.18)$$

using

$$\sigma_1 = \frac{K_1 q_1^2}{m_{11}}, \tag{2.19}$$

$$\sigma_2 = \frac{K_2 q_2^2}{m_{12}}, \tag{2.20}$$

$$\gamma_2 = \frac{m_{02}}{m_{12}}, \tag{2.21}$$

we obtain

$$\sigma^{(+)}(\omega) = \frac{\sigma_1 \gamma_2 + j\omega(\sigma_1 + \sigma_2)}{\gamma_2 + j\omega}. \tag{2.22}$$

Generalizing for a parallel combination of N microcircuits we obtain

$$\sigma^{(+)}(\omega) = \sum_{n=1}^{N} \frac{\sigma_{1n}\gamma_{2n} + j\omega(\sigma_{1n} + \sigma_{2n})}{\gamma_{2n} + j\omega} \tag{2.23}$$

for a series combination instead we have

$$\rho^{(+)}(\omega) = \sum_{n=1}^{N} \frac{\gamma_{2n} + j\omega}{\sigma_{1n}\gamma_{2n} + j\omega(\sigma_{1n} + \sigma_{2n})} \tag{2.24}$$

where the symbol (+) is indicating we are considering the positive model.

Equation (2.24) represents the positive non-resonant model of IP, real and imaginary parts are plotted in Figure 7.

Figure 7: Positive non-resonant model diagram. The real and imaginary parts of the conductivity are expressed in Siemens/m, log frequency in Hz.

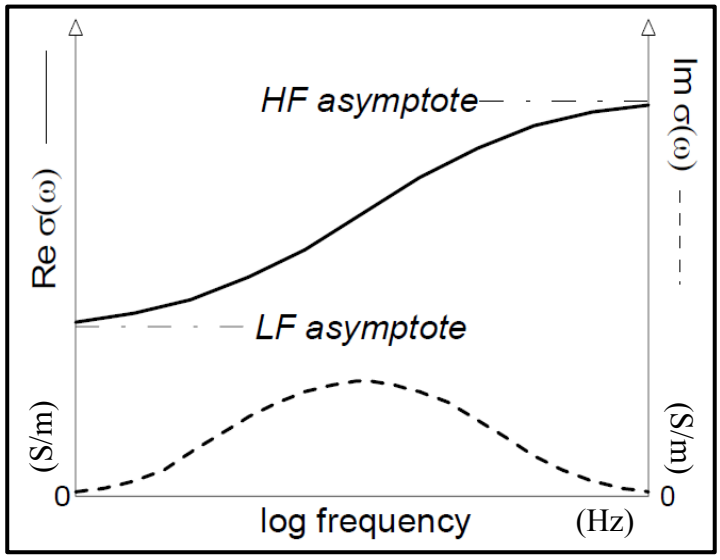

from Patella 2008.

The real part of conductivity is always positive and has two asymptotes; the one at high frequency is at a higher level than the asymptote at low frequency.

The imaginary part, which is also always positive tends to zero at both low and high frequency, and has a maximum in correspondence to inflection point of real part.

Posing now

$$\rho_0 = \lim_{\omega \to 0} \rho^{(+)}(\omega) = \sum_{n=1}^{N} (1/\sigma_{1n}), \tag{2.25}$$

$$\tau_n = \frac{\sigma_{1n} + \sigma_{2n}}{\gamma_{2n}\sigma_{1n}}, \tag{2.26}$$

$$\beta_n = \frac{\sigma_{2n}}{\rho_0 \gamma_{2n} \sigma_{1n}^2}, \tag{2.27}$$

the equation (2.24) can be written as

$$\rho^{(+)}(\omega) = \rho_0 \left(1 - \sum_{n=1}^{N} \frac{j\omega\beta_n}{1 + j\omega\tau_n} \right) \tag{2.28}$$

which is exactly the Debye model.

However is the Cole-Cole model (Cole and Cole, 1941) to be widely used in the analysis of IP after Pelton et al. (1983), and it is the one used in the theoretical simulations of this work (2.29) in the following form

$$\rho^{CC}(\omega) = \rho_0 \left[1 - m\frac{(j\omega\tau)^c}{1 + (j\omega\tau)^c}\right]. \qquad (2.29)$$

The parameter $m \in [0, 1]$ is called chargeability and has the following meaning: for $m \Rightarrow 0$ the soil is less polarizable, vice versa for $m \Rightarrow 1$.

2.4.2 Non-resonant negative model

In the literature, the phenomenon of negative IP has not been considered a physical effect, an intrinsic property of earth materials. Instead, it is viewed as a geometrical effect due to the mutual arrangement between the measuring device and the polarized medium (Sumner 1967; Bertin and Loeb, 1976; Nabighian and Elliot, 1976; Wait, 1982), or as an effect due to inductive coupling between the transmitter and the receiver circuit (Bertin and Loeb, 1976), or additionally as an effect due to current leakage of the transmitter circuit in proximity of the receiver circuit (Cantwell and Madden, 1976).

But it is known that the negative dispersion is an intrinsic property of electrons in metals at wavelengths smaller than 10^{-2} cm (Stratton, 1941), therefore to consider a negative IP model may actually provide information about the properties of the subsoil.

Let's consider once again the system with two different ionic species, in this case the two species are mobile and just one of them has heavy ions. These ions have not negligible inertia, thus generating the equivalent RL effect. As mentioned before from a geological point of view the presence of heavy charges is connected to the presence of hydrocarbons or heavy metal ions.

Then the conductivity expression in this case is

$$\sigma^{(-)}(\omega) = \frac{K_1 q_1^2}{m_{11}} + \frac{K_2 q_2^2}{m_{12} + j\omega m_{22}} \tag{2.30}$$

using (2.19), (2.20) and

$$\lambda_2 = \frac{m_{22}}{m_{12}}, \tag{2.31}$$

we obtain

$$\sigma^{(-)}(\omega) = \frac{(\sigma_1 + \sigma_2) + j\omega\lambda_2\sigma_1}{1 + j\omega\lambda_2}. \tag{2.32}$$

The equation (2.32) represents IP non-resonant negative model, real and imaginary parts are plotted in Figure 8.

Figure 8: Negative non-resonant model diagram. The real and imaginary parts of the conductivity are expressed in Siemens/m, log frequency in Hz.

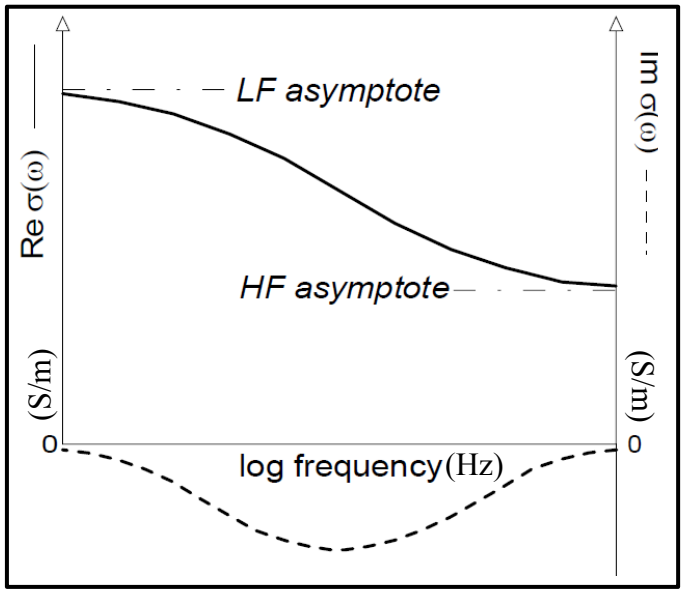

from Patella 2008.

We can notice that the real part is always positive, as in the non-resonant positive model, but the asymptotes are reversed, the asymptote at low frequencies is at higher level than the one at high frequencies. The imaginary part is negative and, as in the previous case, it tends to zero for $\omega \rightarrow 0, \infty$, having a minimum in correspondence of the inflection point of real part.

In this case the expression of Cole-Cole resistivity is (Esposito and Patella, 2009)

$$\rho^{(-CC)}(\omega) = \rho_0 \left[\frac{1 + (j\omega\tau)^c}{1 + (j\omega m^{(-)}\tau)^c} \right], \tag{2.33}$$

with $c \in [0, 1]$ and $m \in [0, 1]$.

2.4.3 Resonant positive and negative models

The case of resonance occurs when one of the two ionic species has considerable inertia. We assume that the microcircuit, formed by two branches in parallel, in one branch behaves as a single resistance (R), and in the other branch as a combination of RLC in series.

The resistivity expression is

$$\sigma^{rf}(\omega) = \frac{K_1 q_1^2}{m_{11}} + \frac{j\omega K_2 q_2^2}{m_{02} + j\omega m_{12} - \omega^2 m_{22}}. \tag{2.34}$$

Using equations (2.19), (2.20), (2.21), and (2.34) we have

$$\sigma^{rf}(\omega) = \frac{\sigma_1(\gamma_2 - \omega^2\lambda_2) + j\omega(\sigma_1 + \sigma_2)}{\gamma_2 + j\omega - \omega^2\lambda_2} \tag{2.35}$$

where σ_1 and σ_2 are expressed in S/m, λ_2 in seconds and γ_2 in Hz.

Equation (2.35) represents IP resonant model (Patella, 2008), of which the real and imaginary parts are plotted in Figure 9.

Figure 9: Resonant model diagram. The real and imaginary parts of the conductivity are expressed in Siemens/m, log frequency in Hz.

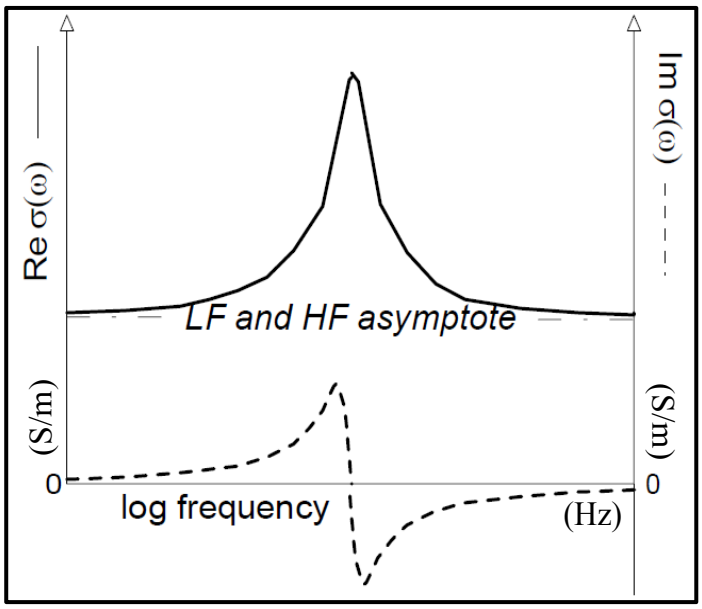

from Patella 2008.

The real part of conductivity is always positive, but in this case the low-frequency asymptote is at the same level of high frequency asymptote and the curve shows a maximum in correspondence of the resonance frequency $\omega = (\gamma_2/\lambda_2)^{1/2}$. The imaginary part, as in the previous cases, goes to zero for $\omega \rightarrow 0, \infty$, and has a positive peak followed by a negative peak in correspondence of the resonance frequency. From the graph, it can be deduced that the effect of resonance can be considered as a combination of a positive and a negative effect.

To conclude, we show the resonance superimposed on either a positive or a negative dispersion effect. Supposing the presence of three different ionic species (i = 1,2,3) and a behavior as a circuit having three branches in parallel, the first branch (i = 1) is constituted by a single resistance (R), the second branch (i = 2) as RC in series (positive model) or RL (negative model), the third branch (i = 3) as a RLC in series.

Conductivities are

$$\sigma^{(r+)}(\omega) = \frac{\sigma_1\gamma_2 + j\omega(\sigma_1 + \sigma_2)}{\gamma_2 + j\omega} + \frac{j\omega\sigma_3}{\gamma_3 + j\omega - \omega^2\lambda_3} \tag{2.36}$$

and

$$\sigma^{(r-)}(\omega) = \frac{(\sigma_1 + \sigma_2) + j\omega\lambda_2\sigma_1}{1 + j\omega\lambda_2} + \frac{j\omega\sigma_3}{\gamma_3 + j\omega - \omega^2\lambda_3} \tag{2.37}$$

where σ_1, σ_2 and σ_3 are expressed in S/m, λ_2, λ_3 in seconds and γ_2, γ_3 in Hz.

We observe in figures 10 and 11 the real and imaginary parts.

Figure 10: Resonant positive diagram. The real and imaginary parts of the conductivity are expressed in Siemens/m, log frequency in Hz.

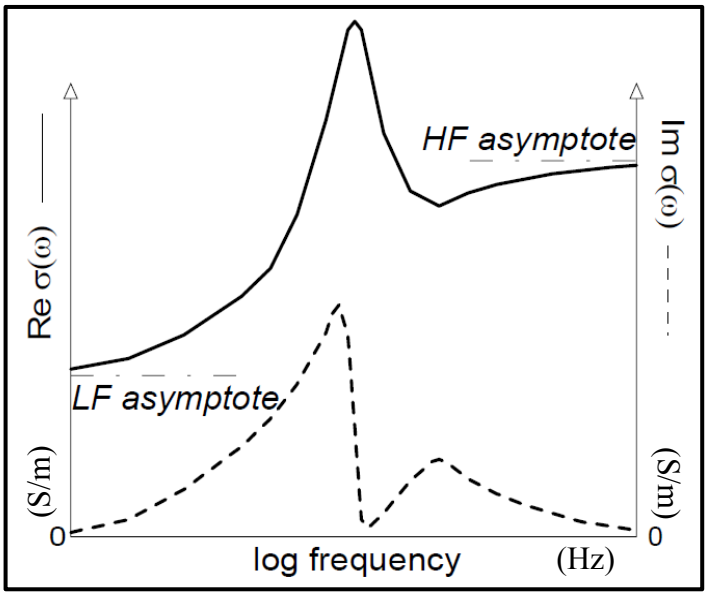

from Patella 2008.

Figure 11: Resonant negative diagram. The real and imaginary parts of the conductivity are expressed in Siemens/m, log frequency in Hz.

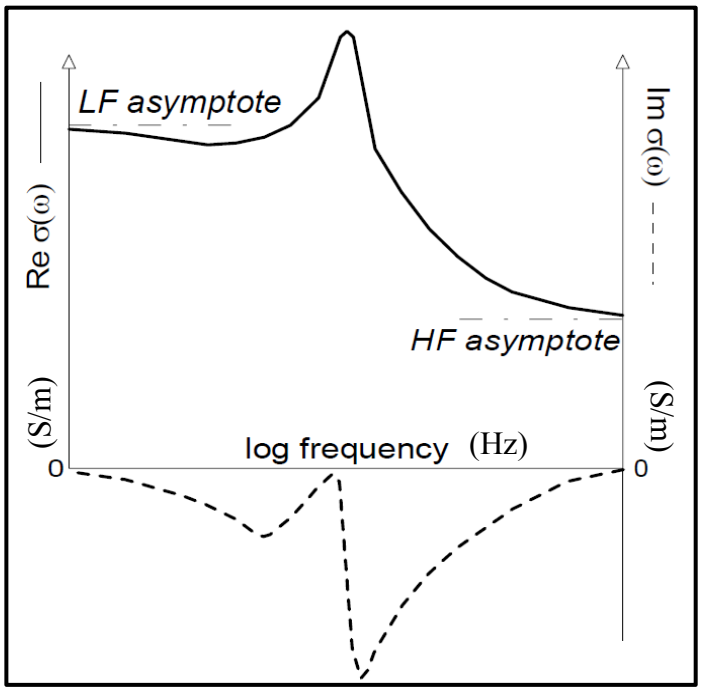

from Patella 2008.

The dispersion models shown are representative of different geological environments. Positive non-resonant dispersion effects in MT were experimentally recognized in volcanic and geothermal areas (Di Maio *et al.*, 1997; Di Maio *et al.*, 2000; Giammetti *et al.,* 1996; Mauriello *et al.*, 2000; Mauriello *at el.,* 2004; Patella *et al.,* 1991).

Negative non-resonant dispersion introduces the possibility of explaining negative chargeability values, known in metals at high frequency, also as an intrinsic physical effect in some earth materials; for example in near-surface applications, negative IP effects might be interpreted as indicators of the presence of heavy ionic contaminants in sediments (Patella, 2008).

Resonant effects are connected to the presence of heavy particles into the subsurface therefore they can verify of in presence of hydrocarbon or metals into the soil or groundwater.

2.5 MT dispersive response for a 1-D and a 2-D earth model

In the following paragraph we report the work of Esposito, R. and Patella, D., 2009 in which are shown in detail the five dispersion models, previously described, in the case of a 1-D layered earth with the second layer affected by resistivity dispersion, which is characterized by the Cole-Cole dispersive functions.

The response curves are calculated through the expression, shown in the equation (2.38), of apparent impedivity in MT for a n-layered dispersive earth (following the theory of Patella 1993).

$$\rho_a^d(\omega) = \rho_1(\omega) tanh^2 \left\{ k_1 h_1 + tanh^{-1} \left[\frac{\sqrt{\rho_2(\omega)}}{\sqrt{\rho_1(\omega)}} tanh \left\{ k_2 h_2 + tanh^{-1} \left[\frac{\sqrt{\rho_3(\omega)}}{\sqrt{\rho_2(\omega)}} \right. \right. \right. \right.$$
$$\left. \left. \left. \left. \cdot tanh \left\{ k_3 h_3 + \cdots \right. \right. \right. \right.$$
$$\left. \left. \left. \left. + tanh^{-1} \left[\frac{\sqrt{\rho_{n-1}(\omega)}}{\sqrt{\rho_{n-2}(\omega)}} \cdot tanh \left\{ k_{n-1} h_{n-1} + tanh^{-1} \left[\frac{\sqrt{\rho_n(\omega)}}{\sqrt{\rho_{n-1}(\omega)}} \right] \right\} \cdots \right] \right\} \right. \right. \right. \right. \quad (2.38)$$

where k_1 and k_2 are the wavenumbers of the first and the second layer, given by $k_1 = \sqrt{(i\omega\mu_0/\rho_1)}$ and $k_2 = \sqrt{(i\omega\mu_0/\rho_2)}$, respectively, being μ_0 the magnetic permeability of the vacuum, equal to $4\pi * 10^{-7}$ H/m in SI units.

The impedivity $\rho_2(\omega)$ of the second layer is given, separately, by the expressions in Eqs. (2.29) and (2.33), and the inverse of the expressions in Eqs. (2.35), (2.36) and (2.37).

2.5.1 1-D earth model

Four combinations of three layers were considered A, Q, H, K, all with the intermediate layer dispersive, or polarizable.

The resistivity and thickness values of the layers are illustrated in Figure 12.

Figure 12: The three-layer A, Q, H and K type sections used for all of the dispersive MT simulations, ρ is the resistivity of the layers and t is the thickness.

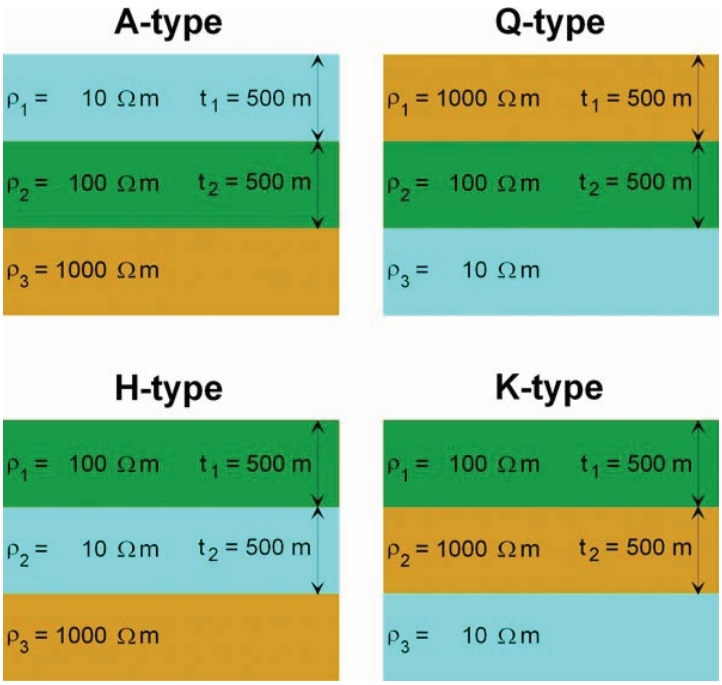

Simulations were performed using the software MATLAB 7.12.0 and in this work we report the most significant results, i. e. where the most significant variations in MT curves are observed (with growing chargeability m respectively, 0.1, 0.5, 0.9, for positive and negative, 0.1, 0.01, 0.001, non-resonant models and different γ, 1Hz, 10Hz, 100Hz, in the three resonant models). The values of the parameters m indicate the degree of polarizability of the soil while γ values are directly connected to the interaction of ionic species in solution. It is not so easy to associate a certain parameter value to a specific geological environment, certainly the presence of saline solutions, hot fluids or sulfides (Pelton, 1978) increase the soil chargeability, so high value of m for the positive non-resonant case and low value of m for the negative non-resonant case are meaningful of these types of alterations. Figures 13, 14, 15, 16 and 17 show the influence of polarization in the MT responses.

In all sets of curves there are always plotted for comparison the responses of MT non-dispersive models.

Figure 13: MT apparent impedivity modulus and phase simulated responses for the A, Q, H and K three-layer sequences of Fig. 12, with the second layer affected by a Cole-Cole type non-resonant positive. The black lines are the reference not dispersive MT responses. The flatting factor and principal time constant are fixed, respectively c+ = 0,75 and τ+ = 100s, while the positive dispersion amplitude is variable with values m+ = 0.1 (red lines), m+= 0.5 (green lines) and m+ = 0.9 (blue lines).

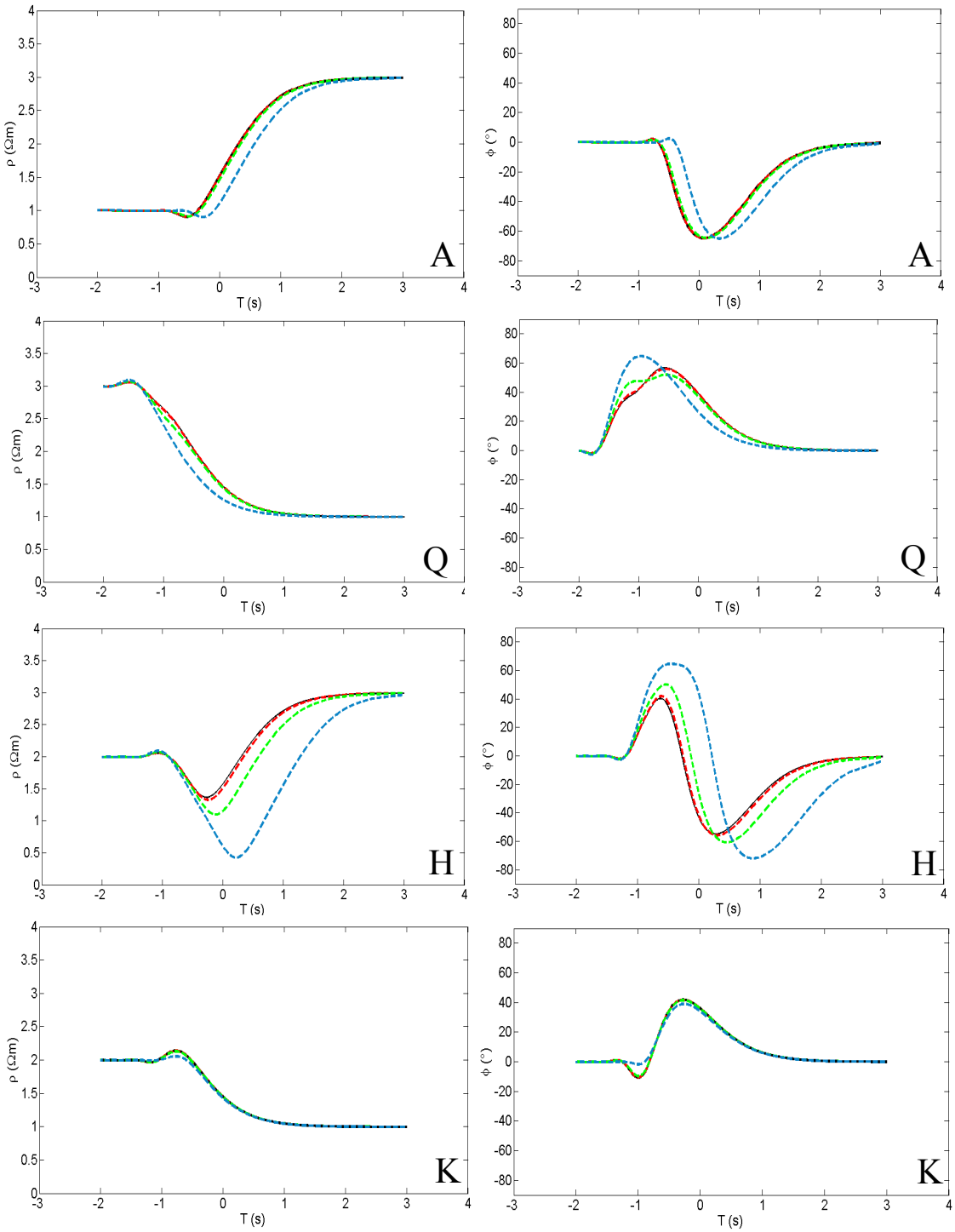

Figure 14: MT apparent impedivity modulus and phase simulated responses for the A, Q, H and K three-layer sequences of Fig. 12, with the second layer affected by a Cole-Cole type non-resonant negative dispersion. The black lines are the reference not dispersive MT responses. The flatting factor and principal time constant are fixed, respectively c- = 0,75 e τ- = 100s, while the negative dispersion amplitude is variable with values m- = 0.001 (red lines), m- = 0.01 (green lines) e m- = 0.1(pink lines).

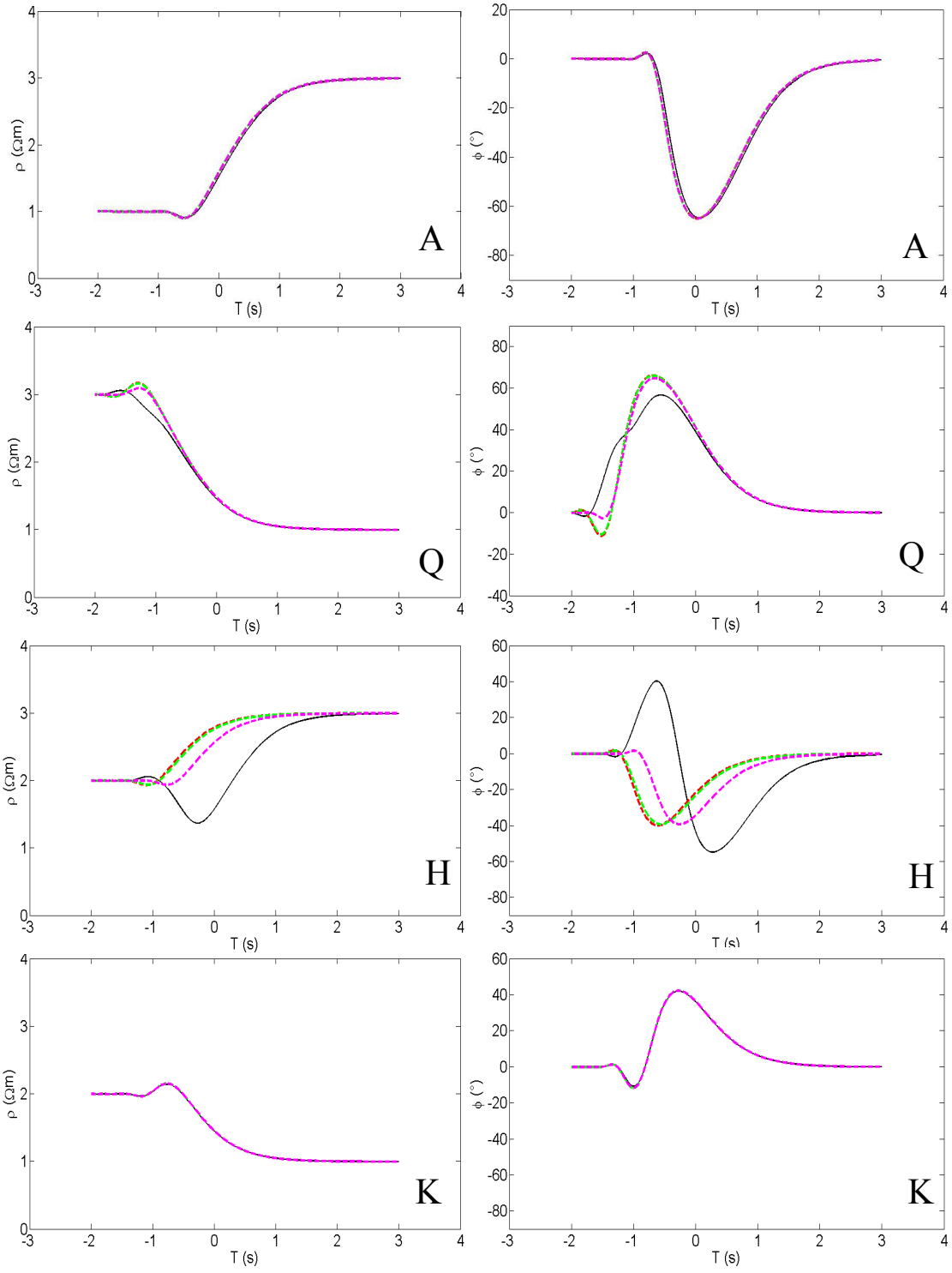

Figure 15: MT apparent impedivity modulus and phase simulated responses for the A, Q, H and K three-layer sequences of Fig. 12, with the second layer affected by a resonant flat dispersion. The black lines are the reference not dispersive MT responses. Fixed parameters are σ2 = 0.1 S/m and λ_2 = 10 s, while the variable parameter is γ_2 = 1Hz(red lines), γ_2 = 10Hz (green lines) and γ_2 = 100 Hz (blue lines).

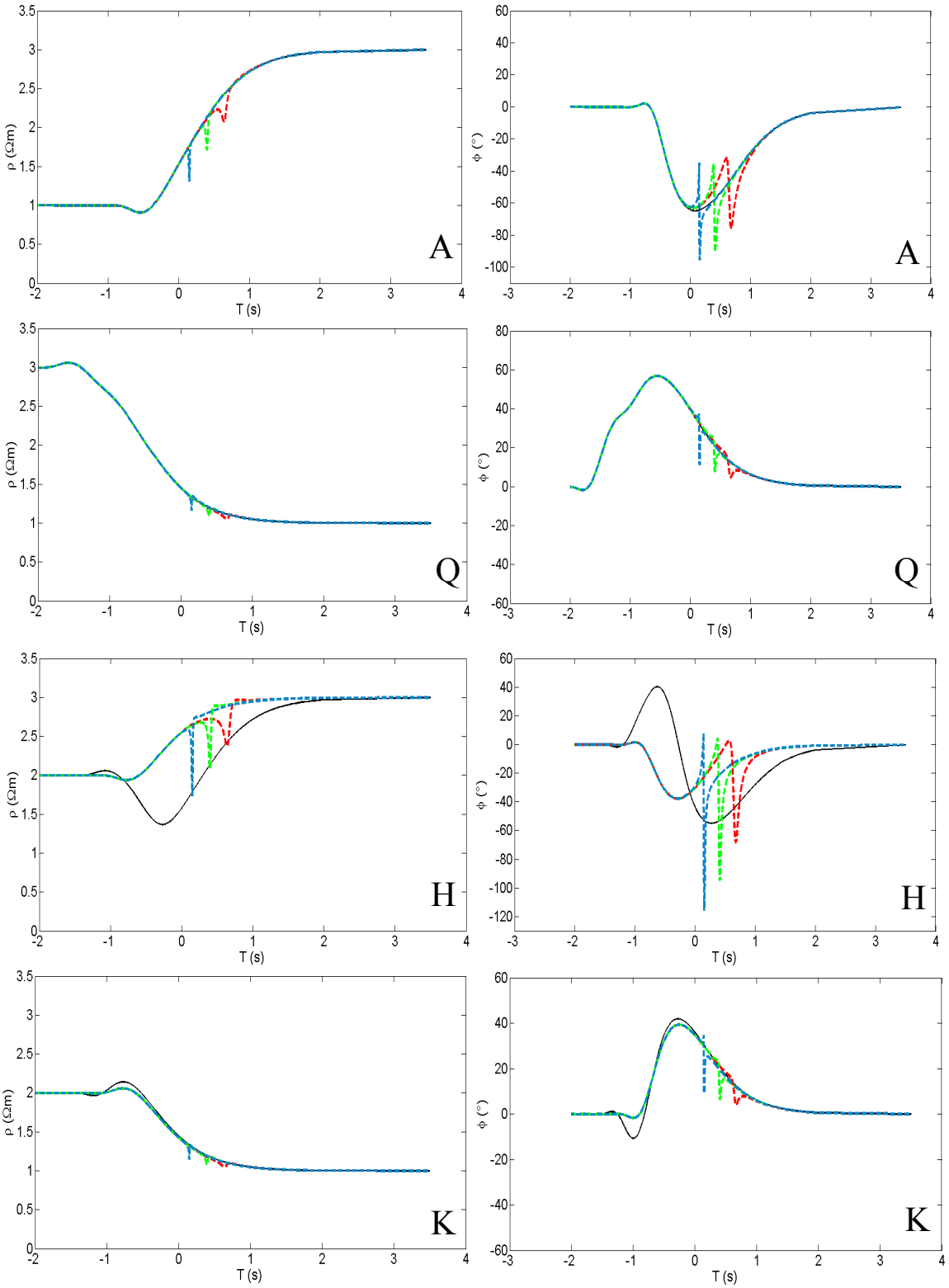

Figure 16: MT apparent impedivity modulus and phase simulated responses for the A, Q, H and K three-layer sequences of Fig. 12, with the second layer affected by a resonant positive dispersion. The black lines are the reference dispersion-free MT responses. The positive dispersion amplitude, flatting factor and time constant parameters are m+ = 0.5, c+ = 1 and τ+ = 1000 s, respectively. Fixed are also σ3 = 0.1 S/m and λ3 = 10 s, while the variable parameter is γ3 = 1 Hz (red lines), γ3 = 10Hz (green lines) and γ3 = 100 Hz (pink lines).

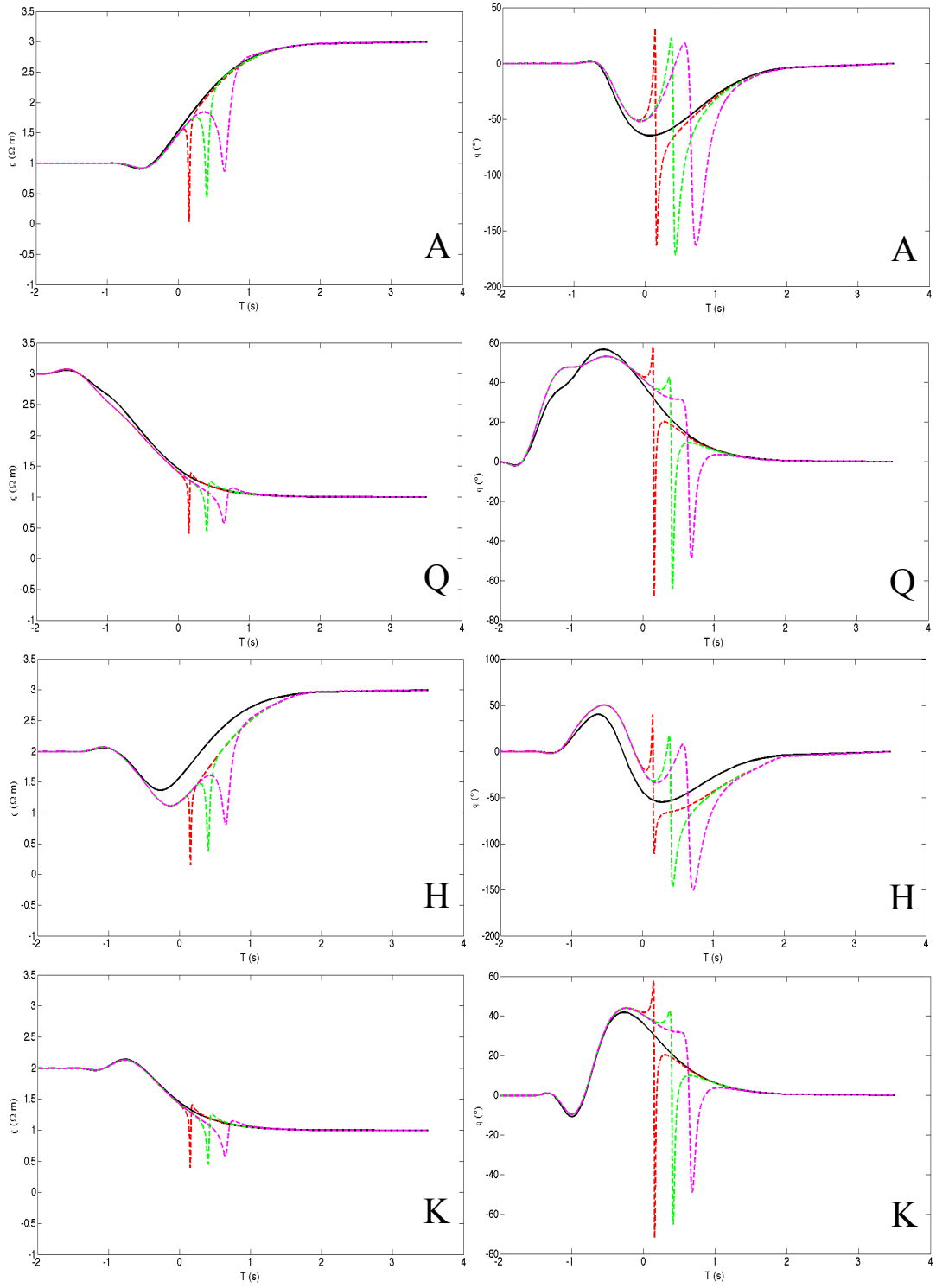

Figure 17: MT apparent impedivity simulated responses for the A, Q, H and K three-layer sequences of Fig. 12, with the second layer affected by a resonant negative dispersion. The black lines are the reference dispersion-free MT curves. The negative dispersion amplitude, flatting factor and time constant are m− = −1, c− = 1 and τ− = 500 s, respectively. Fixed are also σ3 = 0.1 S/m and λ3 = 10 s, while the variable parameter is γ3 = 1 Hz (red lines), γ3 = 10Hz (green lines) and γ3 = 100 Hz (pink lines).

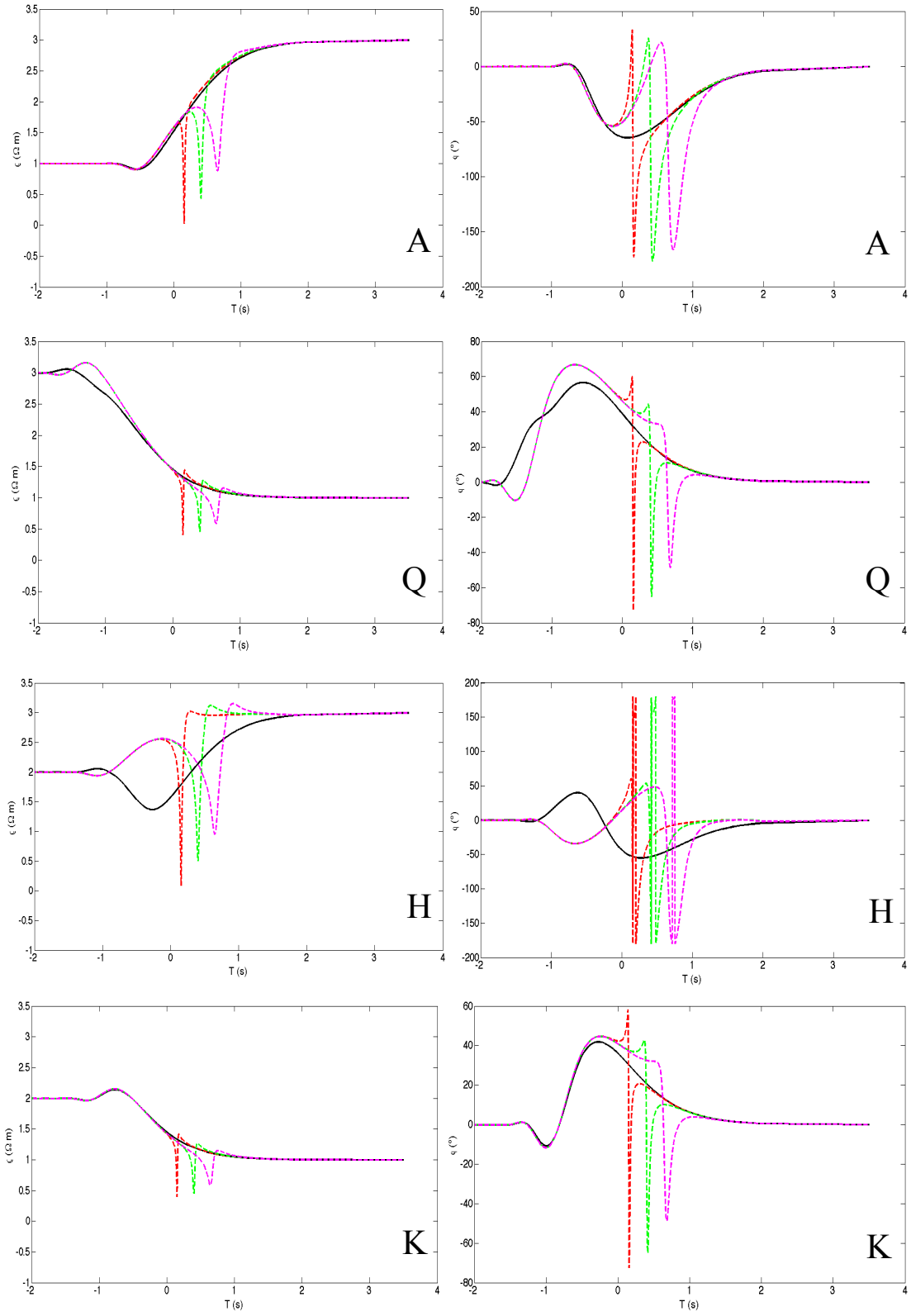

The most significant deformation is shown in Fig. 14 between the curves with the lowest value of *m* and the one with the biggest value of *m*.

It is noteworthy that sequence of type H was shown to be the most frequent model in oil and geothermal explorations (Pellerin, 1996; Zhdanov, 1994). In fact, strong scattering phenomena can occur in a permeable rock, underlying a cover layer, because of the diffuse presence of mineral particles and clay particles formed by the aggressive action of fluids that are rising from an underlying reservoir.

If there is no certainty that data acquisition were made in a polarizable soil, the interpretation of curves can be easily incorrect.

To demonstrate the equivalence problem that can occur we show an example of two MT response curves of two types of earth, one with two layers without dispersion of resistivity and the other with three layers, with the second layer being dispersive, specifically affected by a negative non-resonant type of dispersion. The solid curve is the response curve is the reference three-layer non-dispersive earth (Fig. 18).

From the Fig. 18 it is clear that the responses of the two layers earth without dispersion and the ones of the three layers earth with negative non-resonant dispersion appear identical. For this reason MT measurements alone cannot distinguish in which of the two cases we are, making necessary the combination of MT with a direct-current prospecting method. An electric sounding is free from dispersion, as it operates in a nearly steady state regime, by constructing synthetic MT non-dispersive diagrams from a preliminary DES (Dipole Electric Survey) interpretation, it is possible to evidence dispersion effects from the comparison between the true MT diagrams and the synthetic ones (Patella, 1987).

In the resonant case instead, both positive and negative, we can clearly notice the presence of a more or less marked resonance peak in MT curves characteristic, which can make more recognizable the presence of dispersion.

Figure 18: (a) The two Earth models considered for the simulations below: the two layers dispersion-free model and the three layers with second layer being dispersive (b) MT responses: the black lines are the reference apparent impedivity modulus and phase curves for the dispersion-free H-type model drawn in Fig. 12 The red lines are the apparent impedivity modulus and phase responses for the same H-type sequence, with the second layer affected by a non-resonant negative dispersion, with parameters m− = 0.1, c− = 1 and τ− = 100 s. The blue lines are the corresponding curves for the dispersion-free two-layer sequence with ρ1 = 100 Ωm, ρ2 = 1000Ωm and thickness t1 = 500 m.

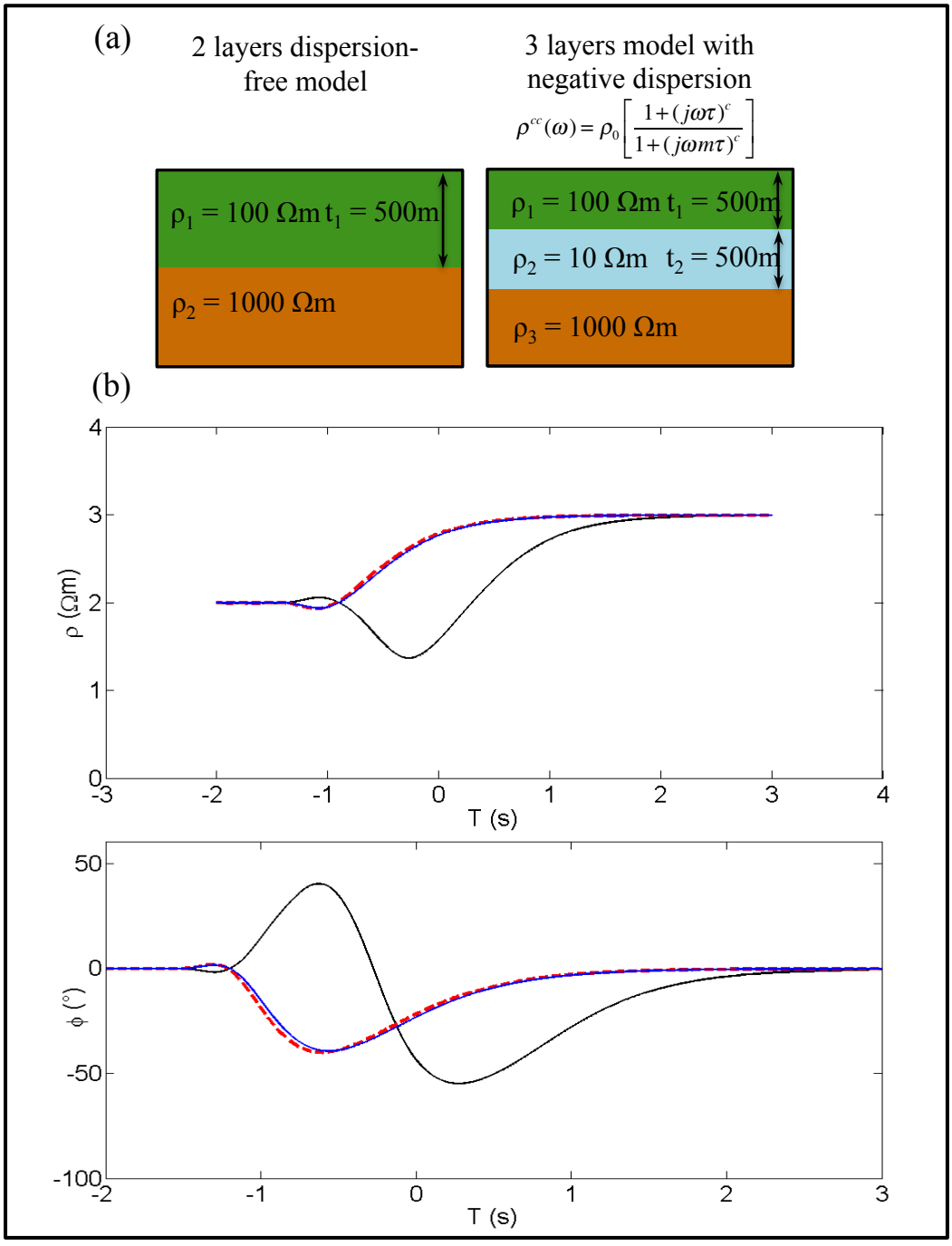

2.5.2 2-D earth model

The magnetotelluric response over 2-D media with resistivity frequency dispersion has already been studied from Mauriello *et al.*, 1996 that investigated the surface MT responses of three real geological situations representing a sedimentary basin, a geothermal system and a magma chamber, assumed to be dispersive.

For further information we decided to perform two 2-D inversions of a synthetic data set derived from a 2-D Earth model, considered both non dispersive and dispersive. We studied a simple case of a conductive body immersed in a more resistive environment that can be appropriate to represent the characteristics of a magma chamber. The conductive body with resistivity of 10 Ωm has dimensions of 2x2km (lateral and vertical extensions), it is located at a depth of 1km in a host material of 200 Ωm of resistivity and it is centered with respect to a 7 km long profile with 15 MT stations which spaced 500m one from each other (Fig. 19).

In this simulation we performed a 2-D inversion with synthetic data originated from the forward 2-D model responses considering the body affected by resistivity dispersion. The MT responses of the forward 2-D model and the 2-D inversion have been performed with the software WinGLinK 2.01.01.

Simulations are made considering the buried body both non-dispersive and dispersive to observe the difference in MT responses.

Figure 19: 2D Earth model, the red body buried into the ground is considered dispersive. At the surface the MT stations are indicated by the black triangles.

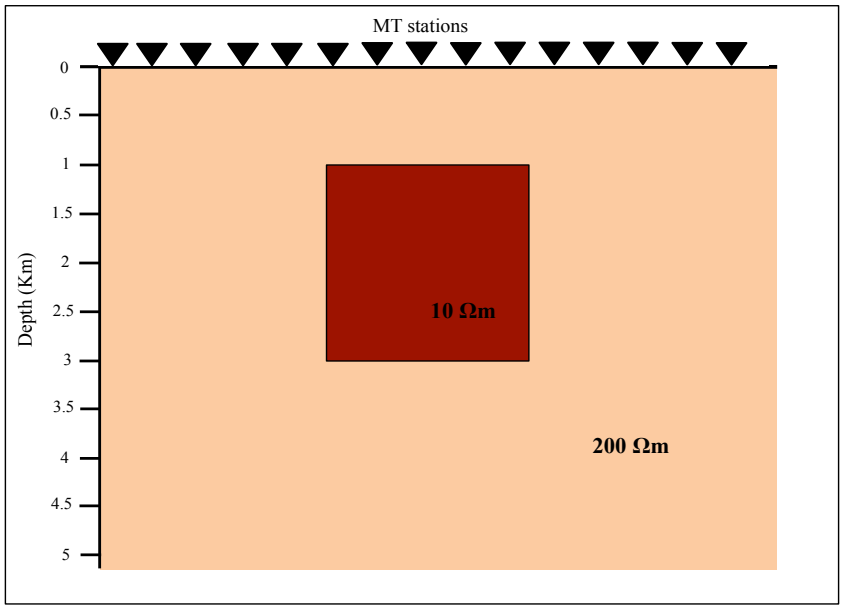

The first step consisted in running a forward 2-D model to obtain the theoretical MT non-dispersive curves for the 2-D earth model showed in Figure 19, then using the positive Cole-Cole dispersion model reported in the Eq. (2.39) we calculated the resistivity value that the body exhibits, at a defined frequency (for instance 10Hz), with the parameters $c = 0.75$, $m = 0.9$ and $\tau = 100$s (chosen according to the 1-D simulations), and we run again the forward 2D model to obtain the correspondent MT curves.

$$\rho^{CC}(\omega) = \rho_0 \left[1 - m\frac{(j\omega\tau)^c}{1 + (j\omega\tau)^c}\right]. \tag{2.39}$$

We have repeated this procedure for sixteen different values of frequency from a value of 0.001 Hz until a few hundreds of Hertz.

As an example, in Fig. 20, we show the MT responses at three different stations of the profile, the first one located in the proximity of the border of the body, the second one centered with respect to the lateral extension of the conductive body and the third one positioned 2km far away from body border.

Once we have replaced the resistivity of the body with the Cole-Cole resistivity we run the forward 2-D model procedure for each of the sixteen values. From the apparent resistivities and phases resulting from the direct modeling procedure, we constructed the MT curves having a resistivity has a function of the frequency.

The MT curves so constructed have been used as the input for the 2-D inversion; in order to understand which Earth model solution we reach. The results of the 2-D inversion are shown in Fig. 21 and Fig. 22, for the non-dispersive case and the dispersive case respectively, considering an error of 10% on the resistivity values and phases for both TE and TM mode.

As we can see clearly from the two figures the input MT curves lead to a two slightly different Earth models, in the dispersive case the body appears bigger in the lateral dimension and more conductive.

Figure 20: Apparent resistivity and phase curves for the 2-D Earth model of Fig. 19. (a) MT responses for the station close to the body border, (b) MT responses for the station centered with respect to the lateral extension of the body (c) MT responses for the station positioned 2km far away from the body border. TE and TM mode are plotted, blue curves represent the model without dispersion, and red curves the model with dispersion.

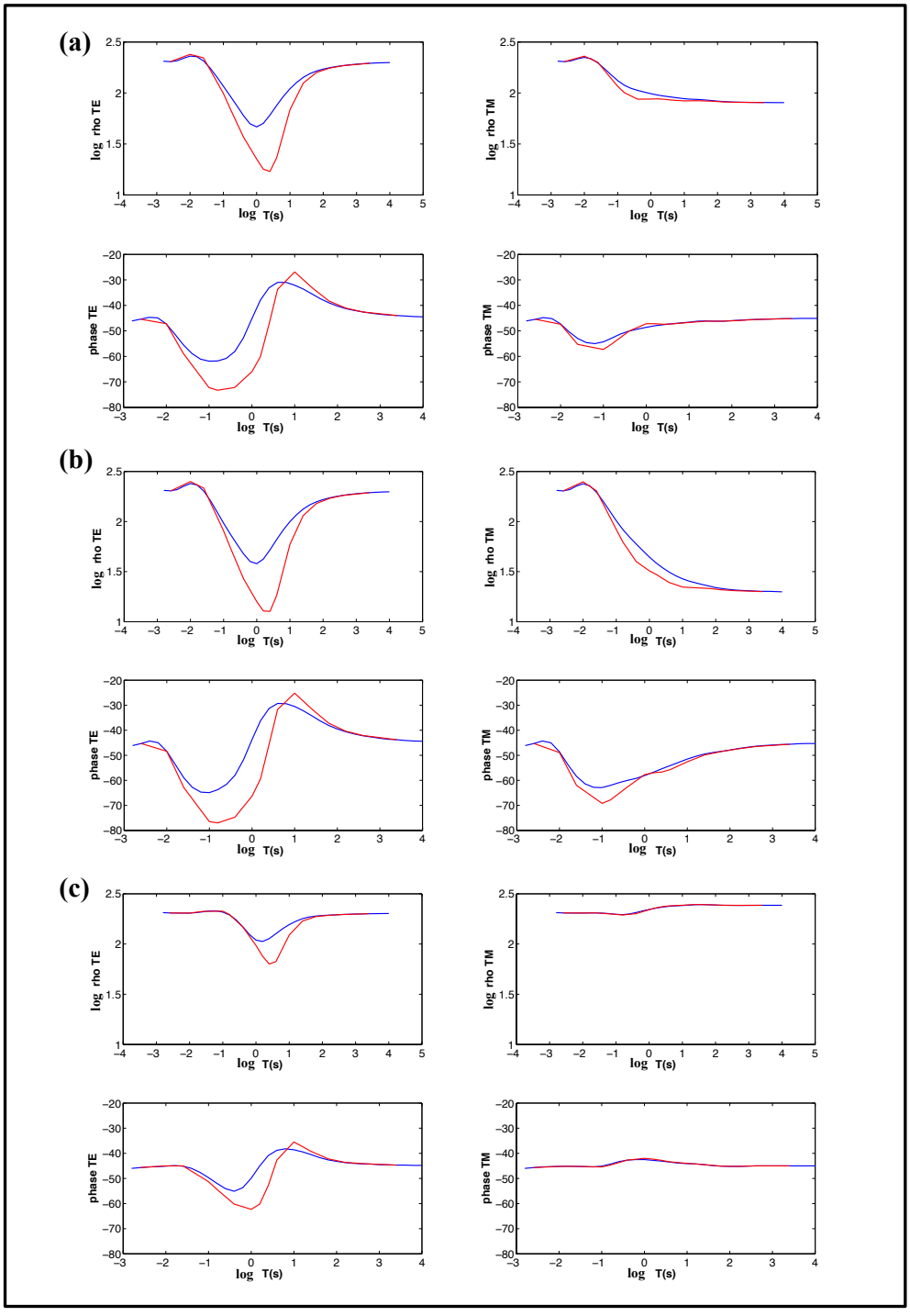

Figure 21: Calculated resistivity model from inversion of synthetic MT data. Non-dispersive case.

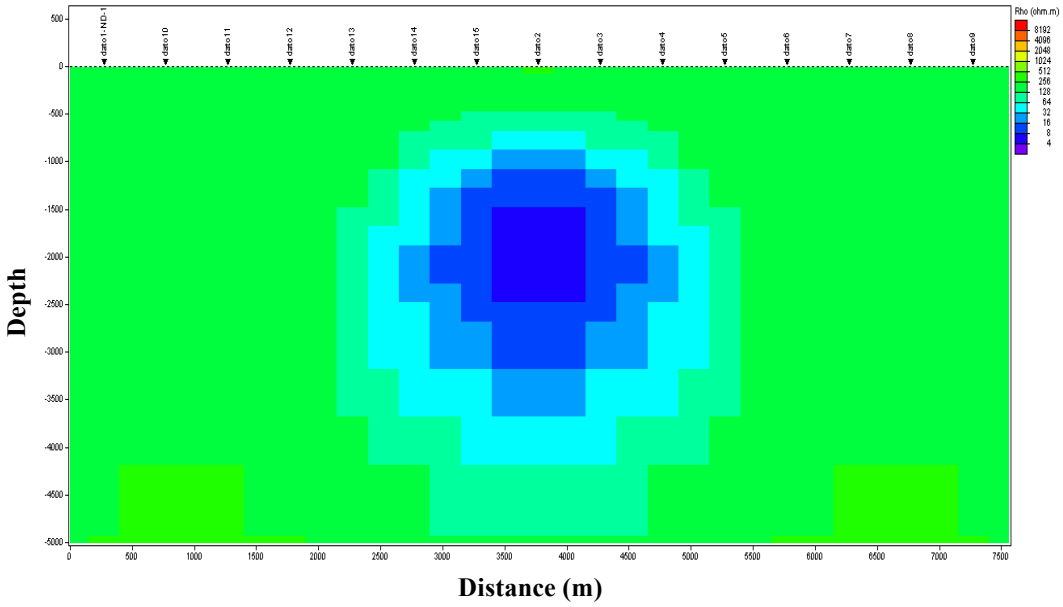

Figure 22: Calculated resistivity model from inversion of synthetic MT data. Dispersive case.

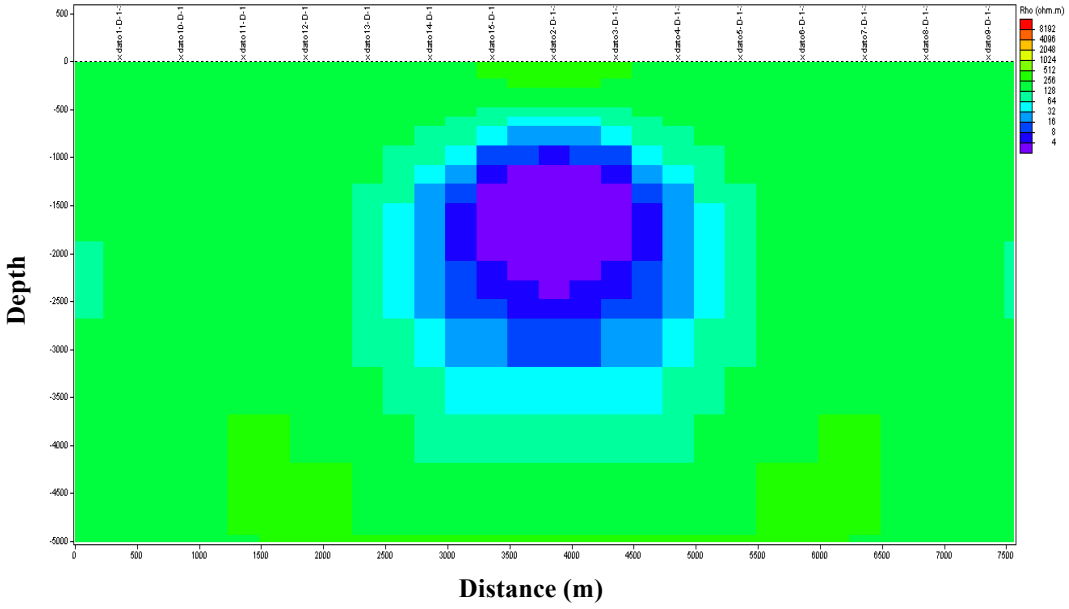

3 THE MAGNETOTELLURIC RESPONSE OVER A 3-D POLARIZABLE STRUCTURE

In this chapter we show the MT responses in the case of a 3-D dispersive structure. The MT curves at the surface are obtained from the 3-D forward modeling code, named MTD3FWD, developed by Randy Mackie and implemented into the 3D modeling program WINGLINK 2.01.01. The forward modeling code computes magnetic and electric fields at the surface of a 3-D electrical resistivity model crossed by electromagnetic plane waves, the fields computed are converted to magnetotelluric impedances and consequently to resistivity and phase curves at the stations contained in the mesh area.

3.1 3-D simulation of dispersive effects in MT

In Fig. 23 we present the 3D model assumed for the simulations. A horizontal dispersive prism with resistivity ρ_0=10 Ωm is buried in a non-dispersive half-space with resistivity of 200 Ωm. The 3D body has horizontal length of 6 km along the *y*-axis and square edges of 2x2 km^2. The top face is located at 2 km depth.

Figure 23: The 3D model and the selected profiles with corresponding station sites on the left, on the right the model seen from above.

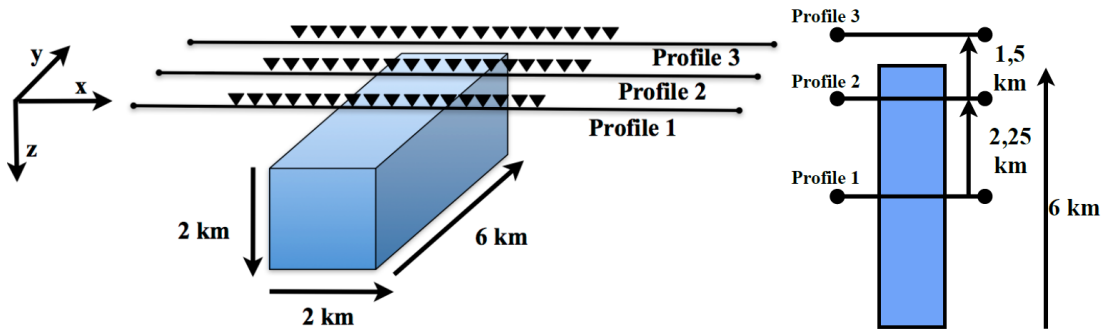

The simulations have been done along three 8 km long profiles parallel to the *x*-axis. Profile 1 crosses the prism's mid-length, profile 2 is 2250 m apart from profile 1, and profile 3 is 1500m apart from profile 2 (Fig. 23). 17 MT station points, spaced 500 m from each other, have been assumed along the profiles. The frequencies 10, 1, 0.1, 0.01 and 0.001 Hz have

been taken to plot modulus and phase of the MT apparent impedivity functions of the TE and TM modes, in order to show how IP alters the MT profiles at decreasing frequency, *i.e.* at increasing penetration depth.

As in the 2-D Earth model simulations we used the positive Cole-Cole dispersion model reported in the Eq. (2.39) with the parameters c = 0.75, m = 0.9 and τ = 100s, and we calculated the resistivity value that the body exhibits, at a defined frequency, specifically at 10, 1, 0.1, 0.01 and 0.001 Hz. For each of the resistivity value assigned to the body we run the forward 3-D model to obtain the MT curves plotting modulus and phase of the MT apparent impedivity functions of the TE and TM modes, in order to show how IP alters the MT profiles at decreasing frequency, *i.e.* at increasing penetration depth.

For the sake of conciseness, only one example of simulation is presented, which refers to the following Cole-Cole parameter set for the dispersive prism: m=0.9, τ=10 s and c=0.75 (Fig.24 through Fig.38). In all figures, the blue line refers to the reference non-dispersive case and the red lines to the dispersive assumption.

Profile 1

Figure 24: Modulus (top diagrams, in Ωm) and phase (bottom diagrams, in deg.) of the two orthogonal TM and TE modes of the MT apparent impedivity response against distance (in m) along the profile 1, calculated at the frequency of 10 Hz. The blue curves refer to the reference not dispersive response, while the red curves to the dispersive case.

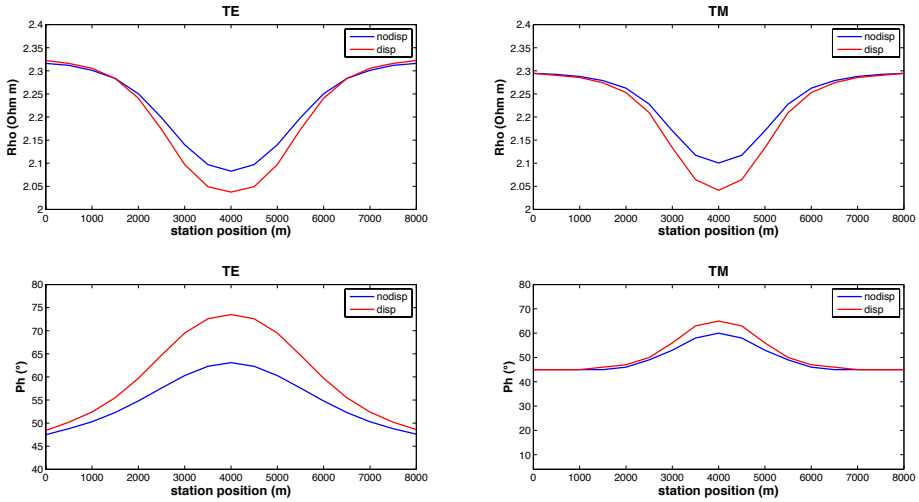

Figure 25: Modulus (top diagrams, in Ωm) and phase (bottom diagrams, in deg.) of the two orthogonal TM and TE modes of the MT apparent impedivity response against distance (in m) along the profile 1, calculated at the frequency of 1 Hz. The blue curves refer to the reference not dispersive response, while the red curves to the dispersive case.

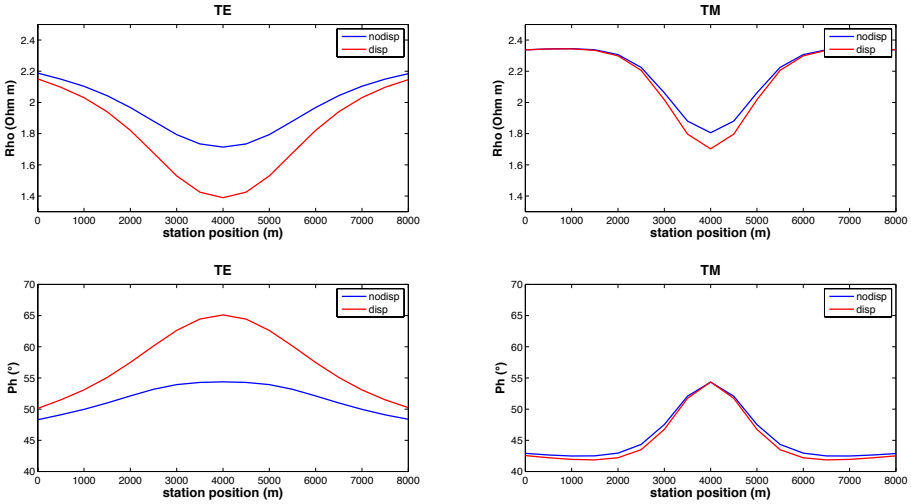

Figure 26: Modulus (top diagrams, in Ωm) and phase (bottom diagrams, in deg.) of the two orthogonal TM and TE modes of the MT apparent impedivity response against distance (in m) along the profile 1, calculated at the frequency of 0.1 Hz. The blue curves refer to the reference not dispersive response, while the red curves to the dispersive case.

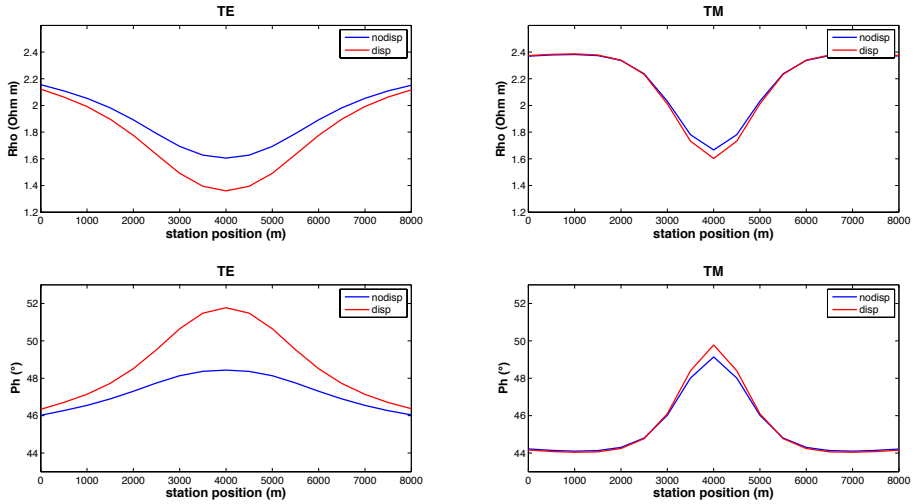

Figure 27: Modulus (top diagrams, in Ωm) and phase (bottom diagrams, in deg.) of the two orthogonal TM and TE modes of the MT apparent impedivity response against distance (in m) along the profile 1, calculated at the frequency of 0.01 Hz. The blue curves refer to the reference not dispersive response, while the red curves to the dispersive case.p

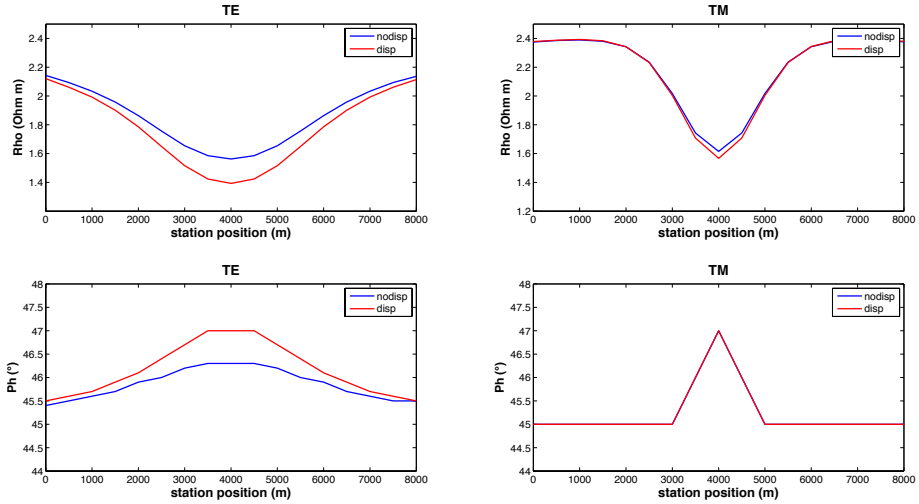

Figure 28: Modulus (top diagrams, in Ωm) and phase (bottom diagrams, in deg.) of the two orthogonal TM and TE modes of the MT apparent impedivity response against distance (in m) along the profile 1 calculated at the frequency of 0.001 Hz. The blue curves refer to the reference not dispersive response, while the red curves to the dispersive case.

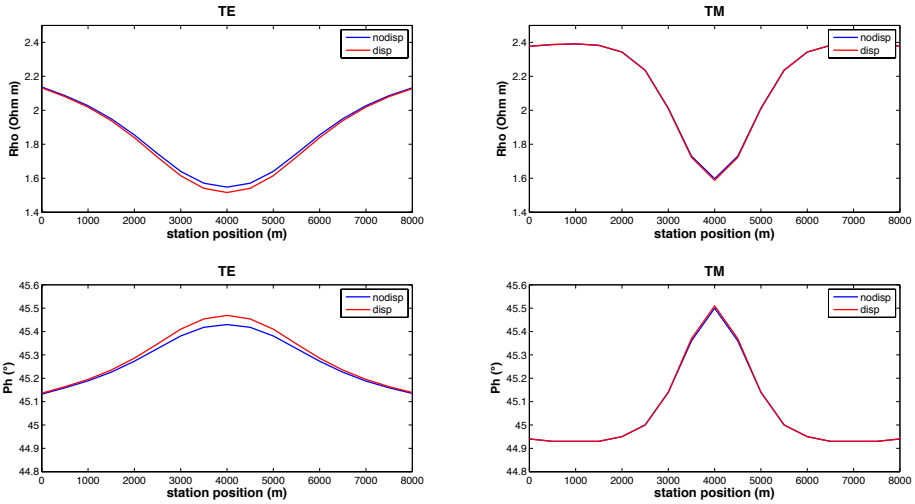

Along the profile 1, centered over the prism (Fig.28 to Fig.32), the departure of the red lines from the reference blue lines, for both modulus and phase of the TE and TM modes, is very evident. The IP effect manifests with a more pronounced minimum of both the TE and TM apparent impedivity modulus, centered above the median axis of the 3D dispersive body.

T The departure from the reference non-dispersive profiles starts to grow from 10 Hz, reaches its maximum at 1 Hz, then slowly decreases as frequency decreases, until it almost disappears at 0.001 Hz. A specular character is observed in the phase curves, where the dispersion-related red lines show a magnified maximum with respect to the non-dispersive reference blue lines. For all frequencies the more vigorous effect is observed in the TE mode.

Profile 2

Figure 29: Modulus (top diagrams, in Ωm) and phase (bottom diagrams, in deg.) of the two orthogonal TM and TE modes of the MT apparent impedivity response against distance (in m) along the profile 2, calculated at the frequency of 10 Hz. The blue curves refer to the reference not dispersive response, while the red curves to the dispersive case.

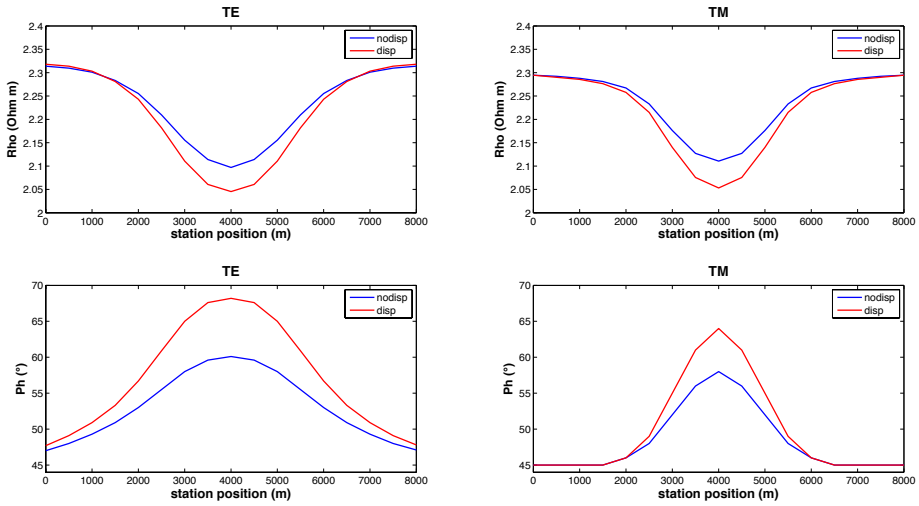

Figure 30: Modulus (top diagrams, in Ωm) and phase (bottom diagrams, in deg.) of the two orthogonal TM and TE modes of the MT apparent impedivity response against distance (in m) along the profile 2 calculated at the frequency of 1 Hz. The blue curves refer to the reference not dispersive response, while the red curves to the dispersive case.

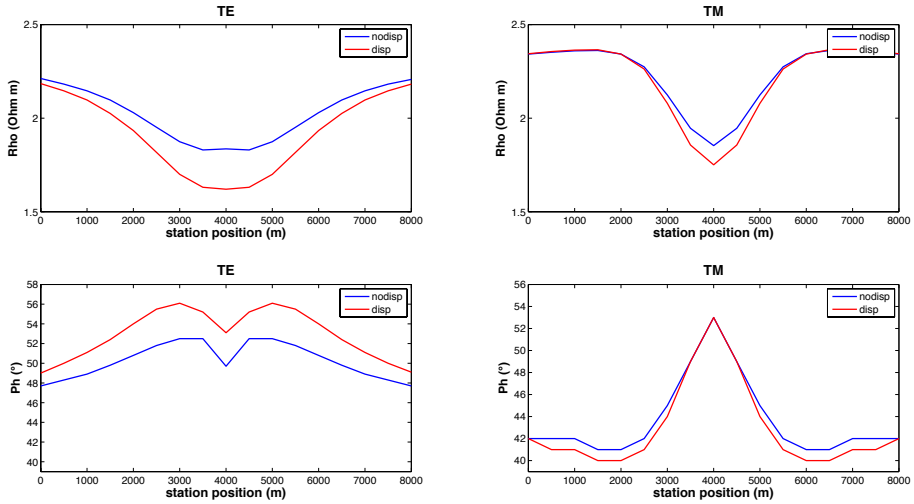

Figure 31: Modulus (top diagrams, in Ωm) and phase (bottom diagrams, in deg.) of the two orthogonal TM and TE modes of the MT apparent impedivity response against distance (in m) along the profile 2 calculated at the frequency of 0.1 Hz. The blue curves refer to the reference not dispersive response, while the red curves to the dispersive case.

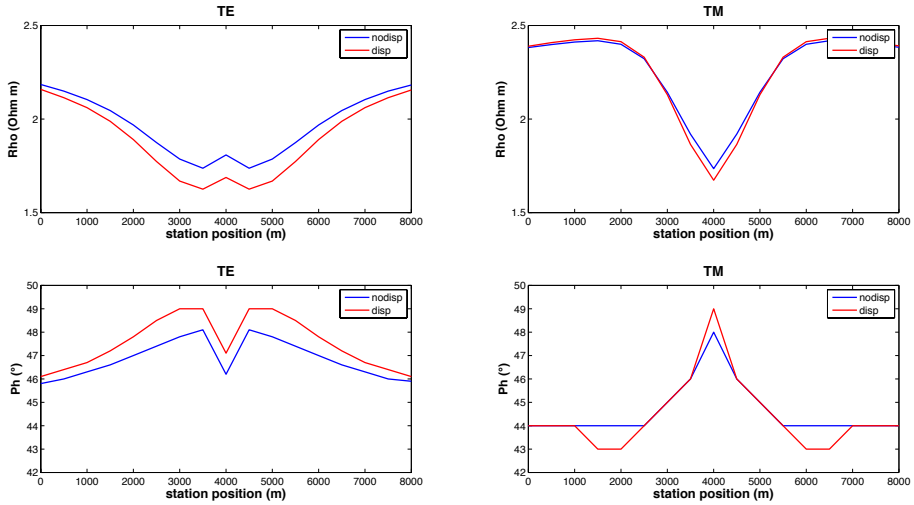

Figure 32: Modulus (top diagrams, in Ωm) and phase (bottom diagrams, in deg.) of the two orthogonal TM and TE modes of the MT apparent impedivity response against distance (in m) along the profile 2 calculated at the frequency of 0.01 Hz. The blue curves refer to the reference not dispersive response, while the red curves to the dispersive case.

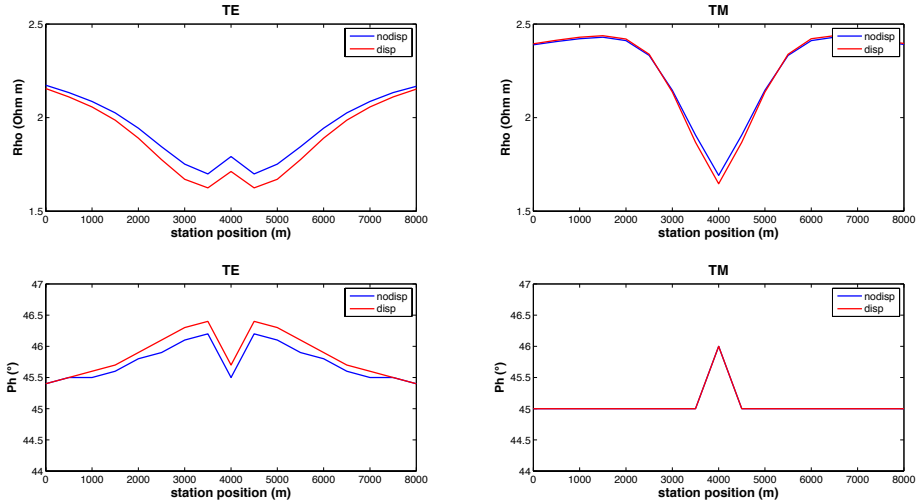

Figure 33: Modulus (top diagrams, in Ωm) and phase (bottom diagrams, in deg.) of the two orthogonal TM and TE modes of the MT apparent impedivity response against distance (in m) along the profile 2 calculated at the frequency of 0.001 Hz. The blue curves refer to the reference not dispersive response, while the red curves to the dispersive case.

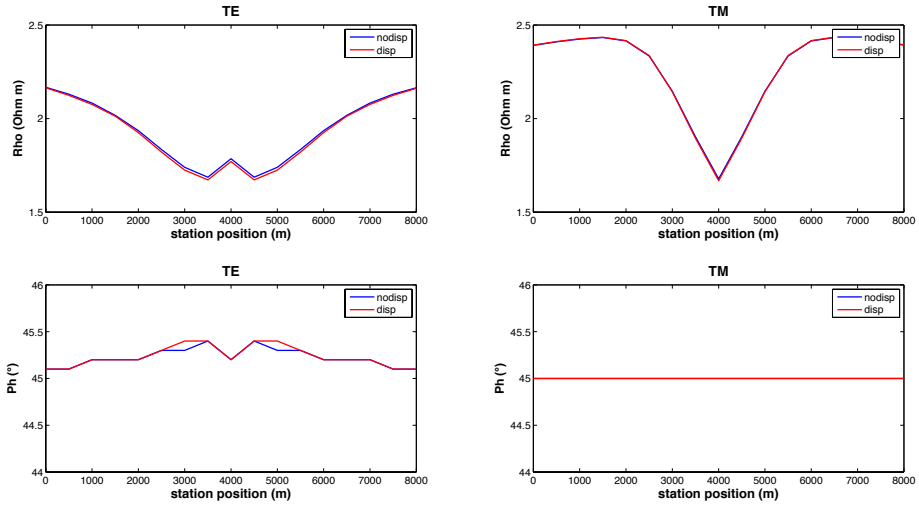

Along the profile 2, the behavior of the curves appears similar to that along the profile 1. However, two differences can readily be envisaged. The first one is that the departure of the dispersive red curves from the non-dispersive blue curves is less pronounced than in the previous case. The second difference regards mainly the TE mode and does not depend on dispersion. It consists in a symmetrical slope reversal in the central portion of the anomaly, with appearance of peaks in correspondence of the median longitudinal axis of the prism. This effect is likely due to the influence of the nearer vertical square face of the prism.

Profile 3

Figure 34: Modulus (top diagrams, in Ωm) and phase (bottom diagrams, in deg.) of the two orthogonal TM and TE modes of the MT apparent impedivity response against distance (in m) along the profile 3 calculated at the frequency of 10 Hz. The blue curves refer to the reference not dispersive response, while the red curves to the dispersive case.

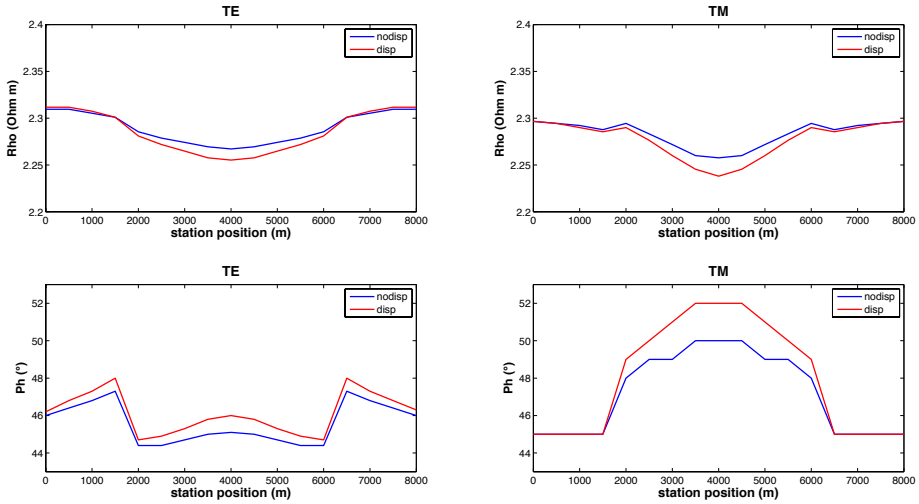

Figure 35: Modulus (top diagrams, in Ωm) and phase (bottom diagrams, in deg.) of the two orthogonal TM and TE modes of the MT apparent impedivity response against distance (in m) along the profile 3 calculated at the frequency of 1 Hz. The blue curves refer to the reference not dispersive response, while the red curves to the dispersive case.

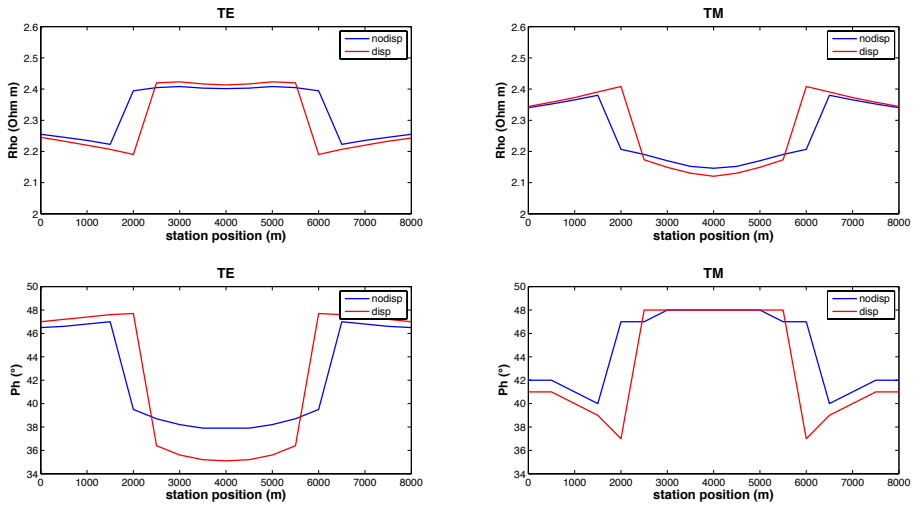

Figure 36: Modulus (top diagrams, in Ωm) and phase (bottom diagrams, in deg.) of the two orthogonal TM and TE modes of the MT apparent impedivity response against distance (in m) along the profile 3 calculated at the frequency of 0.1 Hz. The blue curves refer to the reference not dispersive response, while the red curves to the dispersive case.

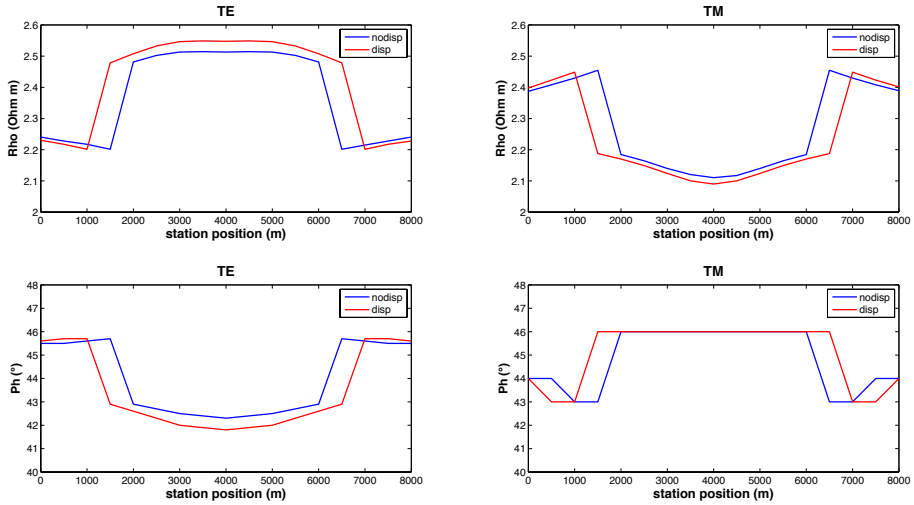

Figure 37: Modulus (top diagrams, in Ωm) and phase (bottom diagrams, in deg.) of the two orthogonal TM and TE modes of the MT apparent impedivity response against distance (in m) along the profile 3 calculated at the frequency of 0.01 Hz. The blue curves refer to the reference not dispersive response, while the red curves to the dispersive case.

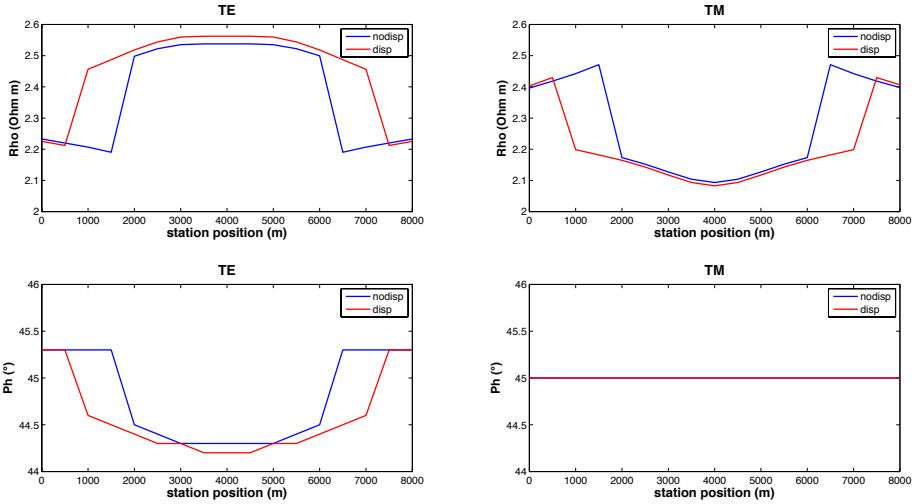

Figure 38: Modulus (top diagrams, in Ωm) and phase (bottom diagrams, in deg.) of the two orthogonal TM and TE modes of the MT apparent impedivity response against distance (in m) along the profile 3 calculated at the frequency of 0.001 Hz. The blue curves refer to the reference not dispersive response, while the red curves to the dispersive case.

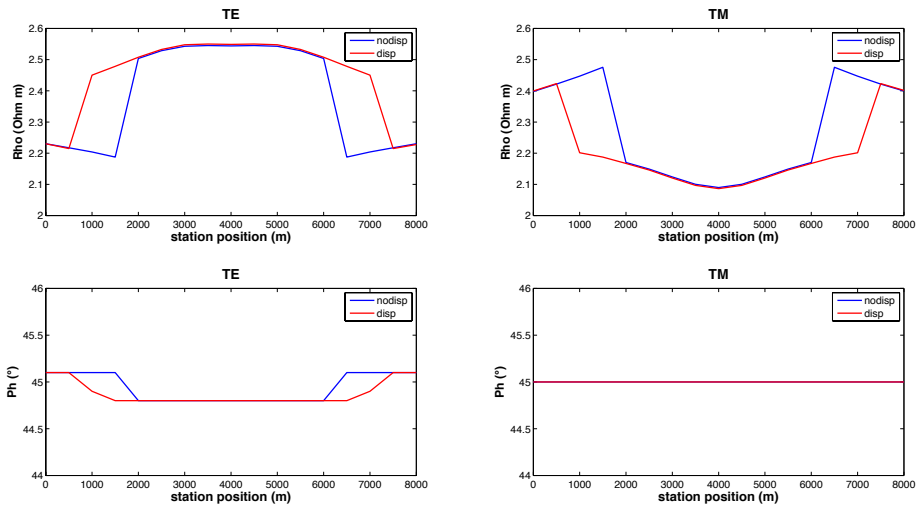

At last, along the profile 3, the effect of dispersion as seen along the profiles 1 and 2, *i.e.* the increasing amplitude of the minima and maxima along the dispersive red curves, almost completely disappears. The different width of the anomaly centered above the prism becomes, instead, the dominant character, especially for the curves of the modulus. The red central anomalies at 1 Hz are less wide than the corresponding blue anomalies, then, from 0.1 Hz down to 0.001 Hz, the red anomalies gradually become wider than the blue ones.

Of course, the amount of distortion of the MT response over a polarizable body depends on the values assigned to the Cole-Cole parameters, m, τ and c. Values of m in the range 0.4 to 0.9, of τ in the range 10^{-3} s to 10^{4} s, and of c in the range 0.1 to 0.8 are reported in literature from laboratory and field experiments made with full spectral or multifrequency IP methods (*e.g.*, Keller and Frischknecht, 1966; Sumner, 1976; Pelton *et al.*, 1978). Mauriello *et al.* (1996) gave a detailed overview on this topic, and inferred from 2D simulations that high values of m (not less than 0.75) and τ (not less than 100 s) are ideal for dispersion effects to be recognizable in MT measurements. They also showed that the TE is always the most distorted MT mode. Esposito and Patella (2009) showed that c has practically no remarkable distortion effect in MT on 1D structures. The low influence of c was also inferred by Mauriello *et al.* (1996) in 2D cases. The above effects have also been tested within the present study devoted to 3D structures. The results from a great number of simulations above the model in Fig. 23, carried out following the same approach as in Mauriello *et al.* (1996) by

changing m and τ with fixed c, fully confirm all of the above conclusions. A further consideration is that visible distortion effects can be obtained even when the m and τ vary in opposite directions. The sense is that the choice of an exceedingly low value of one of them must be compensated by a quite high value of the other one. This is just the case we have discussed a few lines above, where the value τ=10 s, well below the lower limit of the τ-range previously recalled, is compensated by the value m=0.9, at the top limit of the m-range.

3.1.1 Field example

We now show a field example already studied by Mauriello and Patella (1999) in the frame of the probability tomography imaging. The area is the eastern Snake River Plain (SRP), Idaho, where a MT profile was performed by Stanley (1982), near the Idaho National Engineering and Environmental Laboratory (Fig. 39). Fig. 40 shows the TM and TE apparent resistivity pseudosections across the SRP MT profile obtained from a computerization of the field data set of Stanley.

Figure 39: The eastern Snake River Plain with indication of the MT stations along the profile measured by Stanley (1982) and of the INEL-1 test borehole.

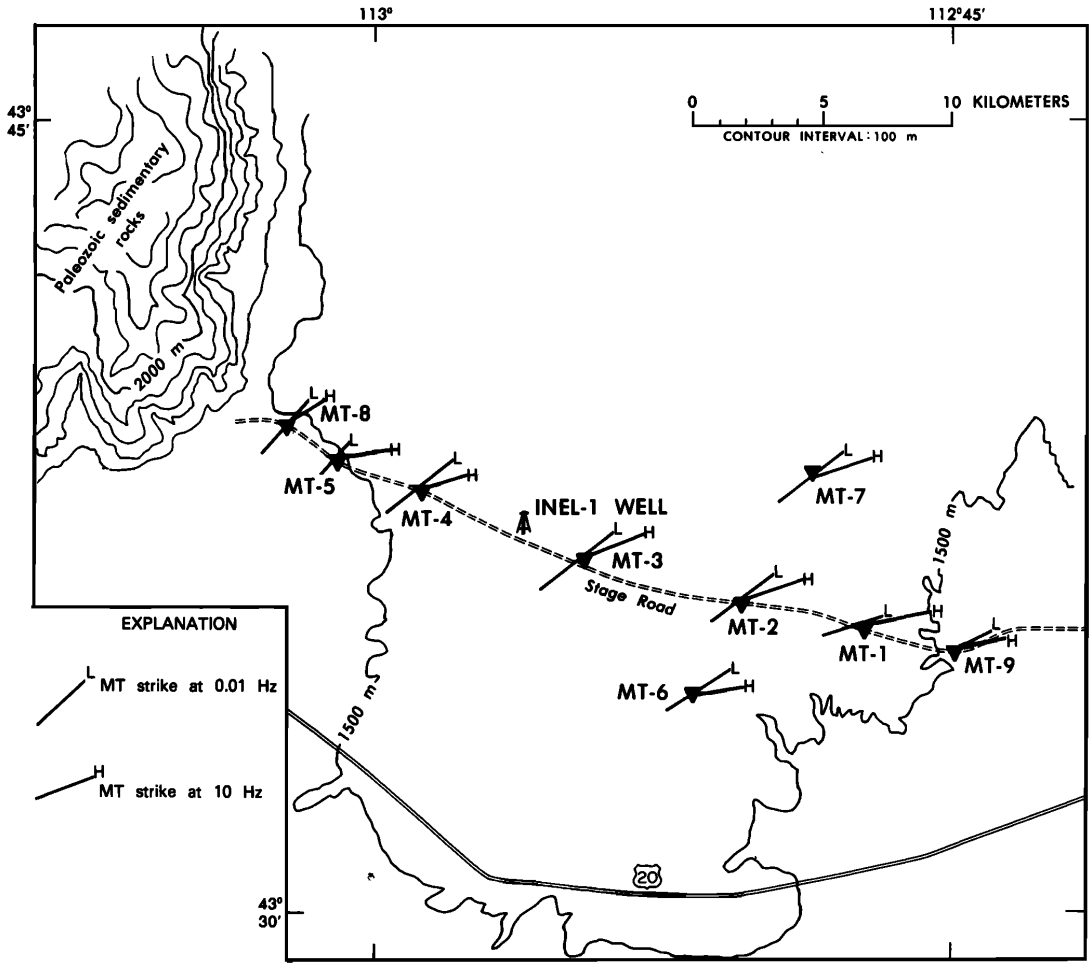

From Stanley, 1982.

The SRP is an arcuate depression bounded on both sides by the Basin and Range structures, and for much of its extent it is underlain by basalt and interbedded continental Quaternary and Tertiary sediments (Mabey, 1982). Mauriello and Patella (1999) applied the 2D probability tomography imaging to the SRP TM and TE pseudosections in Fig.40 and evinced within the SRP depression a laterally bounded conductive slab with lateral extension of about 17 km and a mean depth to its top of about 2 km.

Figure 40: The Snake River Plain MT TM and TE field pseudosections. The color scale is in Ωm.

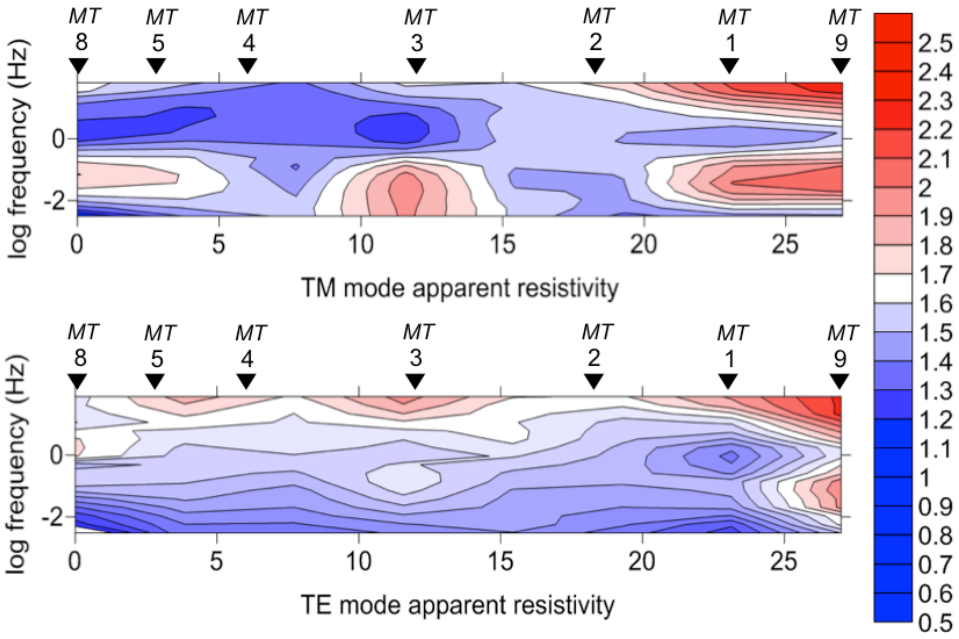

Redrawn from Stanley, 1982

In their work, dispersion effects were also admitted and using the 2D dispersive MT forward modeling by Mauriello *et al*. (1996), the 2D structure depicted in Fig. 41.a was then proposed.

Figure 41.a: The NW-SE section of the interpreted Snake River Plain structural model across the MT profile by Stanley (1982), The 3D conductive slab (15 km wide in the direction normal to the section) is assumed to be affected by resistivity frequency dispersion.

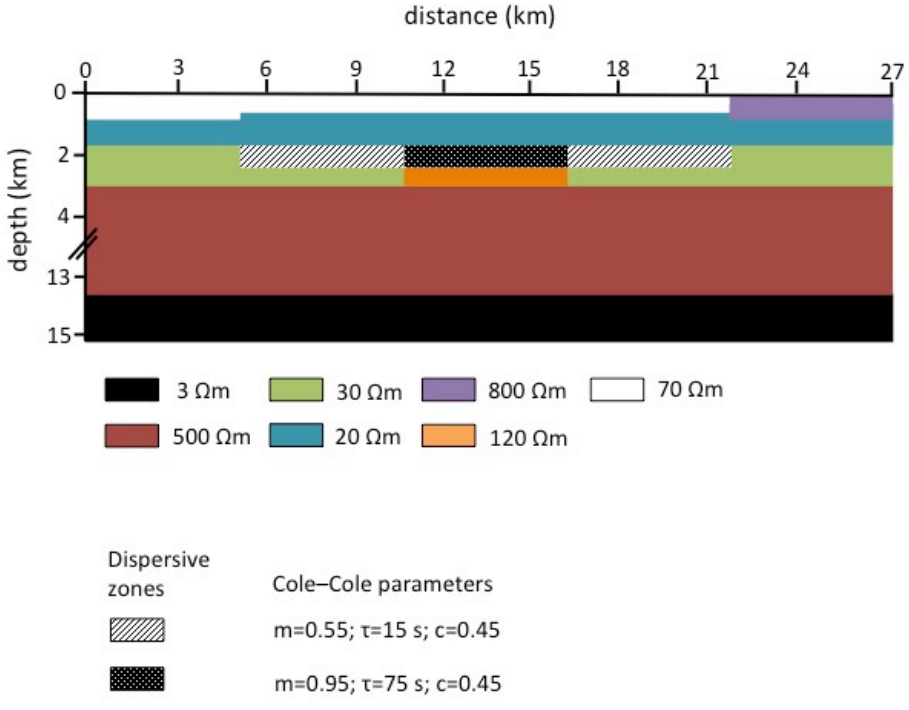

Comparing the synthetic TM and TE pseudosections from the 2D model in Fig. 41.a with the original ones in Fig.40, Mauriello and Patella (1999) found a good matching of the two TM pseudosections, while the TE ones were judged not properly conforming to each other. They attributed this discrepancy to the circumstance that the TE mode is much more affected than the TM mode whenever a 2D geometry is assumed to approximate a limited strike length slab (Wannamaker *et al*., 1984,1997; Livelybrooks *et al*., 1996).

Because of the advanced nowadays 3-D forward modeling we decide to propose a 3-D refinement (Fig 41.b) of the 2-D section in Fig. 41.a, using the same resistivity sequence and Cole-Cole parameters and assigning after trial-and-error a final strike length of 15 km to the horizontal slab (y direction), shorter than the width of the infinite length slab in the original 2-D model.

Figure 41.b: The 3-D model of Snake River Plain. Conductive slab (15 km wide in the direction normal to the section) is assumed to be affected by resistivity frequency dispersion.

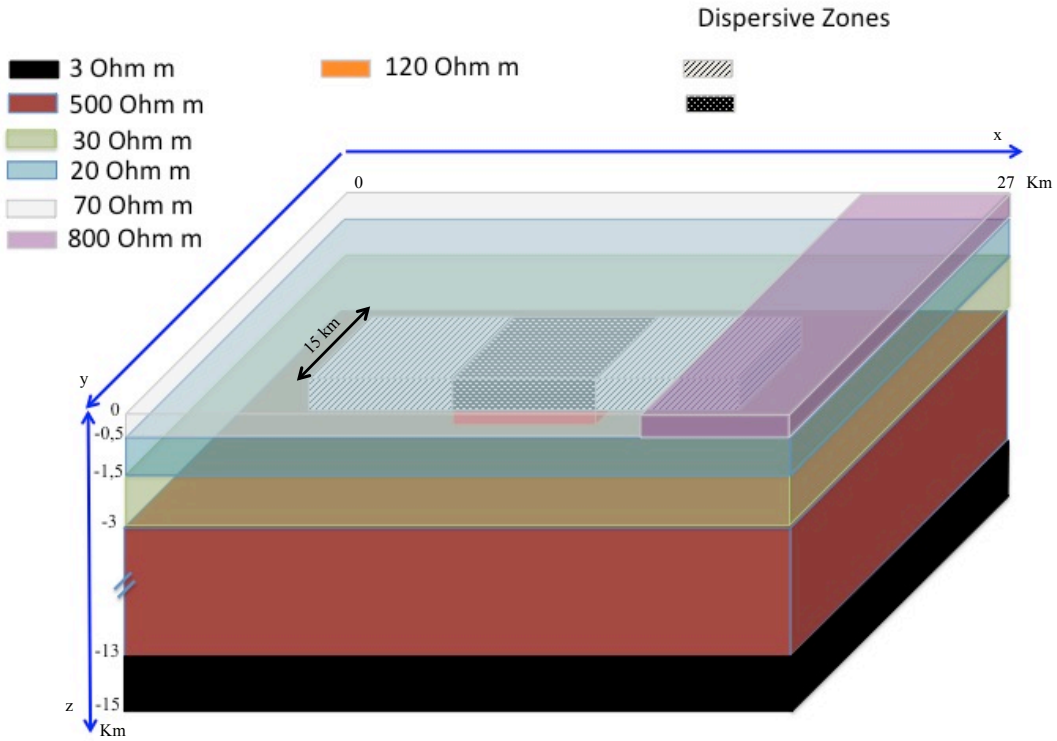

Fig. 42 shows the TM and TE synthetic apparent resistivity pseudosections, derived from the new 3D model. Finally, Fig.43 shows the misfit between the field and synthetic pseudosections, which has been plotted by assigning at each point of the pseudosections the modulus of the discrepancy index r_i, given by (Troiano *et al.*, 2014)

$$r_i=|(d_i-m_i)/\varepsilon_i|, \tag{2.40}$$

where d_i are the observed data, m_i are model responses and $\sum_i$ are the data errors with $i=1,2,\cdots,M$, M being the total number of measured data.

The normalized root mean square (*rms*) misfit has been calculated using the formula (Gabàs and Marcuello, 2003)

$$rms=\sqrt{(\sum_M r_i^2/M)}. \tag{2.41}$$

Average *rms* values have been obtained equal to 2.6 for the TM section and 3.1 for the TE section.

Figure 42: The Snake River Plain MT TM and TE synthetic pseudosections from the 3D model in Fig. 41.b. Color scale is in Ωm.

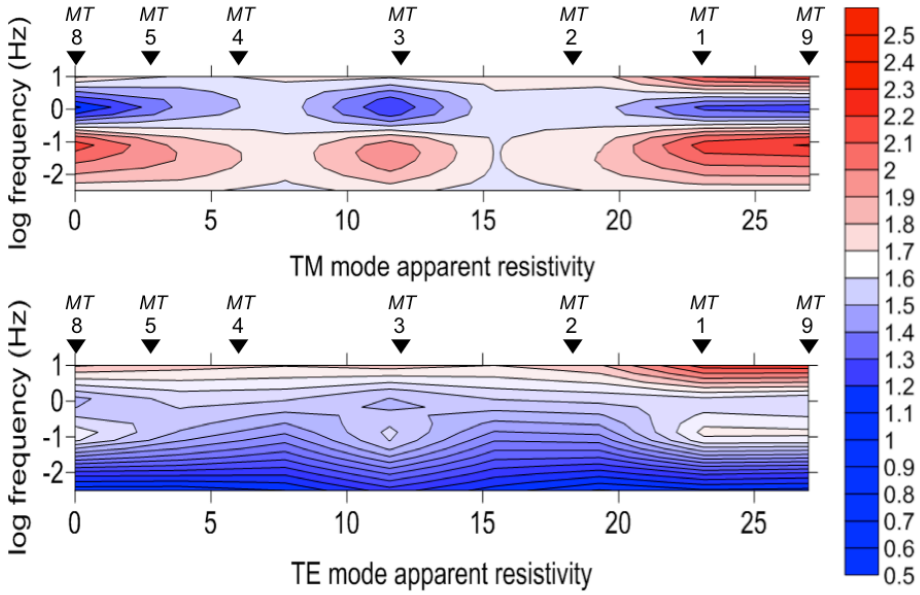

Figure 43: Misfit between the observed MT TM and TE pseudosections drawn in Fig.40 and the synthetic ones drawn in Fig.42.

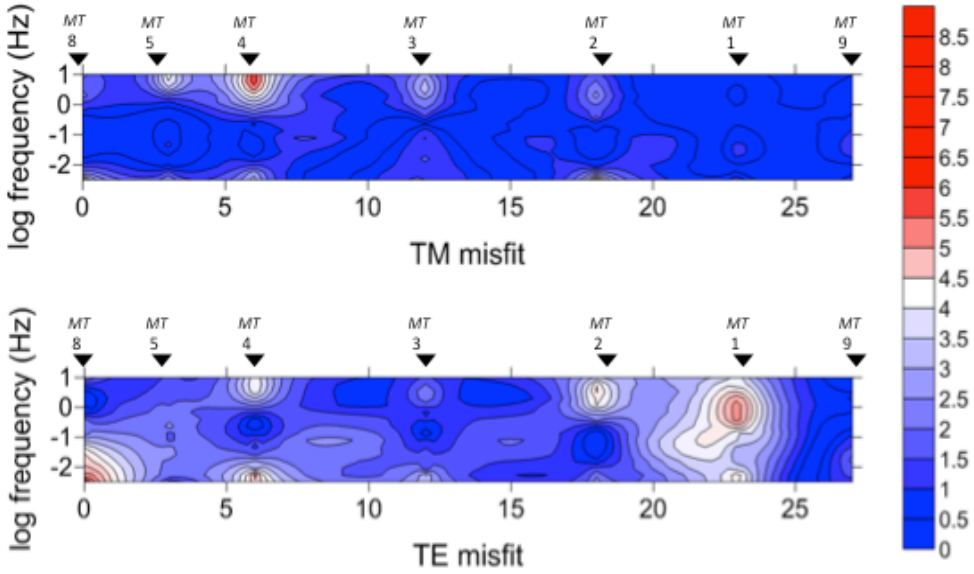

Following a previously suggested interpretation paradigm (Mauriello *et al*., 1996, 2004), *m* and τ seem to play an important role mostly in the evaluation of IP effects in volcano-geothermal areas. In fact, *m* can be associated to the degree of alteration and mineral particle deposition due to rock-fluid interaction. Within certain limits, the higher is the volume percent of alteration products occluding rock fissures and pores, the higher is *m*. For the examined SRP field case, high *m* values, up to 0.95, have been required to model the MT profile, fully consistent with values found in other volcanic and geothermal environments (Patella *et al*., 1991; Coppola *et al*., 1993; Giammetti *et al*., 1996; Di Maio *et al*., 2000; Mauriello *et al*., 2000, 2004).

The parameter τ, instead, seems governed by the local temperature, versus which it has a rather complex direct proportionality, like in the empirical diagram shown in Fig.44, which was derived from the analysis of other partially or totally controlled volcano-geothermal conditions (Mauriello *et al*., 2004). Therefore, the values of τ reported in Fig. 41.a should indicate temperatures between 70°C and 125°C in the central part of the slab and between 50°C and 90°C in the side parts, in the depth range 1.5-2,5 km below the SRP depression. These indirect temperature estimates are in full agreement with data from the INEL-1 test hole (Mann, 1986).

Figure 44: Temperature versus Cole-Cole time constant empirical diagram in different areas of the Earth.

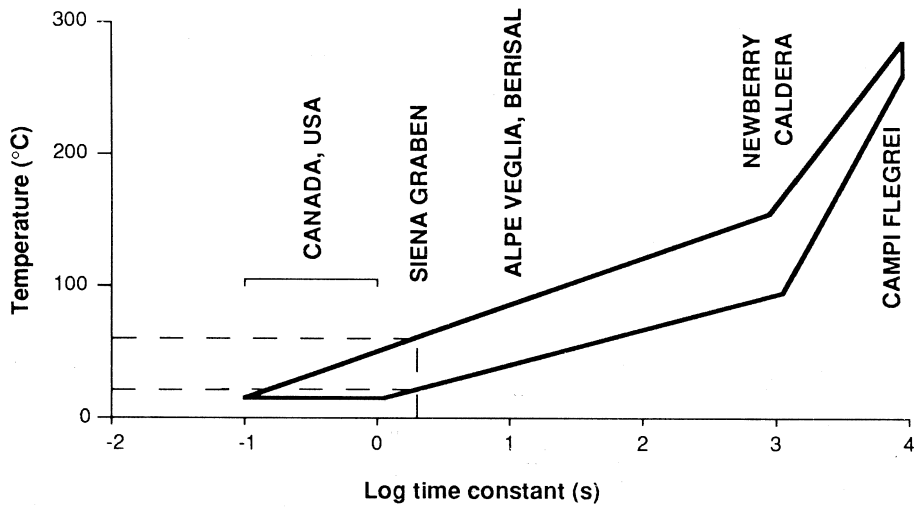

From Giammetti et al., 1996.

4 MT METHOD AND RESULTS

Now we disregard the dispersion of the resistivity to dedicate our attention to the application, both practical and theoretical, of the magnetotelluric method in two different geological environments, the Pecém region (Ceará) and the Potiguar Basin (Rio Grande do Norte). The ideal approach to evaluate the possible dispersion of the resistivity in the Pecém region is to perform a geoelectrical measurement campaign in order to obtain calculated MT curve that we can compare with the measured ones. In the case of Potiguar Basin we know that we are dealing with the presence of hydrocarbon reservoir so we can suspect that the dispersion of the resistivity may affect the MT data. In this case we have decided to study the resistivity dispersion in a future work, when an MT field campaign will be performed in the area, preferably a CSAMT campaign (Controlled Source Audio-Magnetotellurics) so as to have a better resolution in the first kilometer, and we can compare the measured data with the synthetic dispersive ones.

For now we have concentrated our attention to the use of the classical MT method in these two environments.

4.1 Data acquisition

To perform MT and CSAMT data acquisition we arrange over the surface electric and magnetic sensors (Fig. 45). Magnetic sensors are positioned in the three orthogonal direction x, y, z (NS, WE, depth) are formed by a solenoid that rotate around a high magnetic permeability core material which easily retails magnetic field lines. The assembly is inserted into a tube whose extremities are electrical contacts that detect potential differences due to the passage of current in the solenoid. The electrical sensors consist of a pair of electrodes placed into the ground in order to measure the potential difference caused by the passage of electric current.

Unlike magnetic sensors, electrical sensors are positioned only in the two directions x, y; the vertical component of the electric field is not measured, being zero the electric component at the interface surface – air (Fig.46).

Figure 45: MT equipment for data acquisition. Three magnetometers (blue), electrodes (white) and ADU acquisition system (orange box).

It takes a total of five channels, three magnetic and two electric for 3-D structures; are sufficient two channels for 1-D structures, a magnetic and an electric channel arbitrarily positioned on the surface.

Figure 46: Configuration for MT data acquisition.

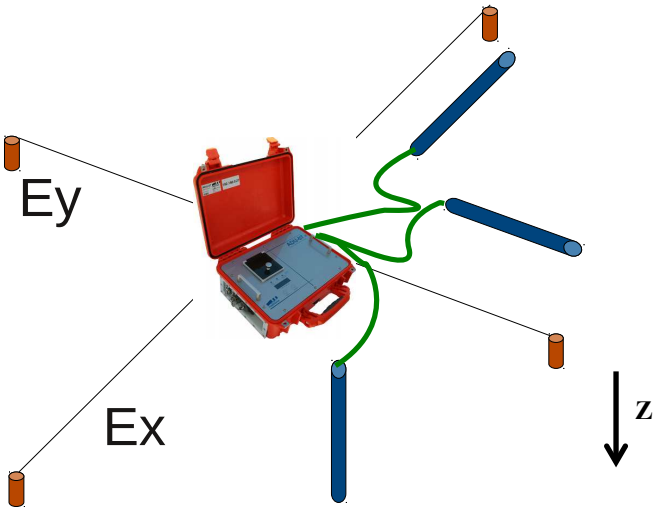

4.2 Data processing

From the data acquisition to the interpretation, intermediate steps are required: processing and inversion, as shown in the diagram below.

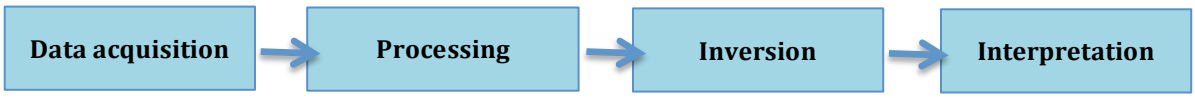

The processing is a data analysis technique whose goal is to extract from the signal, in this case time series (time variations of electrical and magnetic field), functions that are able to represent the response of the medium under examination and that can be used to interpret the conductive structure. In the MT method, these functions are the values of impedance tensor.

The purpose is to determine with greater precision possible, the surface impedance tensor that connects, for each frequency values ω, the horizontal electric field components Ex and Ey at the Hx and Hy components of the magnetic field. Fig. 47 shows a limited portion of the time series registration of the electric and magnetic field. The signals acquired can have extension of minutes or even days, months, depending on the frequency component, and consequently the depth, we are interested in.

Figure 47: MT time series.

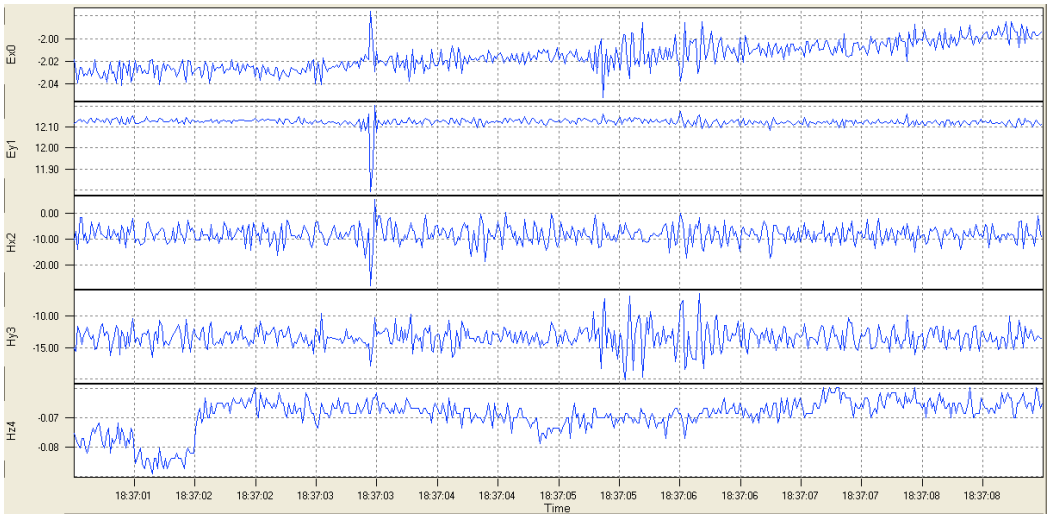

The first step is to pass from time domain to frequency domain applying a Fourier Transform to several time windows.

Impedance tensor Z does not change very quickly with frequency. For this reason the same Z can be associated to an entire frequency band. Generally in order to characterize the tendency of an impedance curve, from 6 to 10 frequency points are used per logarithmic decade.

Therefore a fixed number of frequencies are chosen and finally the impedance is estimated by least squares technique or robust techniques. Once impedance tensor is obtained apparent resistivity and phase values are calculated (Fig. 48).

Figure 48: Apparent resistivity and phase curves. Red and blue curves represents TE and TM modes respectively.

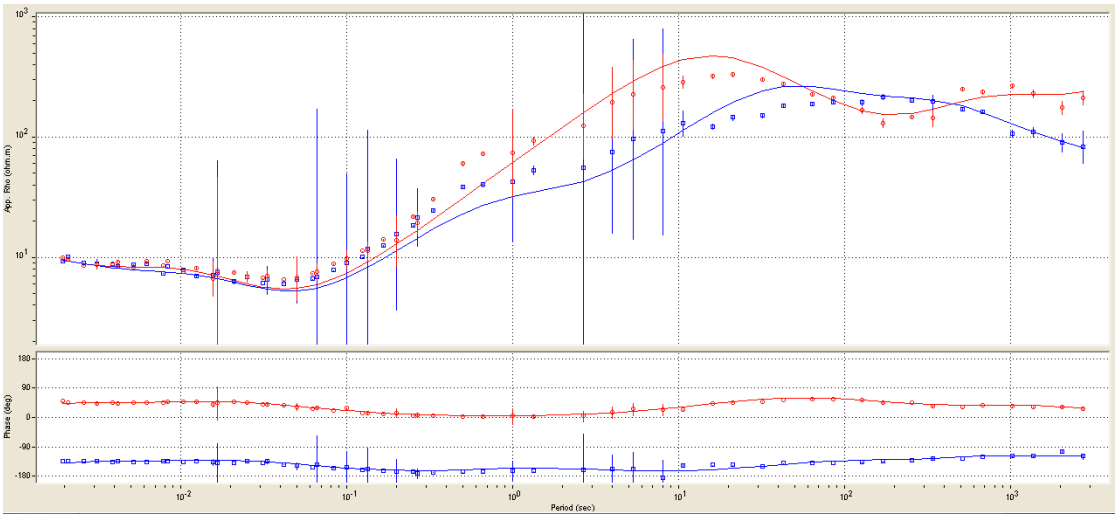

4.3 Inversion

Geophysical inversion is a mathematical process whose objective is to deduce a cause from its effect. In the case of magnetotelluric method, as in many other geophysical methods, the purpose of inversion is to reconstruct the subsurface resistivity distribution from data measured at the surface.

The first step is the creation of a direct model, in other words, basing on preliminary information of the surface and the subsurface it is calculated the synthetic response of the Earth starting from an input model.

The second step is the comparison of synthetic response data with the measured data on the surface, i.e. minimize the difference between measured and synthetic data refining the Earth model.

4.4 MT study in Pecém region – Ceará

We present a case study in an area in the Northeast of Brazil, precisely in the west coast of the State of Ceará. Pecém is approximately 80 km from the city of Fortaleza.

Data acquisition was performed with the Geophysical Laboratory of UFC using Metronix ADU-06 instrumentation and along a profile parallel to the coastal line were performed 5 points of measurements.

In the figure 49 we can see the position of the MT station and synthetized geology of the Pecém region.

Figure 49: Synthesized geology of Pecém Region, NW Fortaleza City with the position of the five MT stations

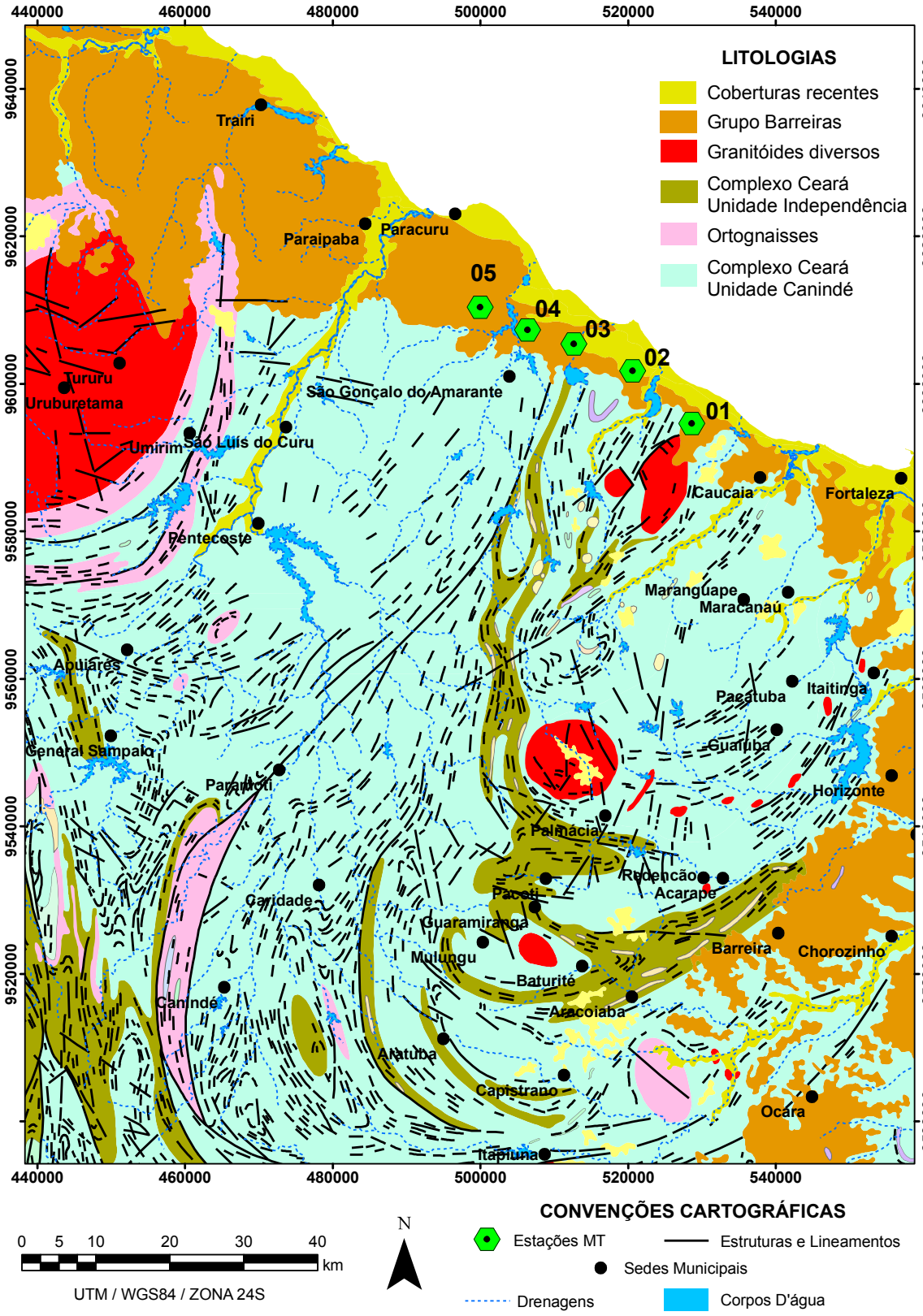

from CPRM, 2003.

The study area is a transition zone between a Pre-Cambrian (Gneiss-migmatitic Complex) unit and Tertiarius-Quaternary units formed by sedimentary deposits of the Group "Barreiras" (eluvial-coluvial coverage) and the Quaternary units (aeolian, marine and fluvial deposits. As it can be seen in Figure 49 the geology of the region is composed by recent sedimentary lithologies, lithologies of the Group "Barreiras" and rocks of Ceará Complex; in the East portion several granitic rocks are present in the form of granite massifs of high morphological features. Several structural trends are oriented in directions North and North-NorthEast. It is important to note that the lithologies associated with the Ceará Complex - Independência Unit are markedly limited and oriented North - NorthEast, inserted in the Caninde Unit.

4.4.1 Processing, inversion and interpretation of MT data

Data were processed and inverted 2D using the software Winglink 2.01.01. In figure 50 it is shown the calculated apparent resistivity model. This is the result of the inversion smoothed through the Rodi and Mackie algorithm (Rodi and Mackie, 2001) that calculates the minimum distribution of resistivity that fits the data at each station. The direct model is calculated using finite difference equations analogous to Maxwell's equations.

Figure 50: Calculated resistivity model. Station MT5 is in the direction NW and station MT1 in the direction SE.

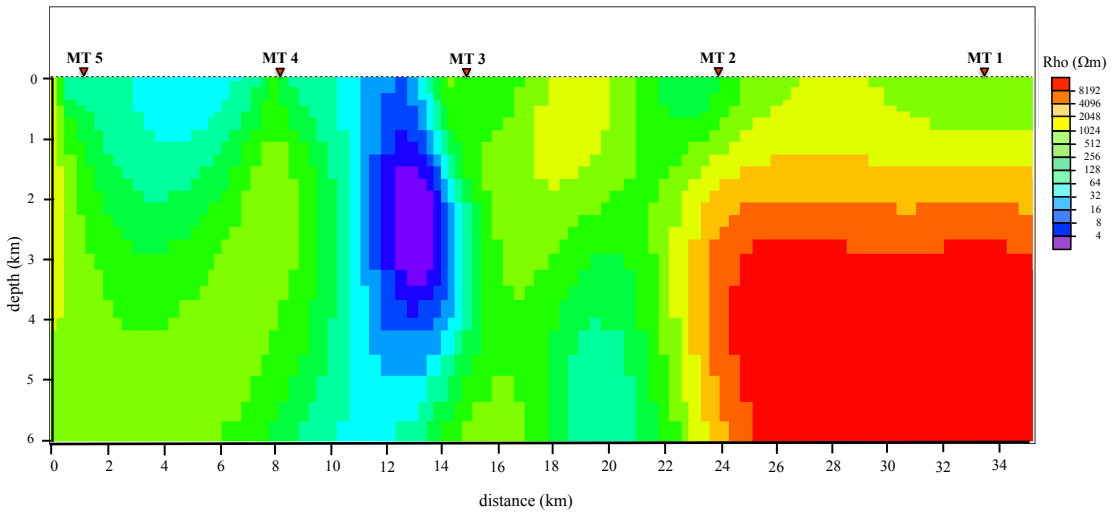

Observing Figure 50 we can recognize several geoelectric units with resistivity contrast varying both vertically and horizontally, from a value of 4 Ωm to a value of 8000 Ωm, as it can be seen in the color legend. Figure 51 we separate these areas for better viewing and interpretation.

Figure 51: Geophysical interpretation based on resistivity contrasts and correspondences with geotectonic units (crustal blocks). Station MT5 is in the direction NW and station MT1 in the direction SE.

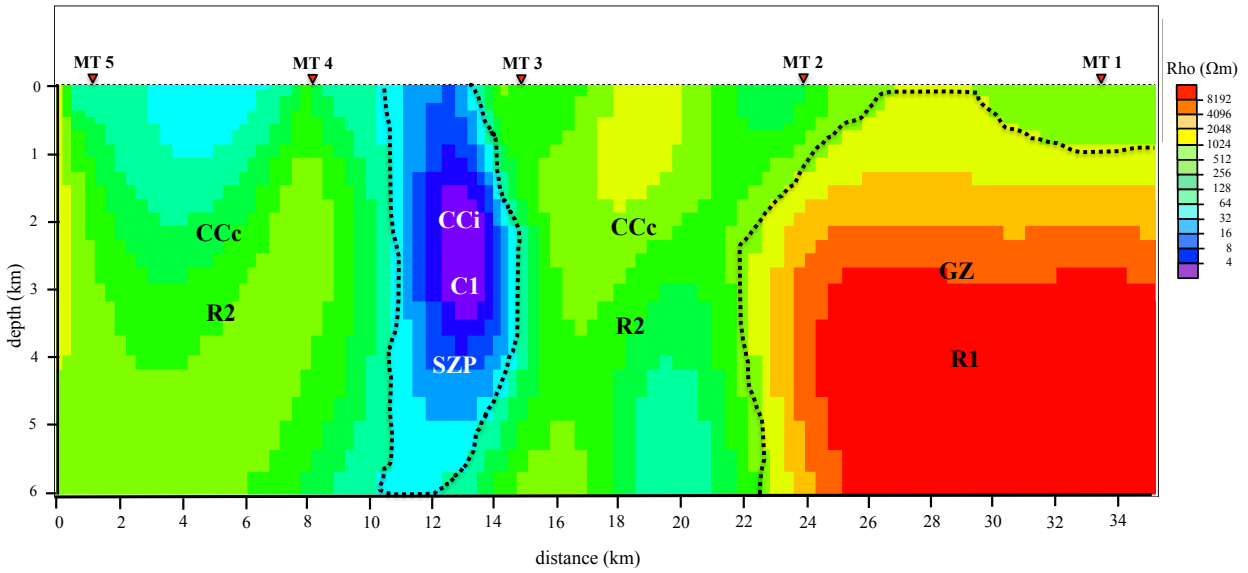

SZP Shear Zone *Paramonti*
R1 > R2 > C1 Resistive and conductive zones
GZ Granitic Zone
CCc Ceará Complex *Canindè* Unit
CCi Ceará Complex *Indipendencia* Unit
Crustal Blocks Limits

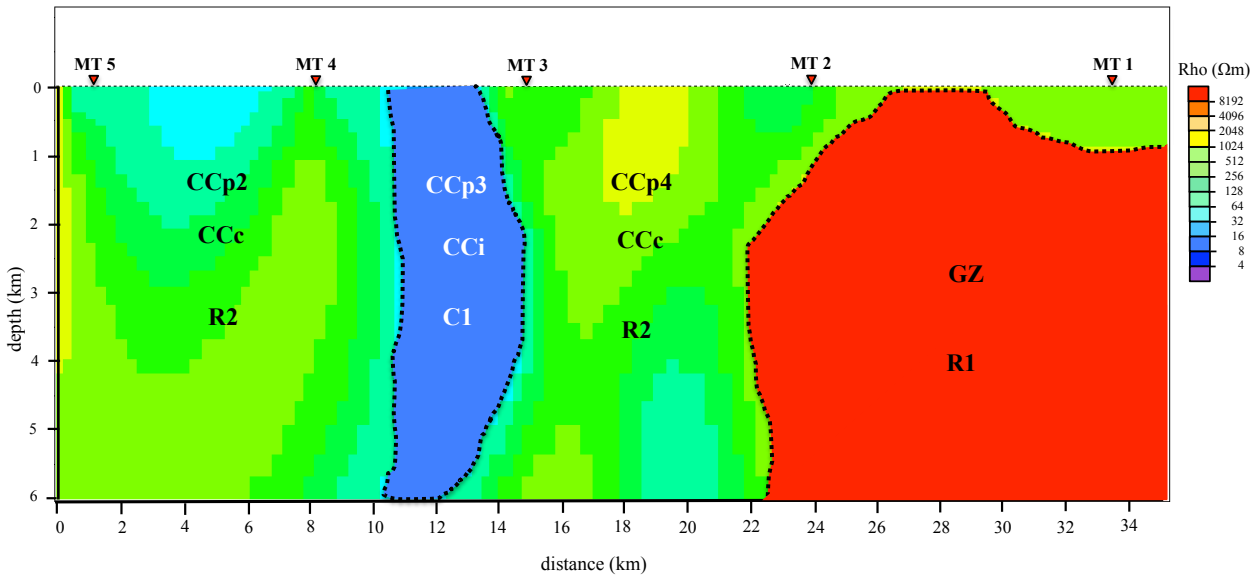

We can recognize four geoelectrical zones:

- One conductive zone C1 located between the MT stations 3 and 4 extending vertically to the base of investigation. This area can be associated, geologically, to the Shear Zone *Paramonti* described in literature (Amaral & Santos, 2008). Such interpretation is supported by rock types present in the shear zone composed by aluminous metasediments and schists.

- Two zones with resistivities R2 higher than 250 Ωm enclosing the conductive area C1. This geoelectric zone is associated with the Central Ceará Complex represented by Canindé Unit composed by paragneiss, migmatites and matabasic rocks.

- The resistive zone R1 with value of resistivity up to 8000Ωm order is located in the eastern section. This geoelectric zone is most likely a major crustal block of highly resistive nature that can be associated to the granitic massif of the *Serra do Juá* with a significant geographic and spatial distribution. It is noteworthy that the geological mapping by CPRM does not present this feature. Parallel to *Paramonti* shear zone and at a depth of around 6000 meters another resistive block can be distinguished, and associated with the *Serra do Juá* mentioned earlier.

We tried to make a comparison with the geological data presented by Amaral & Santos (2008) that consider supracrustal units as River Curu Unit (CCP2) which would correspond to Caninde Unit of CPRM (2003) and the internal rocks as the shear zone Paramonti (Paramonti Sequence Amaral & Santos, 2008 - CCP3; Independência Unit of CPRM, 2003). The latter composed by aluminium metassediments, mylonite and granulites rocks possibly presents the conductive characteristic denoted from the result of the inversion.

The unit with biotite gneisses locally migmatized and with granodiorites (Ccp4) of Amaral & Santos (2008) presents the same resistivity contrasts.

Finally, it is shown in Figure 52 a new geological context obtained from the MT profile and from the interpretations raised from data inversion and considering a number of new geological field observations.

The resistive zone, that in the calculated model (Fig. 50) we called R1, is easily associated with the granitic massif emerging in the CPRM map near the station MT1. The granite rock is characterized by high resistivity values; therefore we can consider the structure underneath as a continuation of itself. The conductive area is correlated to the Paramonti subduction zone, which exhibits low resistivity values due to the presence of fluids typical of the fault zones.

Figure 52: Geological context realized with MT data of this study and other geological field observations.

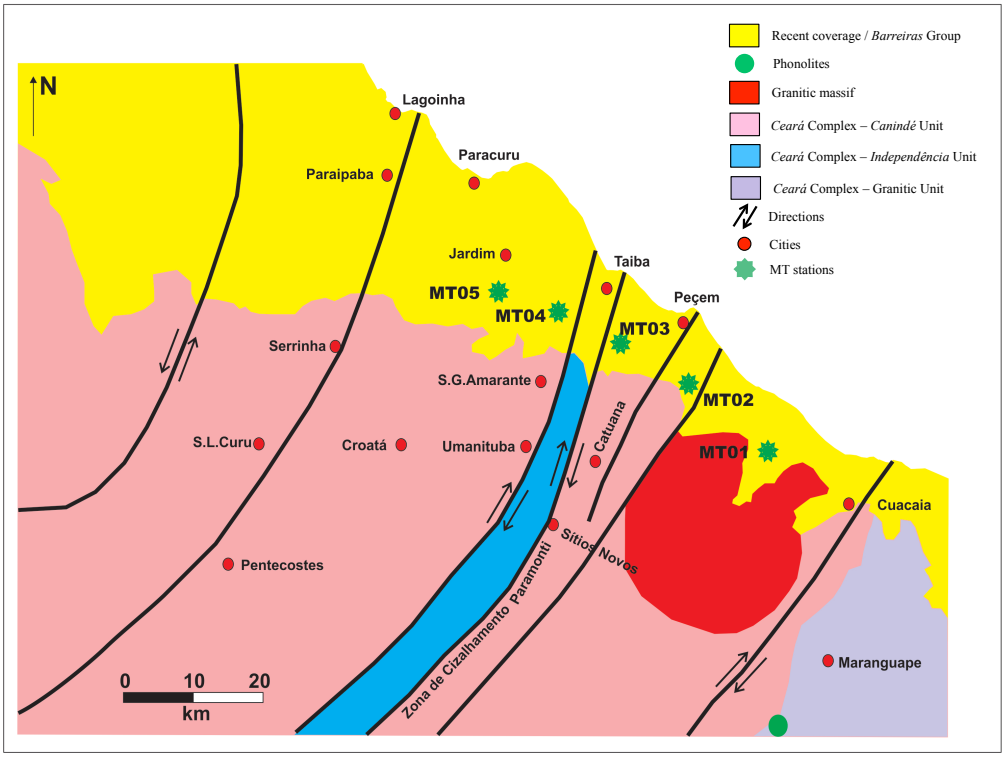

4.5 Potiguar Basin

Potiguar Basin (Bacia) has an extension of approximately 119.300 km^2 and is localized between the states of Rio Grande do Norte and Ceará, in the northeast of Brazil. The emerged portion has an extension of 33.200 km^2 and the remaining part of 86.100 km^2 is the submerged portion. Figure 53 shows the structural geology of the Potiguar Basin.

Figure 53: The Structural Geology of Potiguar Basin. Brown is the crystalline basement; blue squares represent the areas of petroleum field; is possible to see several graben and horts, platforms and faults. Red lines represents the faults in the area.

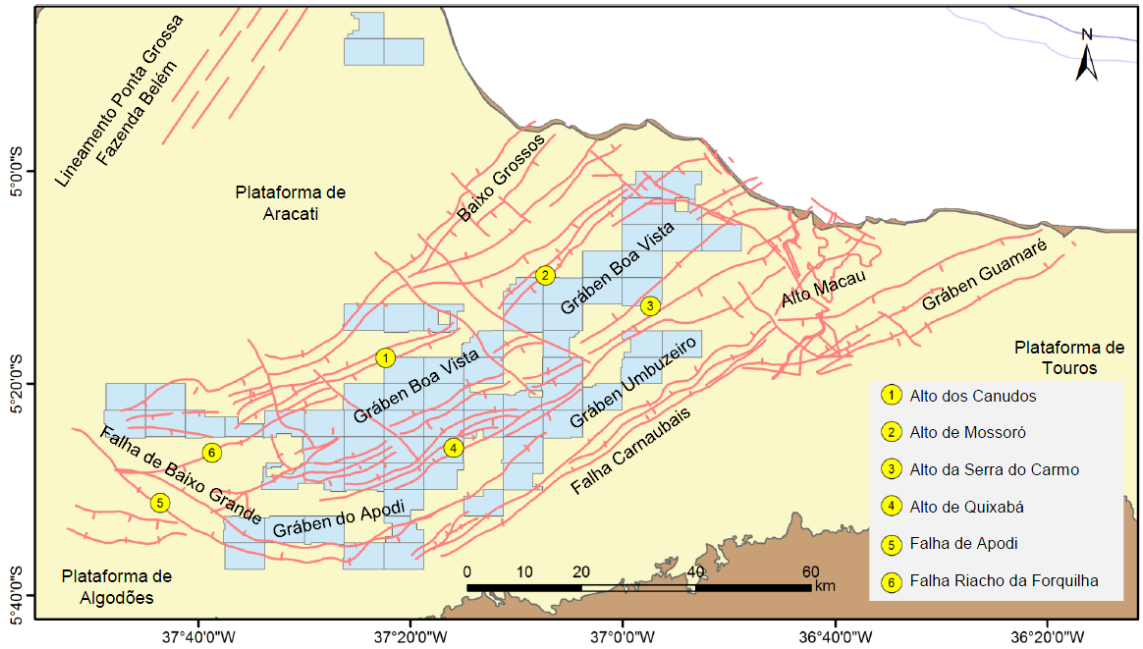

from Angelin et al., 2006, Hoerlle et al., 2007.

The Potiguar Basin is inserted in the northern portion of the Borborema Province, it belongs to the Precambrian geological segment, formed during Pan-African/Brasiliano (Neoproterozoic) Orogeny and is characterized by a complex arrangement of tectono-stratigraphic domains, bounded by zones regional shear and intense granitic magmatism (Almeida et al, 1977; Fetter et al., 2003).

The Potiguar Basin is related to a series of intra-continental basins that compose the Rift System in Northeast Brazil (Matos, 1987). There are several models in literature that attempt to explain the process of formation of the Potiguar basin.

For example Françolin & Szatmari (1987) suggest that the origin of the Potiguar Basin is related to the evolution of the Atlantic Equatorial Margin started at the end of the Jurassic.

The clockwise rotation between Africa and South America generated stresses in the Borborema Province with a resultant East-West compression and Northeast relaxation.

In Figure 54 we can see the stratigraphy of Potiguar Basin with the principal petroliferous systems (Pessoa Neto *et al.*, 2007).

Figure 54: Cretaceous Geology of Potiguar Basin and the principal petroliferous systems.

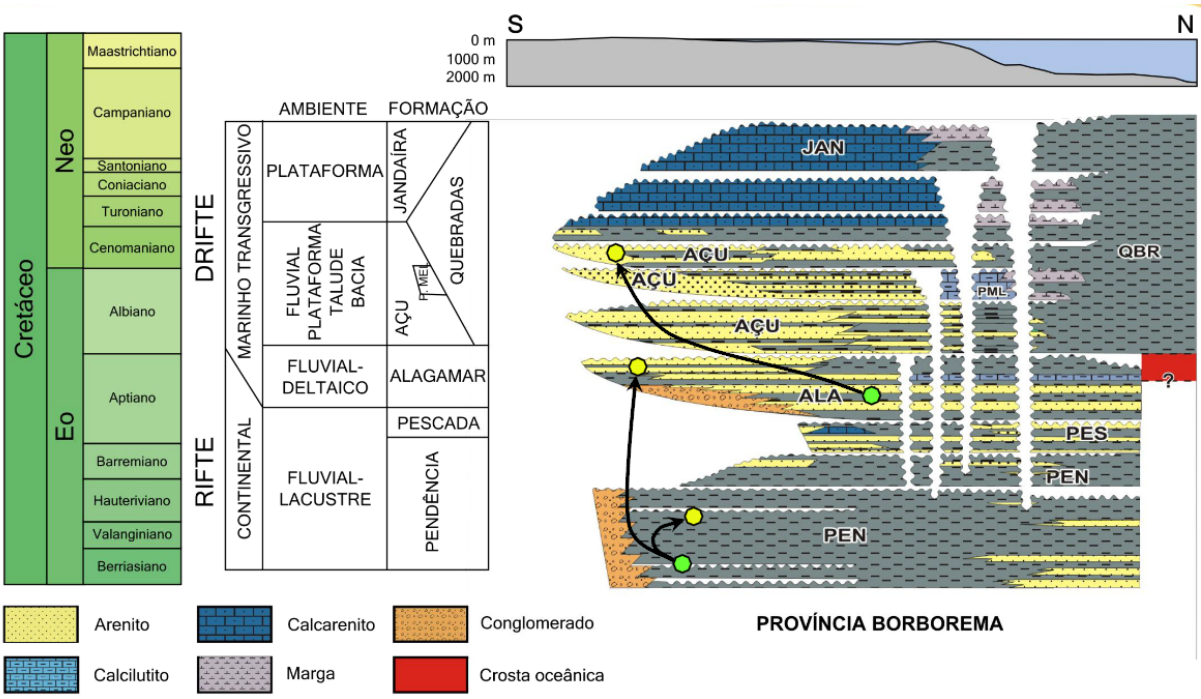

from Pessoa Neto et al., 2007.

4.5.1 Modelling and simulations in Potiguar Basin

We present theoretical MT simulations in order to calculate the MT response in presence of hydrocarbon reservoirs. The synthetic responses are performed over a 3-D model of the Potiguar Basin, which structure has been obtained from the studies of Bertani *et al.*, 1990.

Simulations, as in the previous cases, are performed using the software WINGLING 2.01.01. In Figure 55 is shown a geological cross-section of the basin and in Table 1 the corresponding resistivity values.

Figure 55: Schematic Geological cross-secton of Potiguar Basin near Serra do Mel region. In the figure below it is shown the position of the section over the basin. Black lines are representative of the faults.

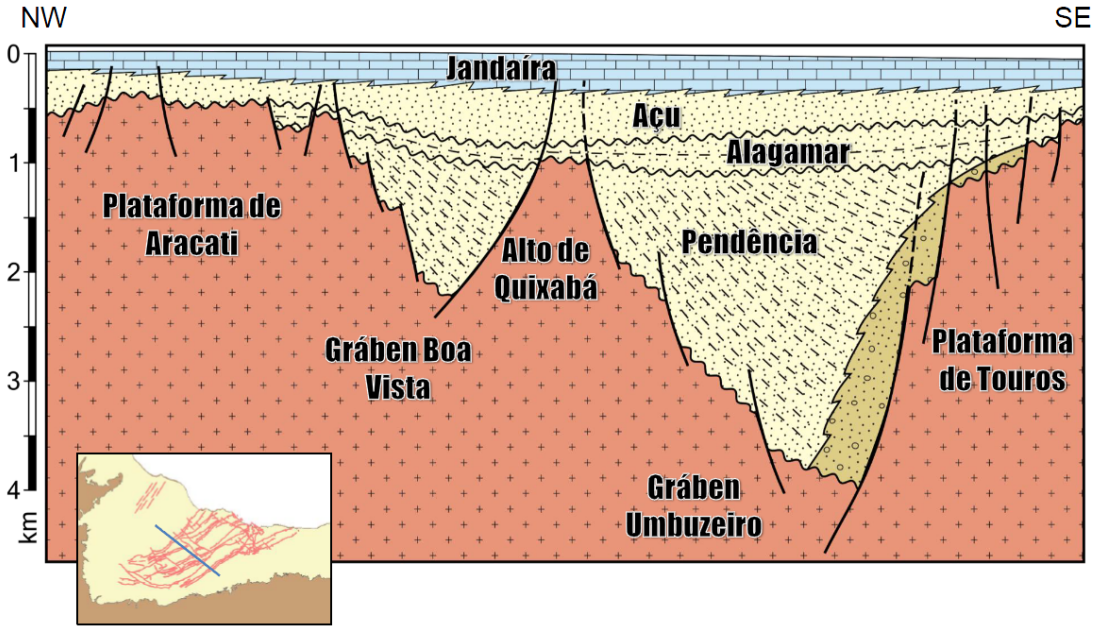

from Bertani et al., 1990.

Table 1: Values of resistivities for the geological structures in fig. 55.

Formation	Resistivity (Ohm m)
Jandaíra	180
Açu	7.5
Alagamar	50
Pendência	16
Conglomerates	100
Basement	1600

We reconstructed the cross-section showed in Figure 55 in a 3D mesh (Figure 56) positioning three areas of hydrocarbon reservoirs, H1, H2 and H3.

H1 and H2 are very shallow, positioned at a depth of respectively 200 and 300 meters, the first area H1 has dimensions 2x2x0.4km, the second area is composed by two blocks, the smaller one of dimensions 1.5x2x0.15km and the bigger 2x2x0.45km, reservoir H3 is the

biggest and the deepest, located at a depth of 1300 meters and it has the following dimensions 3.5x2x0.8km.

Figure 56: Model of Serra do Mel.

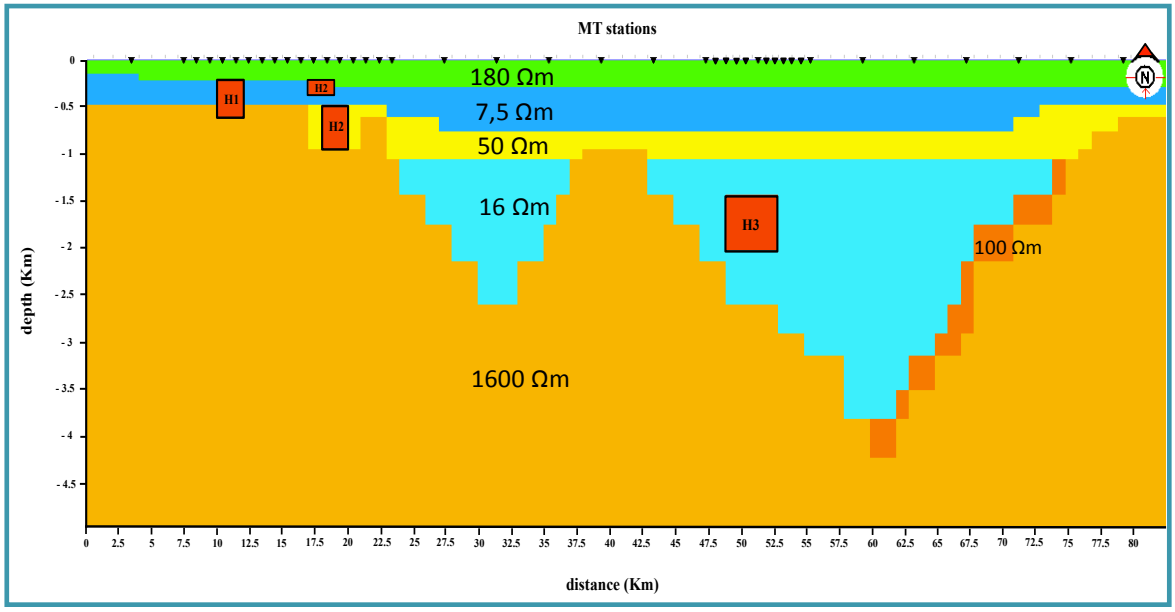

Since the profile has a big extension MT stations are differently spaced whether they are over a reservoir or far from it. In the proximity of the reservoir MT station are 100 meters spaced one from each other, then the distance between stations increases up to 4 kilometers. We focused our simulation on the areas H2 and H3 showed in the Fig. 57 and 58.

Figure 57: Model of the reservoir H2.

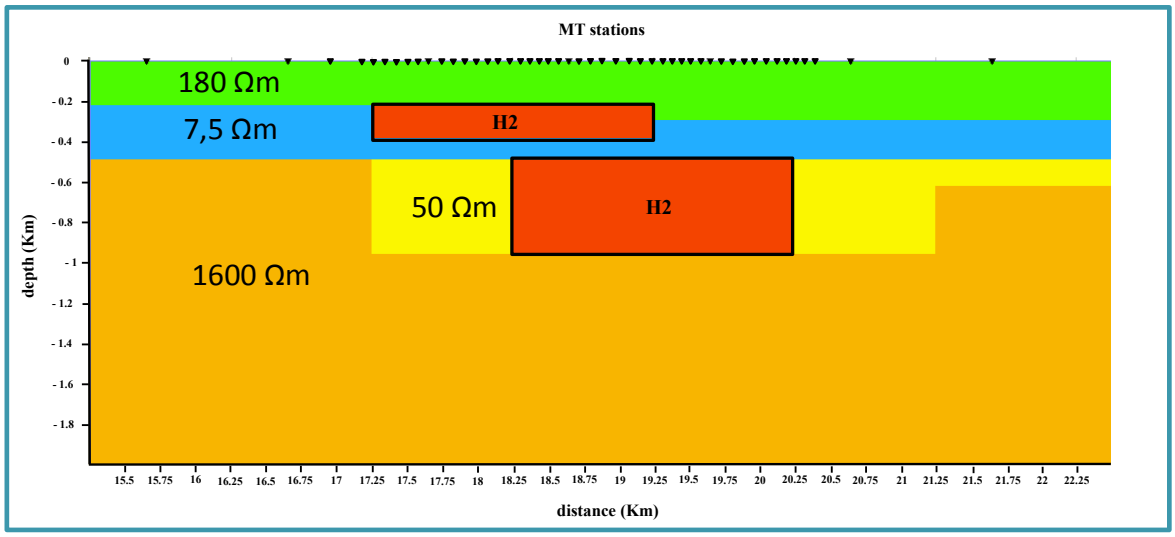

Figure 58: Model of the reservoir H3.

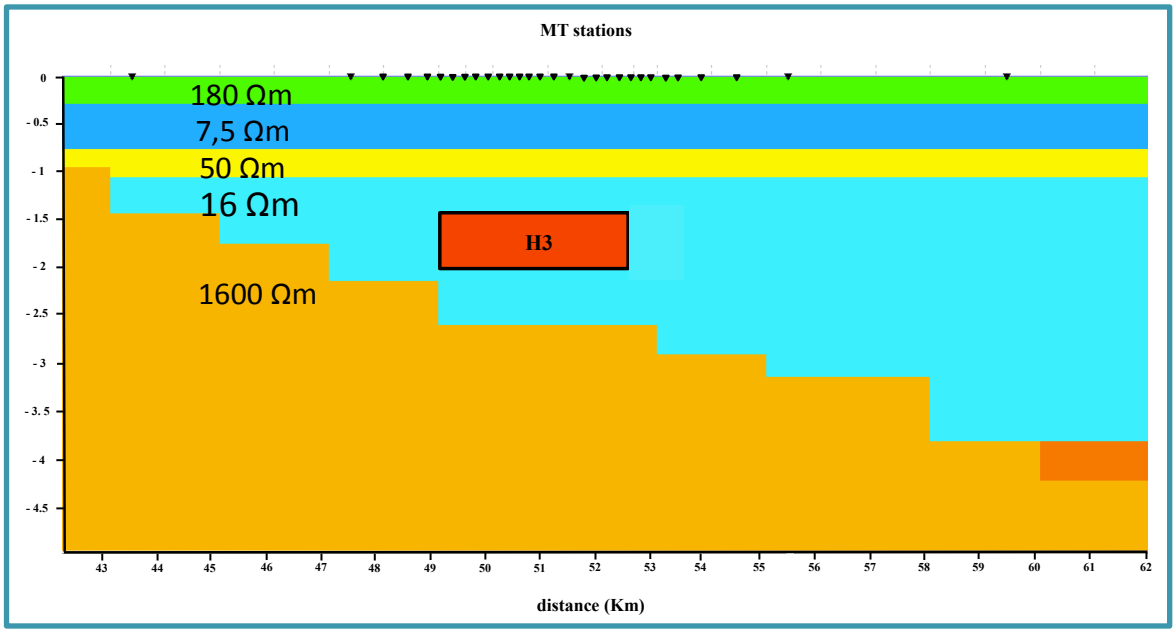

In order to show the effect of reservoirs, pseudosections are performed with and without the presence of hydrocarbon and then compared.

We decided to use two resistivity values for the hydrocarbon reservoirs to study the influence on the MT responses. The first value assumed is 750Ωm, about one order of magnitude more resistive than the surrounding host, considering that Oil, and particularly gas, increase the resistivity of the sediments (Bjorlykke, K., 2010, Petroleum Geoscience). The

other value taken into account is 5000Ωm, which is an extreme case meaning that the reservoir is fully saturated in hydrocarbon and it does not contain water.

In Figure 59 we show the TE and TM pseudosections without the presence of the reservoir, whilst Figure 60 and Figure 61 show pseudosections in presence of reservoirs. As we can see the reservoirs are detected from the MT responses, both cases, resistivity 750Ωm (1°case) and 5000Ωm (which means a reservoir completely dehydrated, 2° case) show a perturbation in the pseudosections that can be quantified with the misfit shown in Figures 62 and 63.

Figure 59: Resistivity TE and TM pseudosections without reservoirs. Color scale is logaritmic.

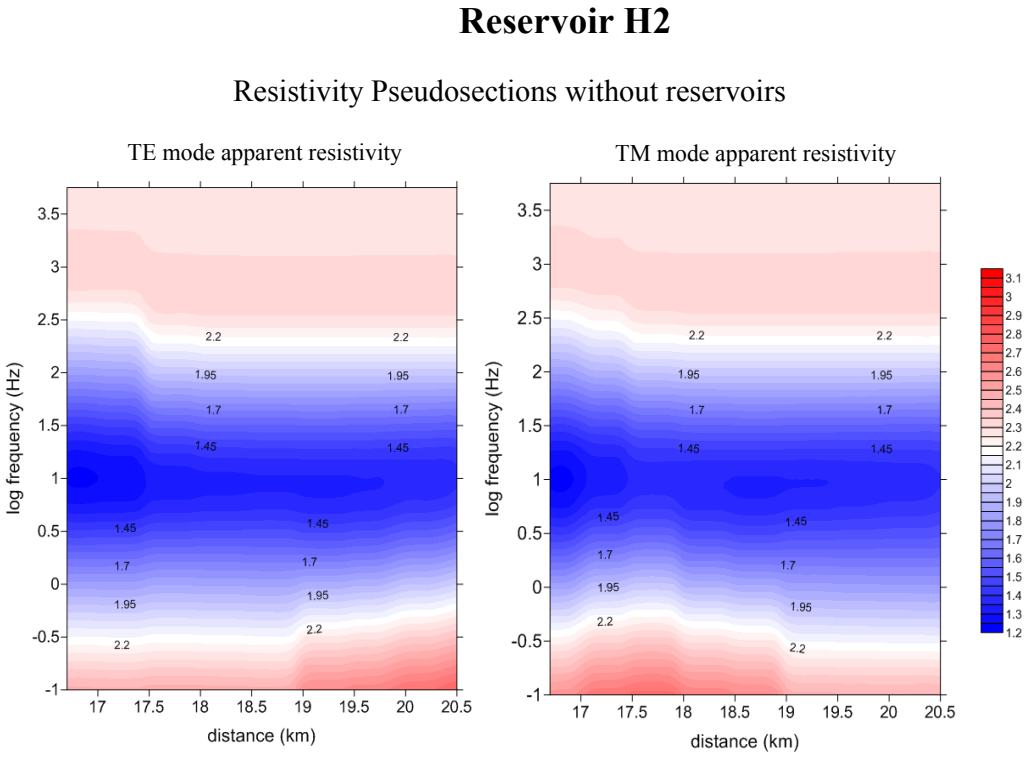

Figure 60: Resistivity TE and TM pseudosections with reservoirs case 1, resistivity value of 750Ωm. Color scale is logaritmic.

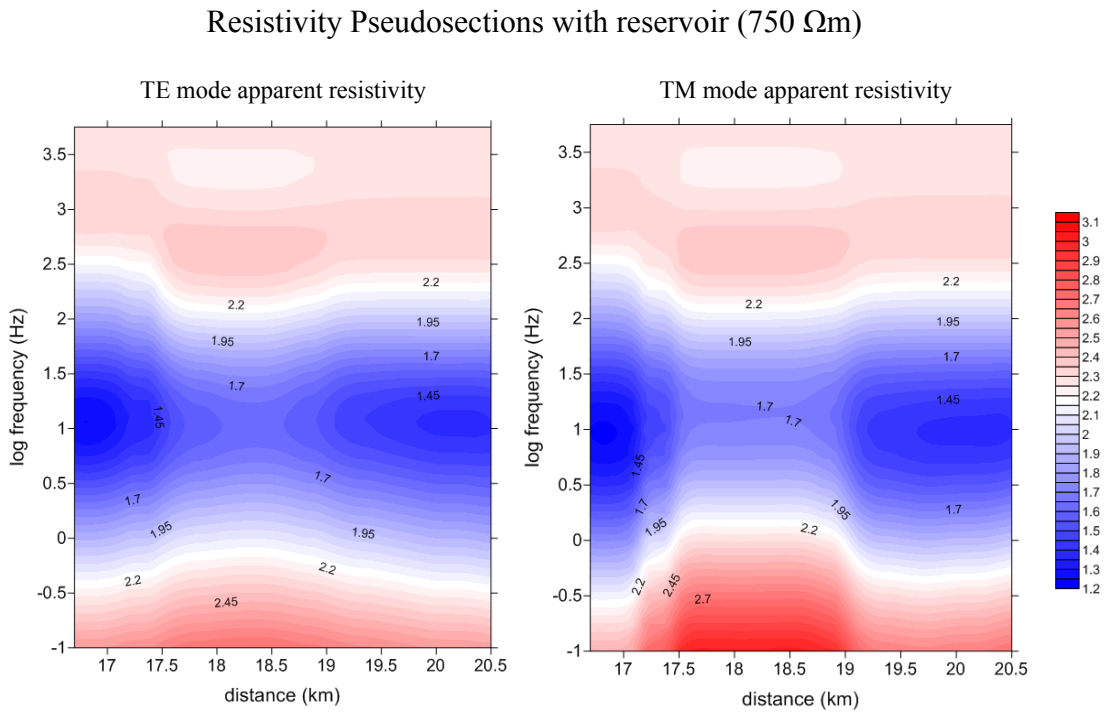

Figure 61: Resistivity TE and TM pseudosections with reservoirs case 2, resistivity value of 5000Ω. Color scale is logaritmic.

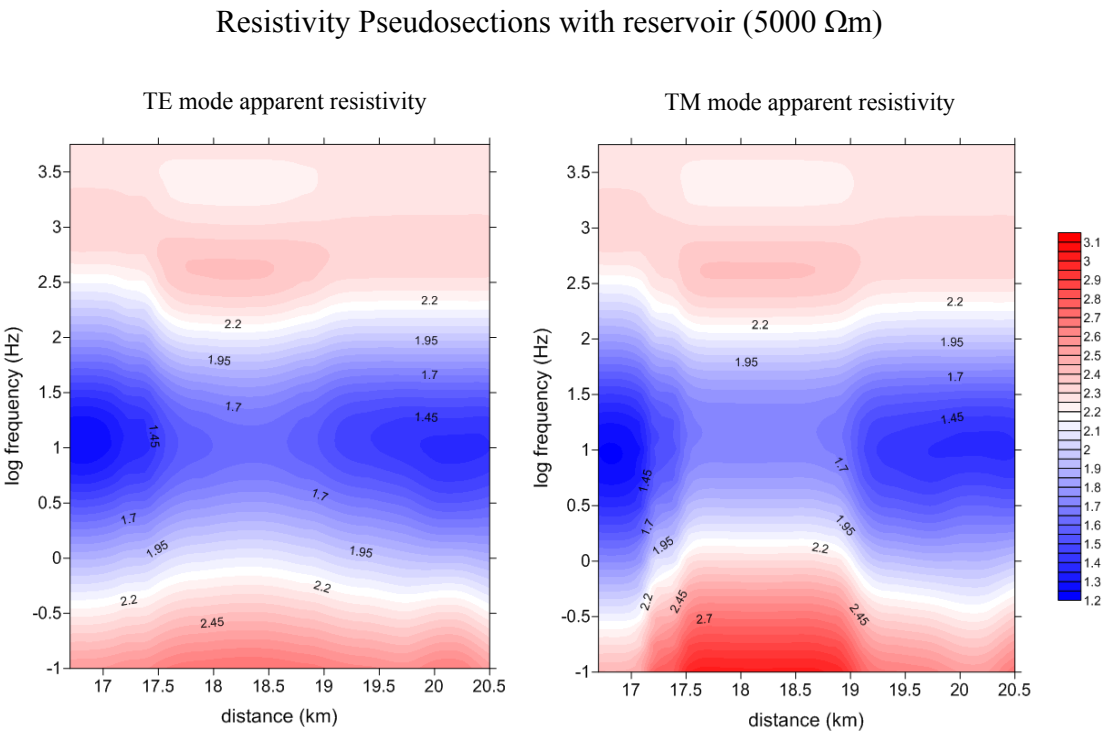

Figure 62: Misfit between pseudosections drawn in Fig. 60 and the ones in Fig. 59. Color scale is logaritmic.

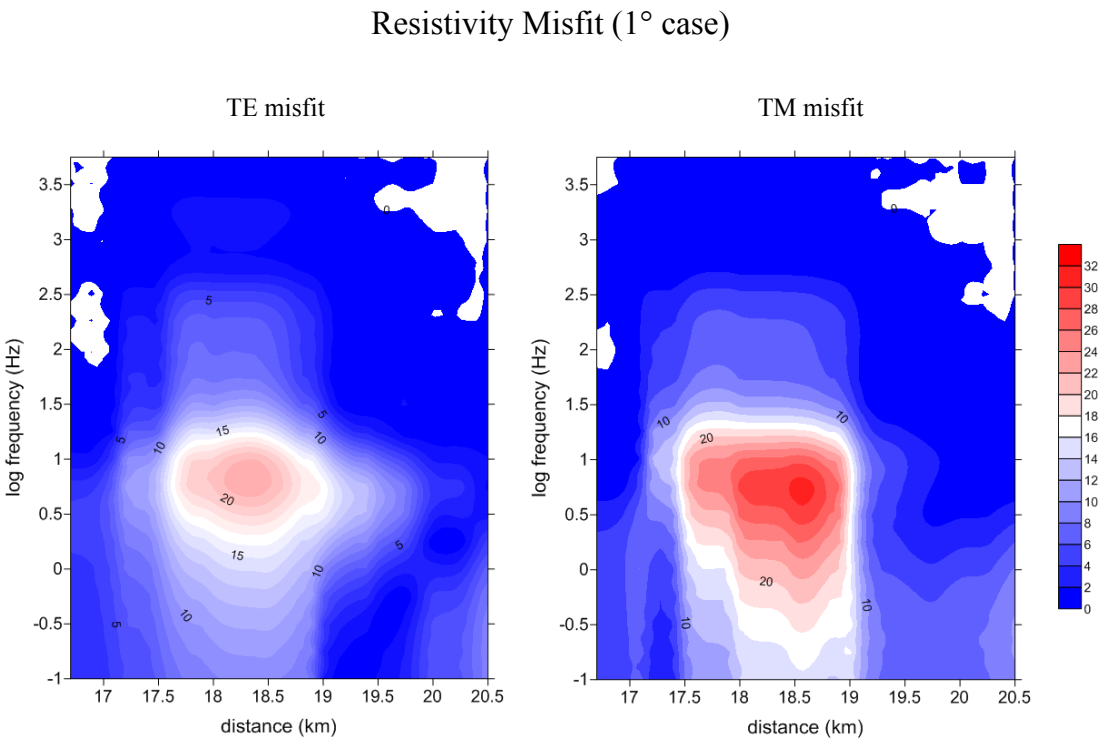

Figure 63: Misfit between pseudosections drawn in Fig. 61 and the ones in Fig. 59. Color scale is logaritmic.

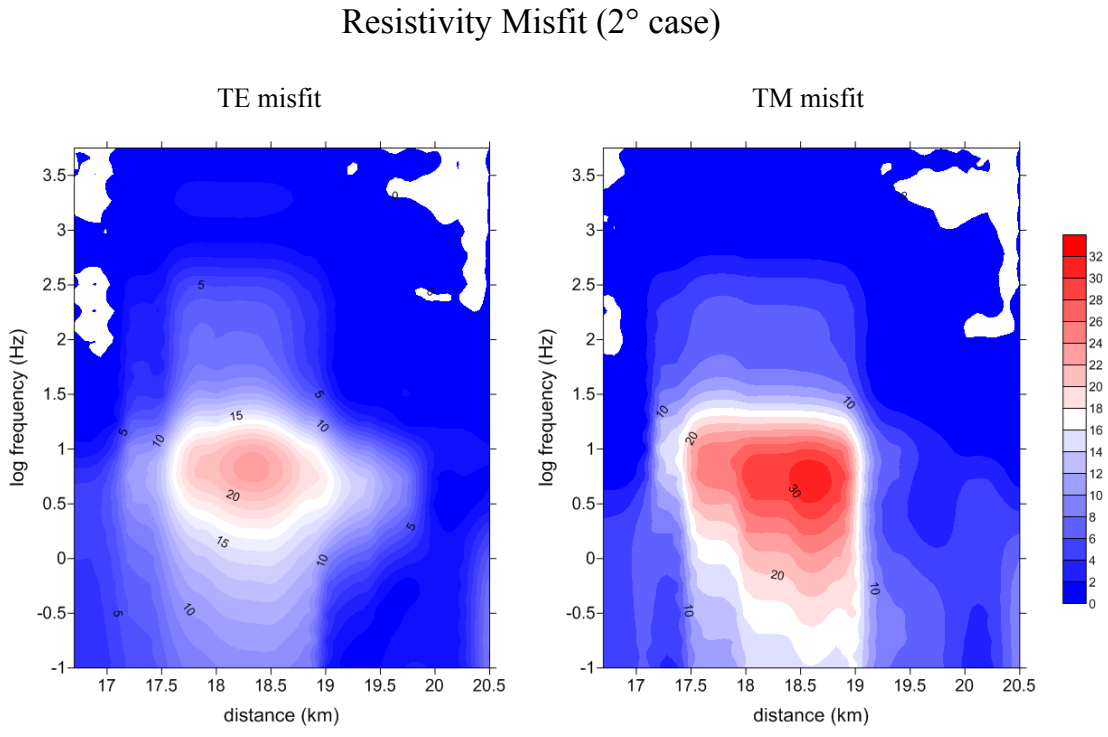

The Figs. 60 and 61 show an increase of the resistivity values exactly where the reservoir

is positioned, emulating clearly its shape. This makes the interpretation of the results quite simple and clear.

Also for the reservoir H3 two values of the resistivity have been considered, 750Ωm and 5000Ωm, but the results are not so encouraging. Looking at the Figs. 64, 65 and 66 we observe that reservoir H3, deeper than H2, is barely visible in the pseudosections (Fig. 65 and 66) and this is confirmed by the misfit, in Fig. 67, which values fall within the margin of error of 5%.

From the simulations we can assume that this is as a case limit for MT detection of reservoir in area of Serra do Mel. Through these simulations we have seen that the deeper reservoir is a threshold for this geological environment, beyond which the MT method does not provide useful information. This is a quite surprising result considering that both the resistivity value of the reservoir (5000Ωm) and its thickness in proportion to the depth are features that should highlight the presence of the reservoir. The result obtained should be verified with an MT sounding in the area to confirm that it is necessary the use of another geophysical prospecting method.

Figure 64: Resistivity TE and TM pseudosections without reservoirs. Color scale is logaritmic.

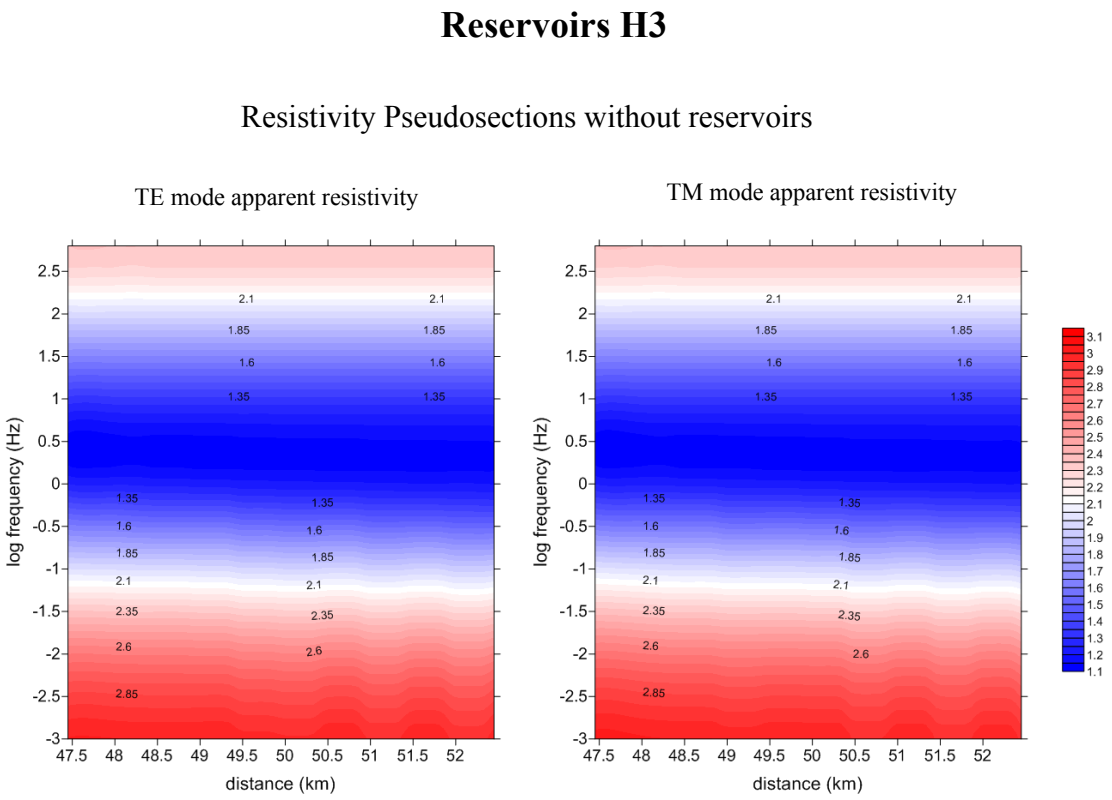

Figure 65: Resistivity TE and TM pseudosections with reservoirs case 1, resistivity value of 750Ωm. Color scale is logaritmic.

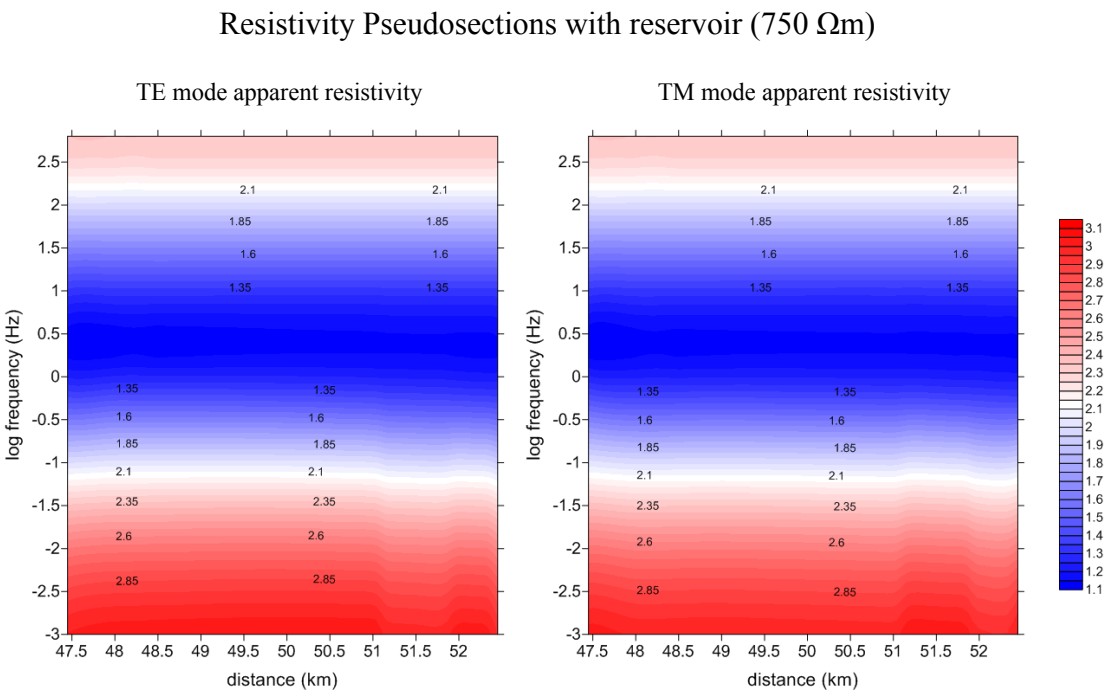

Figure 66: Resistivity TE and TM pseudosections with reservoirs case 2, resistivity value of 5000Ω. Color scale is logaritmic.

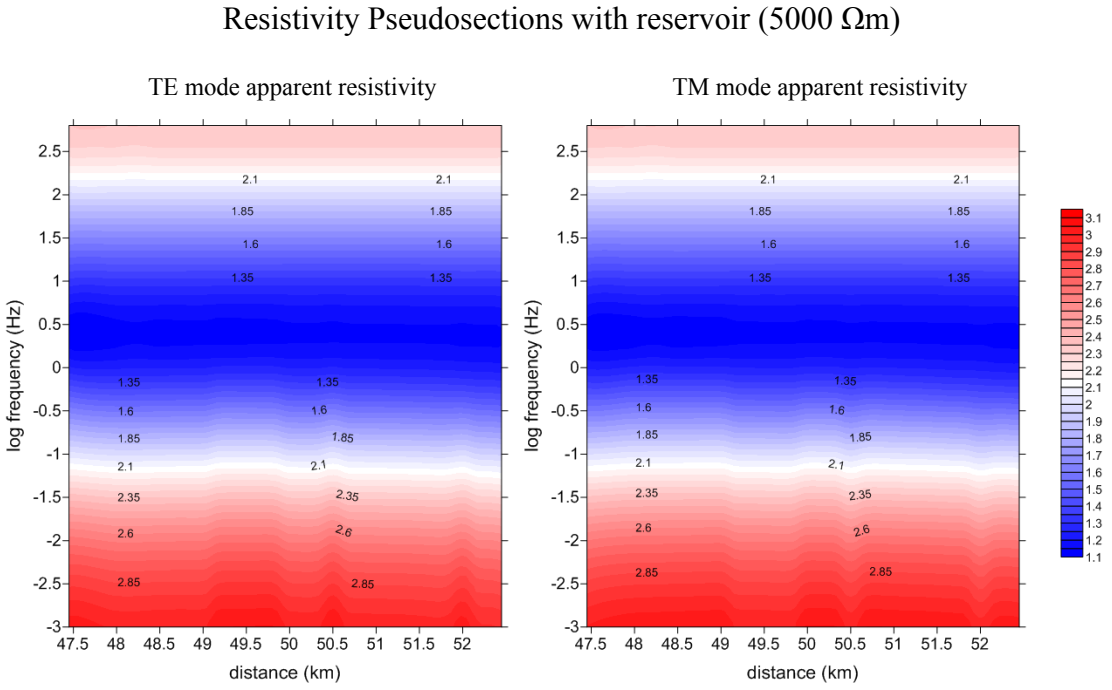

Figure 67: Misfit between pseudosections drawn in Fig. 66 and the ones in Fig. 64. Color scale is logaritmic.

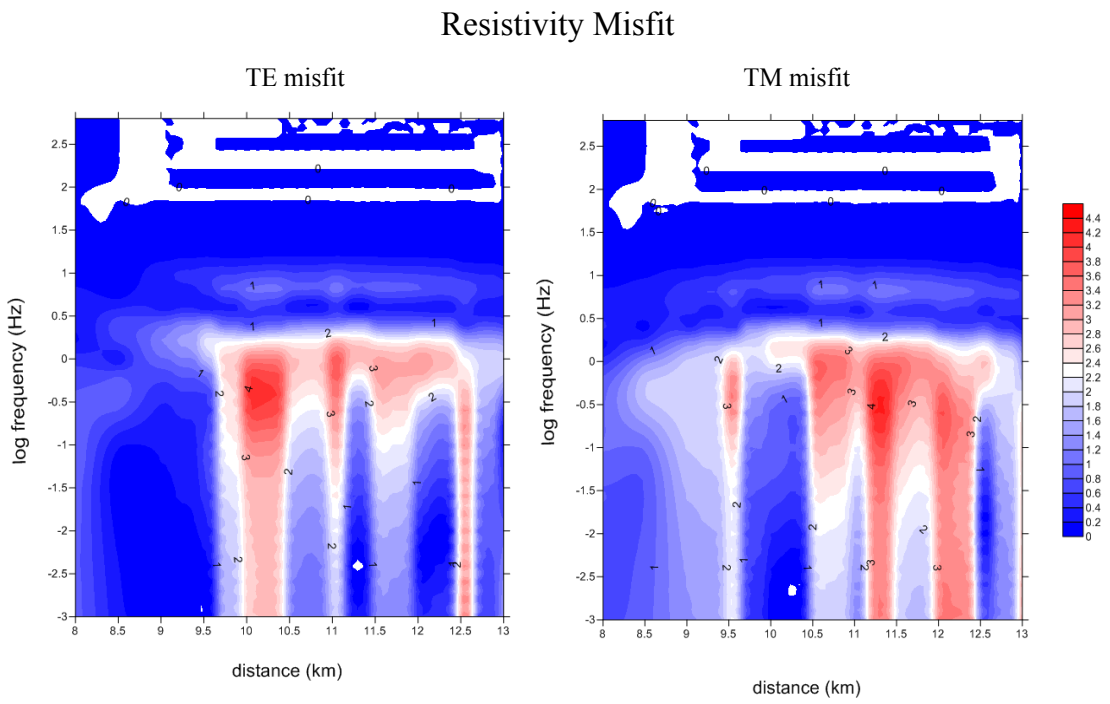

This theoretical study has been performed in order to understand the efficiency of the MT method in a geological environment with the specific features of the Potiguar Basin. As we have seen the detection of hydrocarbon reservoirs, as well as different types of buried structures depends on various factors; resistivity contrast, size of the reservoirs and their depths.

The same structure can be studied considering the dispersion of the resistivity; this is an environment in which we can expect the occurrence of the phenomenon and it could be very interesting to observe and analyze its effect on the responses.

5 CONCLUSIONS

The use of the MT method, to reconstruct images of the subsurface using electrical resistivity contrasts, is constantly in evolution and it is more and more accurate both theoretically and experimentally. Nevertheless this methodology is not widely applied and frequently its great potential is neglected.

Although the resistivity dispersion in MT is a well-known phenomenon it is often overlooked or ignored in the analysis of MT data.

For these reasons in this work we have treated both the dispersion of the resistivity in MT, and the classical MT method in the Pecém region, never applied before, and in the Potiguar Basin where generally the seismic method is used.

Starting from the MT responses in the cases of 1-D and 2-D polarizable structures we have seen, primarily, how a very simple 2-D dispersive structure has an effect on the responses curves to the point that the inversion procedure lead to a solution that differs from the case without dispersion. We next, using a 3-D modeling software, performed and showed the effects on the MT responses of a 3-D polarizable structure and how, applying it to a real case, the resistive tridimensional model has a good fit with the experimental data. The type of the 3-D structure modeled in this work can be very useful to model geothermal and hydrocarbon reservoirs, which likely account for the presence of relevant dispersion effects, due to the high degree of alteration produced by the circulation of aggressive fluids. The dispersion effects have been evaluated along three parallel profiles, normal to the longitudinal axis of the 3-D prism. Amplitude variations of the anomaly above the dispersive body have been recognized, depending on the position of the profile from the center to the edges of the prism.

The 3-D MT curves affected by the dispersion as well as the consideration of the effect in the Snake River Plain field case show that the inclusion, in the forward 3-D modeling, of the resistivity dispersion is a good contribution to a better comprehension of the structures in the subsurface. These results invite the MT users to deal with care the areas that may manifest the dispersion of the resistivity so as to minimize, as much as possible, the interpretation ambiguities.

From the application of the classical MT method we have seen that it is very effective for increasing the geological, tectonic and structural knowledge of the complex environment

of the Pecém region. We have observed its efficiency in resolving very strong resistivity contrasts between crustal blocks.

It is recommended to increase the spatial resolution of MT acquisitions in order to better discriminate the targets detected here. A geophysical acquisition with the transient electromagnetic method (TDEM) or with the controlled source audio-magnetotellurics (CSAMT) at the same location of the MT stations should be made in order to improve the resolution of the data in shallower depths, and to aid in filtering.

The second application of MT, on the structural model of the Potiguar Basin, showed through theoretical simulations that within certain limits the presence of hydrocarbon reservoir is detected by MT measurements.

From the pseudosections we have seen that shallow reservoirs are well revealed and localized, both if we consider the resistivity value one order of magnitude bigger than the surrounding and if the reservoirs are supposed to have a very high resistivity value.

The case with the deeper reservoir instead does not provide so satisfying results; the pseudosections barely show the presence of hydrocarbon, then we can assume this as a case limit for the Potiguar Basin geological structure. It could be useful, for this reason, to perform in the future an MT data acquisition in the Basin to observe the experimental MT responses in this region.

REFERENCES

Almeida, F.F.M., Hasui, Y., Brito Neves, B.B. & Fuck, R.A., 1977. Províncias estruturais brasileiras. In: SIMPÓSIO DE GEOLOGIA DO NORDESTE, 7, Campina Grande. Atas do... Campina Grande, SBG, 1977. 449p. il. p. 363 - 391.

Amaral W. and Santos T.J., 2008. Airborne geophysical and tectonics of the Ceará Central Domain, eastern region of the Santa Quitéria magmatic arc, Borborema province, NE Brazil. Revista Brasileira de Geofisica. 26(4), 527-542.

Angelim, L.A.A., Medeiros, V.C., Nesi, J.R., 2006. Programa Geologia do Brasil – PGB. Projeto Geologia e Recursos Minerais do Estado do Rio Grande do Norte. Mapa Geológico do Estado do Rio Grande do Norte. 1:500.000. Recife: CPRM/FAPERN, 2006. 1 map., 130 cm x 91cm.Scale1:500.000.Avaiable:<http://www.cprm.gov.br/publique/media/mapa_rio_grande_norte.pdf>

Araripe, P.T. & Feijó, F.J., 1994. Bacia Potiguar. Boletim de geociências da Pe- trobrás, 8(1): 127-141.

Battaglia, J., Zollo, A., Virieux, J., and Dello Jacono, D., 2008. Merging active and passive data sets in travel-time tomography: The case study of Campi Flegrei caldera (Southern Italy), Geophys. Prospect., 56, 555-573.

Berdichevsky, M. N., and Zdanov, M. S., 1984, “Advanced theory of deep geomagnetic sounding: Elsevier.

Bertani, R.T., Costa, I.G., Matos, R.M.D., 1990, Evolução tectono-sedimentar, estilo estrutural e hábitat do petróleo na Bacia Potiguar. In: RAJA GABAGLIA, G.P.; MILANI, E.J.(Coord.) Origem e evolução de bacias sedimentares. Rio de Janeiro: Petrobras. SEREC.CENSUD, p. 291-310.

Bertin, J. and J. Loeb, 1976: Experimental and Theoretical Aspects of Induced polarization, (Gebrder-Borntrger, Berlin), 2 vols.

Bjorlykke, K., 2010, Petroleum Geoscience, from sedimentary environments to rock physics, Springer, doi: 10.1007/978-3-642-02332-3

Bruno P.G:, Ricciardi G.P., Petrillo Z., Di Fiore V., Troiano A., Chiodini G., 2007. Geophysical and hydrogeological experiments from a shallow hydrothermal system at Solfatara Volcano, Campi Flegrei, Italy: Response to caldera unrest. Journal Of Geophs. Research, 122, DOI: 10.1029/2006JB004383.

Campbell, W. H., 1987, Introduction to electrical properties of the Earth’s mantle. Pure Appl. Geophys. 125: 193–204.

Chapman, S., and Ferraro, V. C. A., 1931, *Terrestrial Magnetism and Atmpospheric Electricity*,

Chang-Chin, Y., and L. Bin, 1994, The research on the 3D TDEM modeling and IP effect,

Chinese J. Geophys., **S2**, P.631.3, CJFDTotal-DQWX4S2.053.

Cole, K.S. and R.H. Cole, 1941. Dispersion and absorption in dielectrics, J. Chem. Phys., 9, 341-351.

CPRM 2003-Mapa geológico do Estado do Ceará. Escala 1:500000.

Coppola, B., R. Di Maio, I. Marino, A. Merla, D. Patella, G. Pulelli, F.M. Rossi and A. Siniscalchi, 1993, Study of the Simplon area geothermal anomaly in the frame of a transalpine deep railway tunnel feasibility project, in J.L. Reith (ed.), *Underground Transportation Infrastructures*, 93-102, Balkema, Rotterdam.

Da Cunha L. S., 2009. Tese de Doutorado. Determinação da vulnerabilidade intrínseca á poluição e transporte de contaminação: uma ferramenta para a gestão de recursos hídricos subterrâneos na área do porto do Pecém, CE.

Di Maio, R., Patella, D., e Siniscalchi, A., "Sul problema del riconoscimento di uno strato elettricamente polarizzabile mediante misure magnetotelluriche," Atti del II Convegno di Geomagnetismo ed Aeronomia, a cura di A. Meloni e B. Zolesi, ING, Roma, 239-250, 1991.

Di Maio, R., P. Mauriello, D. Patella, Z. Petrillo, S. Piscitelli, A. Siniscalchi and M. Veneruso, 1997, Self-potential, geoelectric and magnetotelluric studies in Italian active volcanic areas, *Ann. Geophys*., **40**, 519-537, doi: 10.4401/ag-3926.

Di Maio, R., D. Patella, Z. Petrillo, A. Siniscalchi, G. Cecere, and P. de Martino, "Application of electric and electromagnetic methods to the study of the Phlegrean Fields caldera," Ann. Geofis., Vol. 43, 375-390, 2000.

Dobbs, E. R. (1985). Electromagnetic waves. London: Routledge & Kegan Paul.

Esposito, R., D. Patella, "The role of the impedivity in the magnetotelluric response" PIER, 89, 225-253, 2009.

Fetter A. H., Santos T. J. S., Van Schmus W. R , Hackspacher P. C., Brito Neves B. B., Arthaud M. H., Nogueira J. A., Wernick E., 2003. Evidence for Neoproterozoic Continental Arc Magmatism in the Santa Quite´ria Batholith of Ceara´ State, NW Borborema Province, NE Brazil: Implications for the Assembly of West Gondwana. Gondwana Research, 6(2): 265–273.

Fink, J.B., E.O. McAlister, B.K. Sternberg, W.G. Wieduwilt and S.H. Ward (eds.), 1990, *Induced Polarization: Applications and Case Histories*, Investigations in Geophysics, **4**, SEG, Tulsa, Oklahoma.

Françolin, J. B. L. & Szatmari, P., 1987. Mecanismo de rifteamento da porção oriental da margem norte brasileira. Revista Brasileira de Geociências. v. 17, n. 2, p. 196-207.

Gabàs, A., and A. Marcuello, 2003, The relative influence of different types of magnetotelluric data on joint inversions, *Earth Planet. Space*, **55**, 243-248, doi: 10.1186/BF03351755.

Giammetti, S., D. Patella, A. Siniscalchi and A. Tramacere, 1996, The Siena Graben: combined interpretation of DES and MT soundings, *Ann. Geophys.*, **39**, 189-200, doi: 10.4401/ag-3961.

Grandt, C., 1991, Global thunderstorm monitoring by using the ionospheric propagation of VLF lightning pulses (sferics) with applications to climatology: Ph.D. thesis, University of Bonn.

Gurin, G. V., Tarasov, A. V., Il'in Yu. T., Titov, K. V., 2015, Application of the Debye decomposition approach to analysis of induced-polarization profiling data (Julietta gold-silver deposit, Magadan Region). *Russian Geology and Geophysics* **56**:12, 1757-1771.

He, Z., Z. Hu, W. Luo and C. Wang, 2010, Mapping reservoirs based on resistivity and induced polarization derived from continuous 3D magnetotelluric profiling: Case study from Qaidam basin, China, *Geophysics*, **75**, B25-B33, doi: 10.1190/1.3279125.

Hoheisal, A., A. Hördt and T. Hanstein, 2004, The influence of induced polarization on long-offset transient electromagnetic data, *Geophys. Prospect.*, **52**, 417-426, doi: 10.1111/j.1365-2478.2004. 00426.x.

Hoerlle, M. R., Gomes, C. J. S., & MatosATOS, R. M. D. D.. O Grabende Apodi, região sudoeste da Bacia Potiguar, RN, uma interpretação com base em seções sísmicas e dados de poços. Revista da Escola de Minas, Ouro Preto v. 60, n. 4, Oct./Dec. 2007, 2007. Available at <http://dx.doi.org/10.1590/S0370-44672007000400004>

Kaufman, A. A., and Keller, G. V., 1981 "The magnetotelluric sounding method". Elsevier.

Keller, G.V., and F.C. Frischknecht, 1966, *Electrical Methods in Geophysical Prospecting*, Pergamon. Oxford.

Jones, A. G. (2006) Electromagnetic interrogation of the anisotropic Earth: Looking into the Earth with polarized spectables. Physics of the Earth and Planetary Interiors, 158, 281-291.

Livelybrooks, D., M. Mareschal, E. Blais and J.T. Smith, 1996, Magnetotelluric delineation of the Trillabelle massive sulfide body in Sudbury, Ontario, *Geophysics*, **61**, 971-986, doi: 10.1190/1.1444046.

Lopes de Castro D, Costa Pedrosa N. Jr., Monteiro Santos F. A. 2011. Gravity–geoelectric joint inversion over the Potiguar rift basin, NE Brazil. Journal of Applied Geophysics. Vol. 7, 431-443.

Mabey, D.R., 1982, Geophysics and tectonics of the Snake River Plain, Idaho, in B. Bonnichsen and R.M. Breckenridge, *Cenozoic Geology of Idaho*, Idaho Bureau of Mines and Geology Bulletin, **26**, geology.isu.edu/B-26Ch3-1.

Madden, T.R. and T. Cantwell, 1967: Induced polarization, a review. In Mining Geophysics, Society of Exploration Geophysicists, Tulsa, Oklahoma, vol. 2, 373-400.

Mann, L.J., 1986, Hydraulic properties of rock units and chemical quality of water for INEL-1: a 10,365-foot deep test hole drilled at the Idaho National Engineering Laboratory, Idaho, *Water-Resources Investigations Report 86-4020*, 23 p., USGS, usgs/wri864020.

Manzanares-Martinez, J. and J. Gaspar-Armenta, "Direct integration of the constitutive relations for modelling dispersive metamaterials using the finite difference time-domain technique," Journal of Electromagnetic Waves and Applications, Vol. 21, 2297–2310, 2007.

Manzella, A. et al. (2004): Combined TEM-MT investigation of shallow-depth resistivity structure of Mt Somma-Vesuvius, Journal of Volcanology and Geothermal Research 131, 19-32.

Marchant, D., E. Haber and D.W. Oldenburg, 2014, Three-dimensional modeling of IP effects in time-domain electromagnetic data, *Geophysics*, **79**, E303-E314, doi: 10.1190/geo2014-0060.1.

Matos, R. M. D., 1987. Expressão sísmica de prováveis falhas de transferência na Bacia Potiguar emersa e *Graben* de Jacaúna/CE. Seminário de Geofísica, 2, Nova Friburgo. Anais... Nova Friburgo: Petrobras/Depex.

Mauriello, P., D. Patella, A. Siniscalchi, "The magnetotelluric response over 2D media with resistivity frequency dispersion," Geophysical Prospecting, Vol. 44, 789-818, 1996.

Mauriello, P., and D. Patella, 1999, Principles of probability tomography for natural-source electromagnetic induction fields, *Geophysics*, **64,** 1403-1417, doi: 10.1190/1.1444645.

Mauriello, P., D. Patella, Z. Petrillo and A. Siniscalchi, 2000, An integrated magnetotelluric study of the Mt. Etna volcanic structure, *Ann. Geophys*., **43**, 325-342, doi: 10.4401/ag-3633.

Mauriello, P., D. Patella, Z. Petrillo, A. Siniscalchi, T. Iuliano and C. Del Negro, 2004, A geophysical study of the Mount Etna volcanic area, in A. Bonaccorso, S. Calvari, M. Coltelli, C. Del Negro, and S. Falsaperla (eds.). *Mt. Etna: Volcano Laboratory*, Geophysical Monograph Series, **143**, 273-291, AGU, Washington DC.

Nabighian, M.N., and C.L. Elliot (1976): Negative induced polarization effects from layered media, Geophysics, 41, 1235-1255.

Nordsiek, S., and Weller, A., 2008, "A new approach to fitting induced-polarization spectra." GEOPHYSICS, 73(6), F235-F245. doi: 10.1190/1.2987412

Olhoeft, G., R., 1980, Electrical properties in rocks, *in* Y. S. Thoulaikian, W. R. Judd, and R.F. Roy, Eds., Physical properties od rocks and minerals, McGraw-Hill, New York, 257-330.

Palacky, G.V. (1987), Resistivity characteristics of geologic targets, in Electromagnetic Methods in Applied Geophysics, Vol. 1, Theory, 1351

Parker, E. N., 1958, Dynamics of the interplanetary gas and magnetic field. Astrophys. J. 128: 664–676.

Patella, D., 2003. On the role of the J-E constitutive relationship in applied geoelectromagnetism, Annals of Geophysics, Vol. 46, N. 3.

Patella, D., 2008. Modeling electrical dispersion phenomena in earth materials. Annals of Geophysics. Vol. 51, 159-165.

Patella, D., 1987, "Tutorial: Interpretation of magnetotelluric measurements over an electrically dispersive one-dimensional earth," Geophysical Prospecting, Vol. 35, 1-11.

Patella, D., 1993, "I principi metodologici della magnetotellurica su mezzi generalmente dispersivi," Annali di Geofisica, Vol. 36, 147-160.

Patella, D., Tramacere, A., Di Maio, R., and Siniscalchi, A., 1991, "Experimental evidence of resistivity frequency-dispersion in magnetotellurics in the Newberry (Oregon), Snake River Plain (Idaho) and Campi Flegrei (Italy) volcano-geothermal areas", *J. Volcanol. Geoth. Res.,* Vol. 48, 61-75.

Patella, D., 1979, "Resistivity frequency-dispersion affecting Magnetotelluric measurements. The study of a simple theoretical case and of its implication," Bollettino di Geofisica teorica ed applicata, Vol. 21, 67-71.

Pellerin, L., J. M. Johnston, and G. W. Hohmann, 1996, "A numerical evaluation of electromagnetic methods in geothermal exploration," Geophysics, Vol. 61, 121–137.

Pelton, W.H., W.R. Sill and B.D. Smith, 1983. Interpretation of complex resistivity and dielectric data, Part I, Geophys. Trans., 29, 297-330.

Pessoa Neto, O.C., Soares, U.M., Silva, J.G.F., Roesner, E.H., Florencio, C.P., Souza, C.A.V., 2007, Bacia Potiguar. Boletim de Geociências da Petrobras, v. 15, n. 2, p. 357-369, maio/Nov.

Price, A. T., 1962, " The theory of magnetotelluric fields when the source field is considered. J. Geophys. Res. 67, 1907-1918.

Prosvirnin, S. L. and S. Zouhdi, "On the effective constitutive parameters of metal-dielectric arrays of complex-shaped particles," Journal of Electromagnetic Waves and Applications, Vol. 20, 583–598, 2006.

Rodi W., Mackie L. R., 2001. Non linear conjugate gradients algorithm for 2-D magnetotelluric inversion. Geophysics, Vol. 66, 174-187.

Seigel, H. O., 1959, Mathematical formulation and type curves for induced polarization, *Geophysics*, **24**, 547-565, doi: 10.1190/1.1438625.

Seigel, H. O., 1974, The magnetic induced polarization (MIP) method: Geophysics, 39, 321–339.

Sjöberg, D., "Exact and asymptotic dispersion relations for homogenization of stratified media with two phases," Journal of Electromagnetic Waves and Applications, Vol. 20, 781–792, 2006.

Sochel'nikov, V. V., 1979, "Basic theory of natural electromagnetic fields in the sea". Leningrad, Gidrometeoizdat.

Srivastava, S. P., 1966, "Theory of the magnetotelluric method for a spherical conductor", Geophys. J. Roy. Astr. Soc., 11, 373-387.

Stanley, W.D., 1982, Magnetotelluric soundings on the Idaho National Engineering Laboratory facility, Idaho, *J. Geophys. Res.*, **87**, 2683-2691, doi: 10.1029/JB087iB04p02683.

Sternberg, B. K. and Oehler, D. Z., 1990, Induced-polarization hydrocarbon surveys: Arkoma Basin case histories: Induced Polarization, J. B. Fink, B. K. Sternberg, E. 0. McAlister and W. G. Wieduwilt, eds., Tulsa, OK, Soc. Explor. Geophys., p. 354-378

Stoyer, C.H., 1976, Consequences of induced polarization in magnetotelluric interpretation, *Pure Appl. Geophys.*, **114**, 435-449, doi: 10.1007/BF00876943.

Sumner, J.S., 1976, *Principles of Induced Polarization for Geophysical Exploration*, Elsevier, Amsterdam.

Sumner, J.S. (1967): The problem of negative IP anomalies, Proc. of the Symposium on Induced Electrical Polarization, Engi- neering Geoscience, Department of Mineral, Technical University of California, Berkeley, 32-50.

Simpsons F. and Bahr K., 2005, Practical Magnetotelluric, Cambridge University.

Sims W. E. et al., 1971, The estimation of magnetotelluric impedance tensor elements from measured data, Geophysics, vol. 36, no. 5, pp. 938-942. Sratton, J., 1941. Electromagnetic Theory (McGraw-Hill, New York).

Snyder, D. D, Merkel, R. H., Williams, J. T., 1977, Complex Formation Resistivity - The Forgotten Half Of The Resistivity Log

Stratton, J., (1941), Electromagnetic Theory (McGraw-Hill, New York).

Troiano, A., Di Giuseppe, M.G., Petrillo, Z., and Patella, D., 2009. Imaging 2D structures by the CSAMT method. Application to the Pantano di S. Gregorio Magno faulted basin (Southern Italy), J. Geophys. Eng., 6, 120-130, doi: 10.1088/1742-2132/6/2/003.

Ustra, A., Mendonça, C. A., Ntarlagiannis, D., Slater L. D., 2016, Relaxation time distribution obtained from a Debye decomposition of spectral induced polarization data.

Wait, J.R., 1982. Geo-electromagnetism (Academic Press, New York).

Wait, J.R., 1959, *Overvoltage Research and Geophysical Applications*, Pergamon, Oxford.

Wait, J. R., 1954, "On the relation between telluric currents and the Earth's magnetic field. Geophysics, 19, 281-289

Wannamaker, P.E., G.W. Hohmann and S.H. Ward, 1984, Magnetotelluric responses of three-dimensional bodies in layered earth, *Geophysics*, **49**, 1517-1533, doi: 10.1190/1.1441777.

Wannamaker, P.E., J.M. Johnston, J.A. Stodt and J.R. Booker, 1997, Anatomy of the southern Cordilleran hingeline, Utah and Nevada, from deep electrical resistivity profiling, *Geophysics*, **62**, 1069-1086, doi: 10.1190/1.1444208.

Stanley H. Ward (1990) 6. Resistivity and Induced Polarization Methods. Geotechnical and Environmental Geophysics: pp. 147-190.

Weidelt, P., 1972, ""The inverse problem of geomagnetic induction": Zeitschrift für Geophysik, 38, 257-290.

Weigand, M., and Kemna, A., 2016, Debye decomposition of time-lapse spectral induced polarisation data. *Computers & Geosciences* **86**, 34-45.

Wright, B. W., Kalinoski, H. T., and Smith, R. D., 1985, Investigation of retention and selectivity effects using various mobile phases in capillary supercritical fluid chromatography. *Anal. Chem.*, 57, 2823-2829

Zaslavsky, M., V. Druskin and L. Knizhnerman, 2011, Solution of 3D time-domain electromagnetic problems using optimal subspace projection, *Geophysics*, **76**, F339-F351, doi: 10.1190/geo 2011-0088.1.

Zhdanov, M.S., and G.V. Keller, 1994, *The Geoelectrical Methods in Geophysical Exploration*, Elsevier, Amsterdam.